Supplementary Information

Near-Infrared (1050 nm) Light-Driven Molecular Cobalt Photocatalysis

Byung Hak Jhun,† Jihoon Jang,† Gyeong Min Park, Seoyeon Kim, Jin Yeong Choi, Mi Sook Seo, Yubin Choi, Sohee Lee, Eun Jin Cho, Yunho Lee,* and Youngmin You**

Dr. Byung Hak Jhun, Seoyeon Kim, Yubin Choi, Sohee Lee, and Prof. Dr. Youngmin You
Department of Chemical and Biomolecular Engineering, Yonsei University, Seoul 03722, Republic of Korea
E-mail: odds2@yonsei.ac.kr

Gyeong Min Park, Jin Yeong Choi, Dr. Mi Sook Seo, and Prof. Dr. Yunho Lee
Department of Chemistry, Seoul National University, Seoul 08826, Republic of Korea
E-mail: yunhochem@snu.ac.kr

Jihoon Jang and Prof. Dr. Eun Jin Cho
Department of Chemistry, Chung-Ang University, Seoul 06974, Republic of Korea
E-mail: ejcho@cau.ac.kr

†These authors contributed equally to this work.

Supplementary Table 1. Molecular structures and photophysical parameters of long-wavelength-activatable photocatalysts

entry	structure	substrate activation mode	condition	λ_{ex} (nm)	ε (M^{-1} cm^{-1})	E^*_{ox} (V vs SCE)	E^*_{red} (V vs SCE)	Refs
1	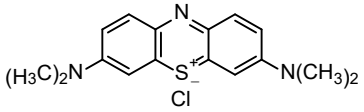	photoinduced electron transfer	CH_3CN	630 or 660	-	–0.68	1.60	1-5
2	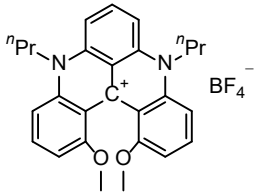	photoinduced electron transfer	DMF	640	6,150 (640 nm)	–0.61	1.15	6-8
3	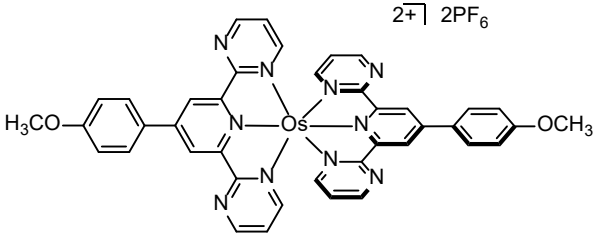	photoinduced electron transfer	CH_3CN	660	-	–0.04	1.58	9
4	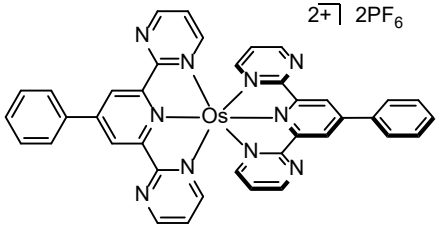	photoinduced electron transfer	CH_3CN	740	-	–0.14	1.38	9
5	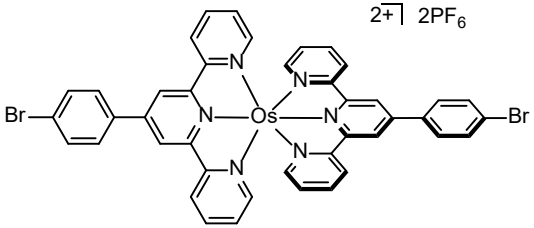	photoinduced electron transfer	CH_3CN	740	-	–0.29	1.31	9,10

6	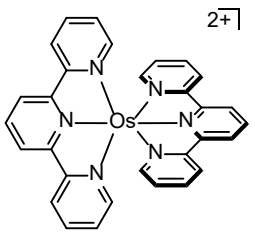	photoinduced electron transfer	CH_3CN	740	500 (740 nm)	–0.41	0.95	9
7	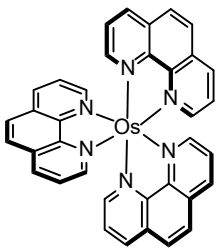	photoinduced electron transfer	CH_3CN	740	-	–0.52	0.80	9
8	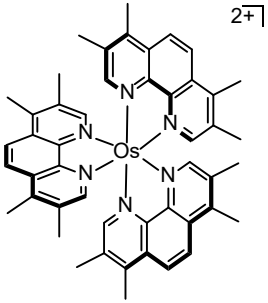	photoinduced electron transfer	CH_3OH	660	-	–1.05	0.63	11
9	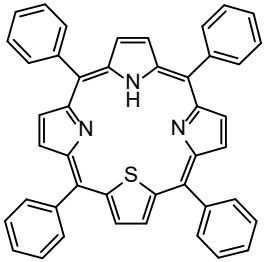	photoinduced electron transfer	DMF	645	6,700 (696 nm)	–0.74	0.75	12
10	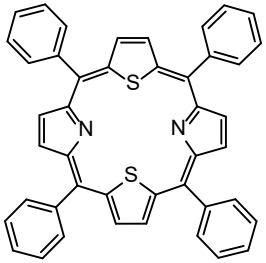	photoinduced electron transfer	DMF	645	6,400 (677 nm)			12

11	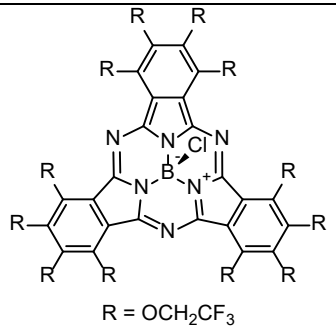 R = OCH_2CF_3	photoinduced electron transfer	CH_3CN/CH_3OH	650	3700 (650 nm)	–0.81	1.28	13
12	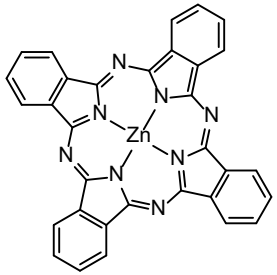	photoinduced electron transfer	CH_3CN/DMF	635	-	–0.78	0.38	14
13	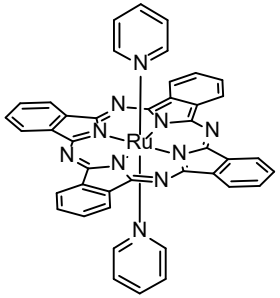	photoinduced electron transfer	acetone DMF	634	55,000 (634 nm)	–0.78	0.77	15
14	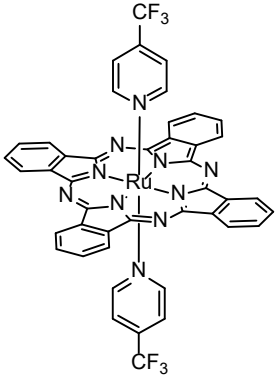	photoinduced electron transfer	acetone DMF	634	-	–0.77	0.66	15

15	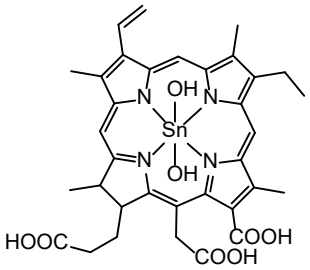	photoinduced electron transfer	DBPS	660	-	-	-	16
16	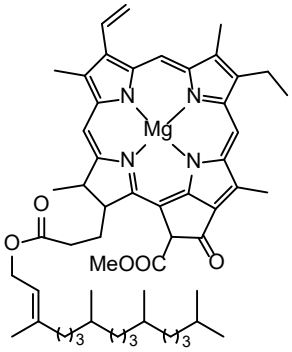	energy transfer	DMSO	620	-	-	-	17
17	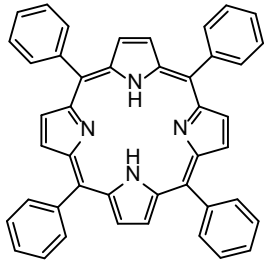	photoinduced electron transfer	DMSO	660	-	-	-	18
18	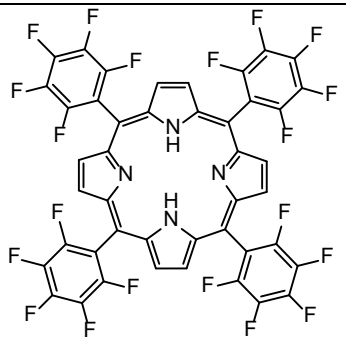	photoinduced electron transfer	DMSO	660	-	-	-	18

19	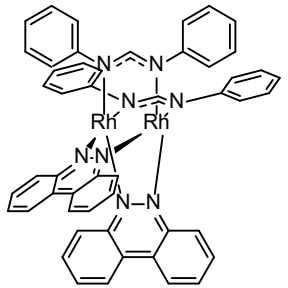	photoinduced electron transfer	H_2O/DMF	670	1,300 (735 nm)	-	2.05	19,20
20	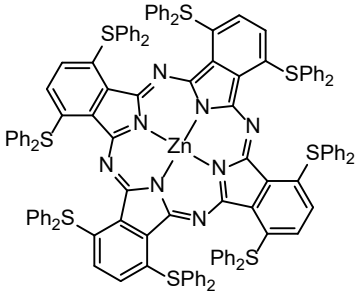	energy transfer	CH_3OH/pyridine	810	-	-	0.35	21
21	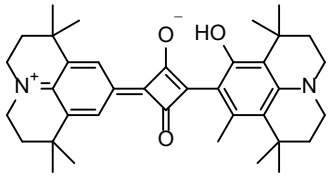	photoinduced electron transfer	DMSO	810	-	–1.45	0.84	22
22	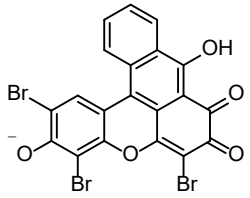	photoinduced electron transfer	DMSO	631 or 830	-	-	-	23
23	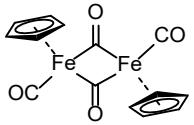	hydrogen atom transfer	CH_3CN	730	13 (730 nm)	-	-	24

24	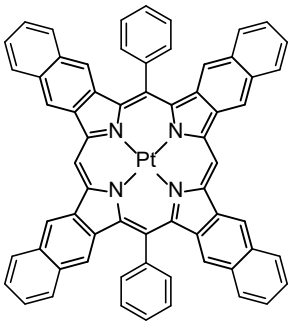	triplet-triplet annihilation-based up conversion	CH_3CN DMF DMSO	730	2,100 (730 nm)	-	-	25
25	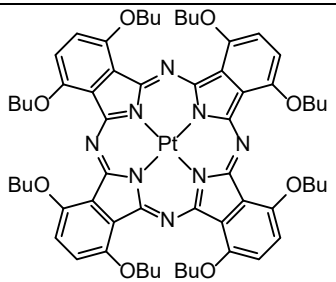	triplet-triplet annihilation-based up conversion	CH_3CN DMF DMSO	730	-	-	-	25
26	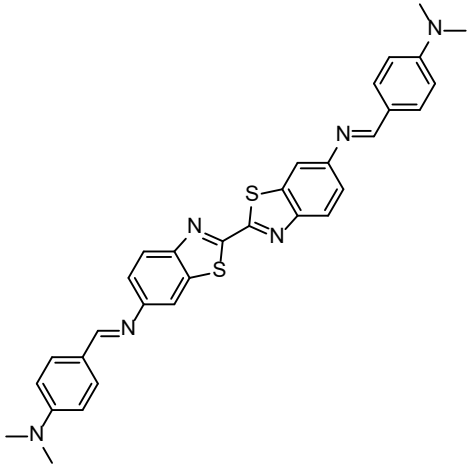	two-photon absorption	CH_3CN	850	-	-	-	26

27	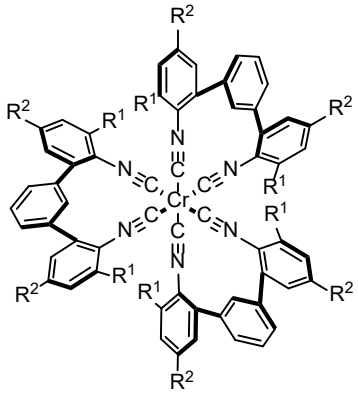	photoinduced electron transfer	benzene	623	5,200 (623 nm)	–2.13 (mesityl) –2.03 (pyrenyl)	-	27
28	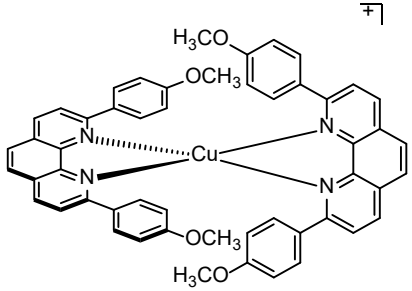	photoinduced electron transfer	CD_3CN	623	534	-	-	28
29	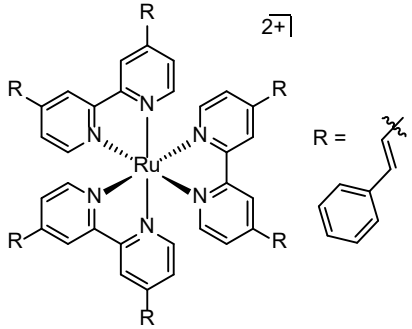	energy transfer	CH_3CN CH_3OH CD_3CN	740	-	-	-	29
30	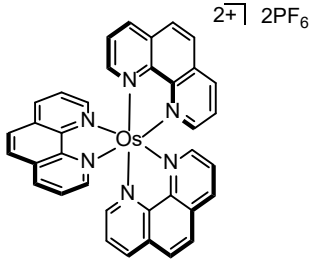	consecutive photoinduced electron transfer	DMSO	660	-	-	-	30

31	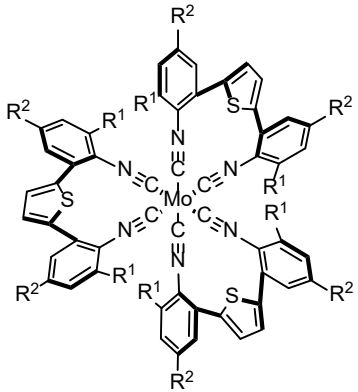 R^1 = ^{t}Bu R^2 = 1,3-dimethoxyphenyl	energy transfer	toluene CD_3CN	635	3,340 (635 nm)	-	-	31
32	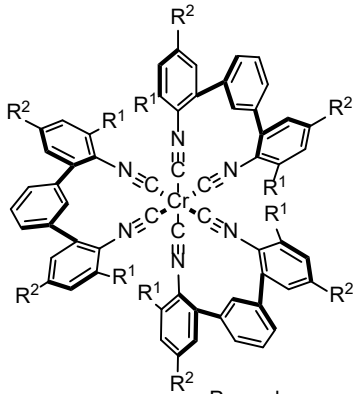 R^1 = ^{t}Bu R^2 = Pyrenyl	triplet-triplet annihilation-based up conversion	-	705	-	-	-	32
33		consecutive photoinduced electron transfer	PBS/DMSO	620	-	–0.68	1.60	33

34	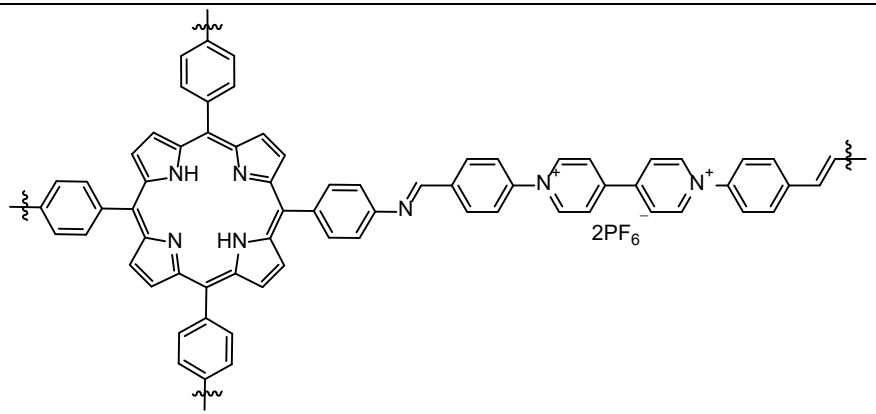	photoinduced electron transfer	CH_3CN	725	-	-	-	34
35	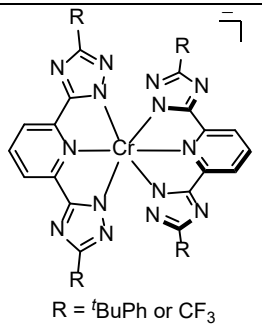 R = ^{t}BuPh or CF_3	photoinduced electron transfer	CH_3CN CD_3CN	632	-	-	0.29 (^{t}BuPh) 0.59 (CF_3)	35
36	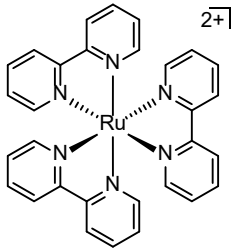	energy transfer	DMSO	660	-	–0.81	0.77	36

37	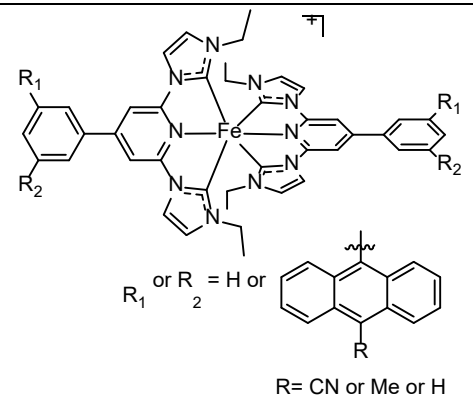	energy transfer	CD_2Cl_2	623	-	-	-	37
38	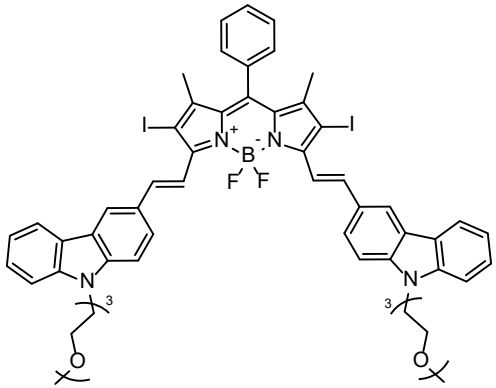	energy transfer	CH_2Cl_2	720	-	-	-	38
39	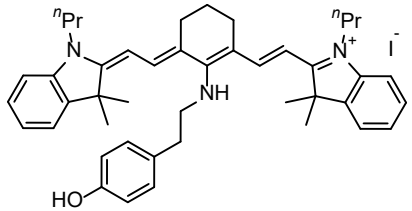	photoinduced electron transfer	DMSO	810	-	–1.19	0.72	39
40	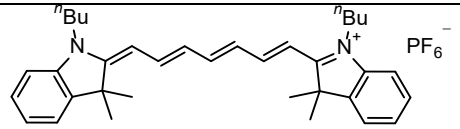	photoinduced electron transfer	DMSO	810	-	–0.88	0.80	39
41	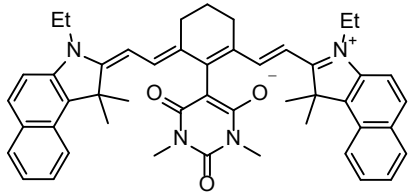	photoinduced electron transfer	DMSO	810	-	–1.00	0.48	39

42	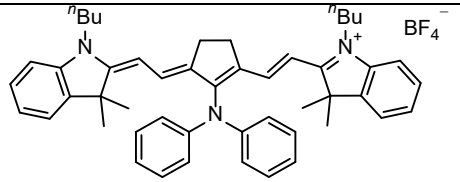	photoinduced electron transfer	DMSO	810	-	–0.80	0.74	39
43	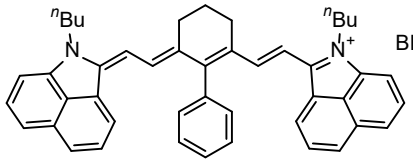	photoinduced electron transfer	DMSO	810	-	–0.38	0.79	39

Supplementary Table 2. Simulated electronic transitions of [**Co**]$^{2+}$

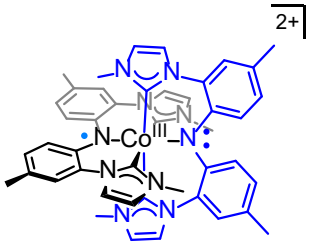

state	energy (eV)	oscillator strength	transition character
D_1	0.34	0.0663	LMCT + π–π* (amido)
D_2	1.52	0.0347	MLCT + LLCT (carbene → amido)
D_5	1.67	0.0068	MC + n–π* (amido)
D_6	1.78	0.0041	n–π*
D_8	2.11	0.0882	MLCT + LLCT (carbene → amido)

Supplementary Table 3. Isosurfaces for the hole and electron distributions of the electronic transitions in Supplementary Table 2

state	hole	electron
D_1	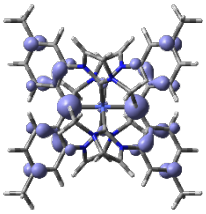	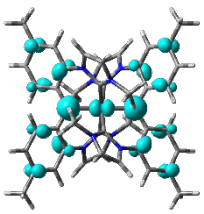
D_2	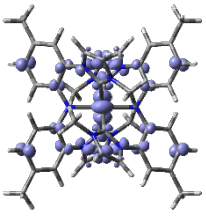	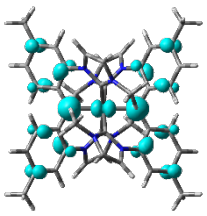
D_5	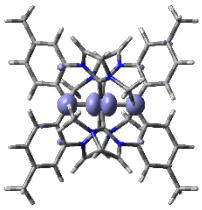	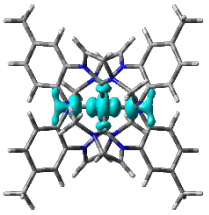
D_6	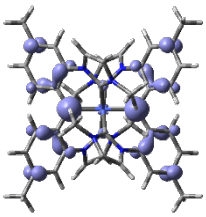	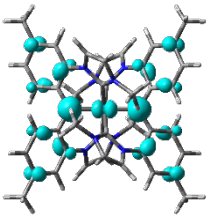
D_8	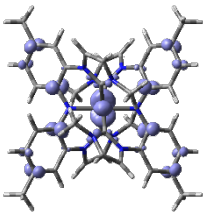	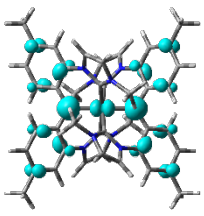

Supplementary Table 4. Population analyses for the electronic transitions of [**Co**]$^{2+}$

state	fragment	hole (%)	electron (%)	difference (electron% – hole%)
D_1	Co	0.36	12.58	12.22
	carbene	87.98	80.41	–7.58
	amido	8.61	4.31	–4.31
D_2	Co	24.37	12.58	–11.79
	carbene	33.51	4.31	–29.20
	amido	41.02	80.41	39.38
D_5	Co	55.34	54.86	–0.48
	carbene	4.61	12.29	7.68
	amido	38.70	31.84	–6.86
D_6	Co	21.33	12.58	–8.75
	carbene	40.26	4.31	–35.96
	amido	37.65	80.41	42.76
D_8	Co	30.97	12.58	–18.39
	carbene	12.71	4.31	–8.41
	amido	52.12	80.41	28.28

Supplementary Table 5. Simulated electronic transitions of $[\mathbf{Co}]^{3+}$

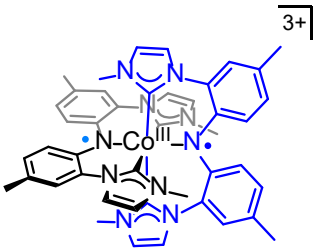

state	energy (eV)	oscillator strength	transition character
$\mathbf{S_1}$	1.56	0.0002	LLCT (carbene → amido) + π–π* (amido)
$\mathbf{S_2}$	1.61	0.1425	LLCT (carbene → amido) + π–π* (amido)
$\mathbf{S_3}$	1.71	0.0119	MC + n–π* (amido)
$\mathbf{S_4}$	1.81	0.0257	LLCT (carbene → amido)
$\mathbf{S_5}$	1.86	0.0038	LLCT (carbene → amido)
$\mathbf{S_7}$	1.91	0.0001	LLCT (carbene → amido) + π–π* (amido)
$\mathbf{S_{12}}$	2.12	0.0733	LLCT (carbene → amido)

Supplementary Table 6. Isosurfaces for the hole and electron distributions of the electronic transitions in Supplementary Table 5

state	hole	electron
S_1	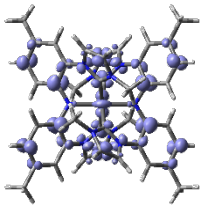	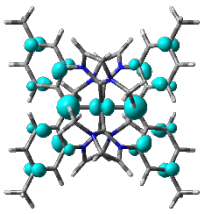
S_2	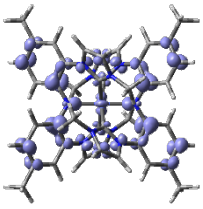	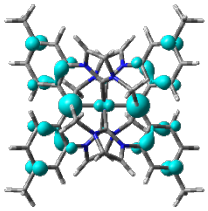
S_3	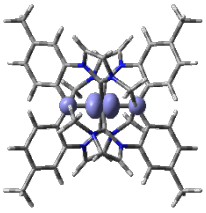	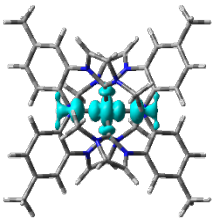
S_4	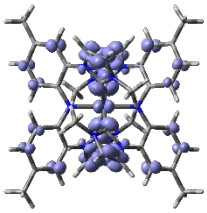	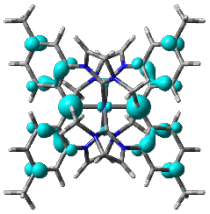
S_5	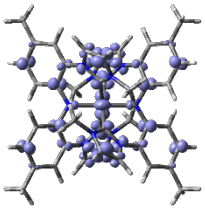	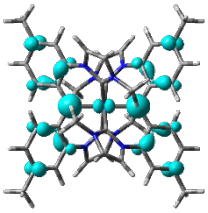
S_7	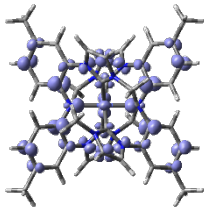	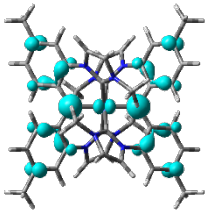
S_{12}	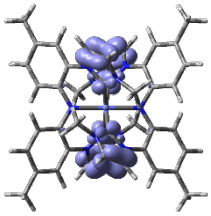	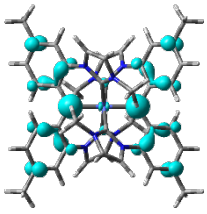

Supplementary Table 7. Population analyses for the electronic transitions of [**Co**]$^{3+}$

state	fragment	hole (%)	electron (%)	difference (electron% – hole%)
	Co	7.86	1.63	–6.22
$\mathbf{S_1}$	carbene	35.13	7.98	–27.15
	amido	55.00	87.32	32.32
	Co	3.66	3.74	0.08
$\mathbf{S_2}$	carbene	27.47	7.43	–20.04
	amido	66.31	85.81	19.5
	Co	65.50	56.10	–9.40
$\mathbf{S_3}$	carbene	7.71	11.51	3.81
	amido	25.81	31.46	5.65
	Co	4.53	1.15	–3.38
$\mathbf{S_4}$	carbene	54.61	8.24	–46.37
	amido	39.91	87.54	47.64
	Co	10.15	5.45	–4.70
$\mathbf{S_5}$	carbene	42.35	5.96	–36.39
	amido	45.87	85.58	39.71
	Co	5.12	6.19	1.07
$\mathbf{S_7}$	carbene	31.61	5.56	–26.05
	amido	60.85	85.24	24.39
	Co	0.94	0.68	–0.26
$\mathbf{S_{12}}$	carbene	80.88	8.49	–72.39
	amido	16.07	87.76	71.69

Supplementary Table 8. Simulated electronic transitions of [**Co–H**]$^{2+}$

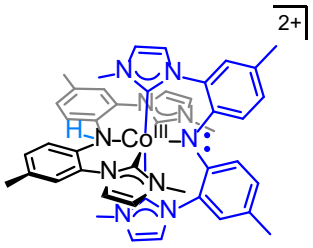

state	energy (eV)	oscillator strength	transition character
S_1	1.09	0.0001	MLCT + LLCT (amido → amine)
S_2	1.76	0.0109	MLCT + LLCT (amido → amine)
S_3	2.54	0.0002	MLCT
S_4	2.92	0.0128	LMCT

Supplementary Table 9. Isosurfaces for the hole and electron distributions of the electronic transitions in Supplementary Table 8

state	hole	electron
S_1	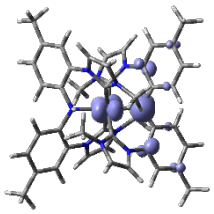	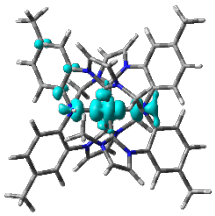
S_2	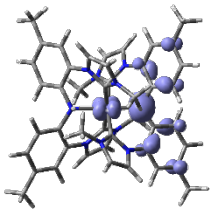	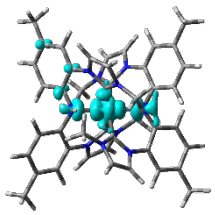
S_3	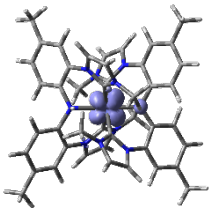	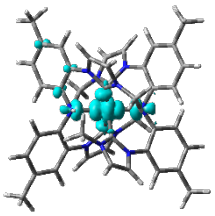
S_4	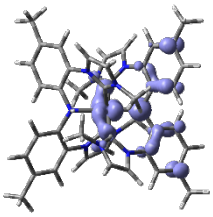	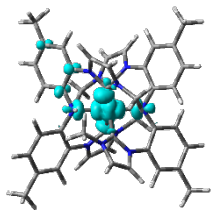

Supplementary Table 10. Population analyses for the electronic transitions of [**Co–H**]$^{2+}$

state	fragment	hole (%)	electron (%)	difference (electron% – hole%)
S_1	Co	51.52	56.29	4.77
	carbene	3.43	10.24	6.81
	amido	43.93	32.43	–11.50
S_2	Co	26.22	56.29	30.07
	carbene	4.22	10.24	6.02
	amido	67.85	32.43	–35.42
S_3	Co	79.47	55.21	–24.26
	carbene	9.22	12.72	3.50
	amido	10.72	30.92	20.20
S_4	Co	29.00	51.92	22.92
	carbene	15.29	16.45	1.16
	amido	53.08	30.23	–22.84

Supplementary Table 11. Simulated electronic transitions of [**Co–H**]$^{3+}$

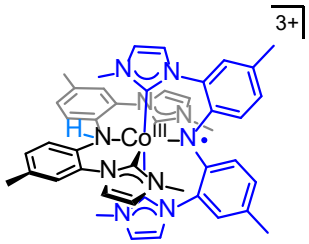

state	energy (eV)	oscillator strength	transition character
D_1	1.47	0.0016	MC + n–π* (amido)
D_2	1.60	0.0734	LLCT (carbene → amido) + π–π* (amido)
D_5	1.82	0.0125	LLCT (carbene → amido) + π–π* (amido)
D_6	1.86	0.0101	LLCT (carbene → amido)
D_9	2.18	0.0579	LLCT (carbene → amido) + π–π* (amido)
D_{12}	2.32	0.0250	MC + n–π* (amido)

Supplementary Table 12. Isosurfaces for the hole and electron distributions of the electronic transitions in Supplementary Table 11

state	hole	electron
$\mathbf{D_1}$	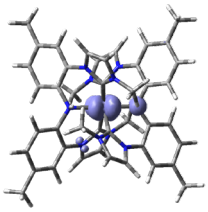	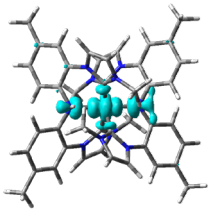
$\mathbf{D_2}$	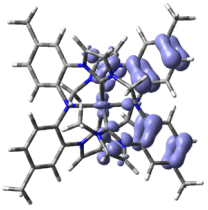	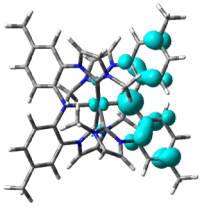
$\mathbf{D_5}$	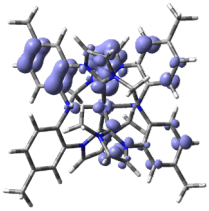	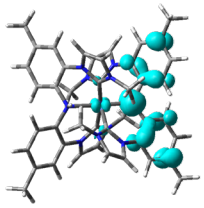
$\mathbf{D_6}$	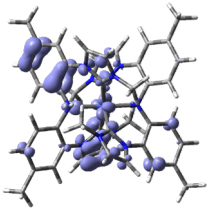	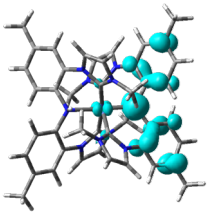
$\mathbf{D_9}$	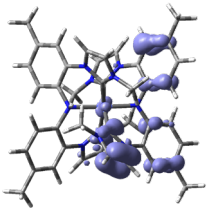	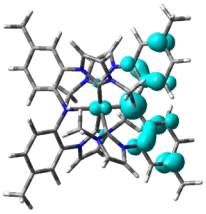
$\mathbf{D_{12}}$	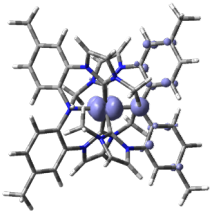	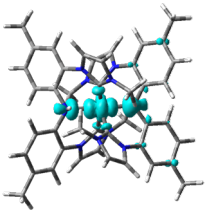

Supplementary Table 13. Population analyses for the electronic transitions of [**Co–H**]$^{3+}$

state	fragment	hole (%)	electron (%)	difference (electron% – hole%)
	Co	74.62	59.56	–15.06
D_1	carbene	6.86	10.07	3.20
	amido	17.76	29.45	11.69
	Co	6.08	4.01	–2.07
D_2	carbene	31.27	6.63	–24.64
	amido	60.33	86.30	25.97
	Co	3.91	4.01	0.10
D_5	carbene	42.99	6.63	–36.36
	amido	51.40	86.30	34.90
	Co	8.01	4.01	–4.00
D_6	carbene	40.69	6.63	–34.06
	amido	49.25	86.30	37.05
	Co	3.87	5.79	1.92
D_9	carbene	44.55	6.73	–37.82
	amido	48.38	84.49	36.11
	Co	56.64	53.53	–3.12
D_{12}	carbene	10.55	9.82	–0.73
	amido	31.53	35.51	3.97

Supplementary Table 14. Selected bond distances and angles for $[\mathbf{Co}]^{3+}$

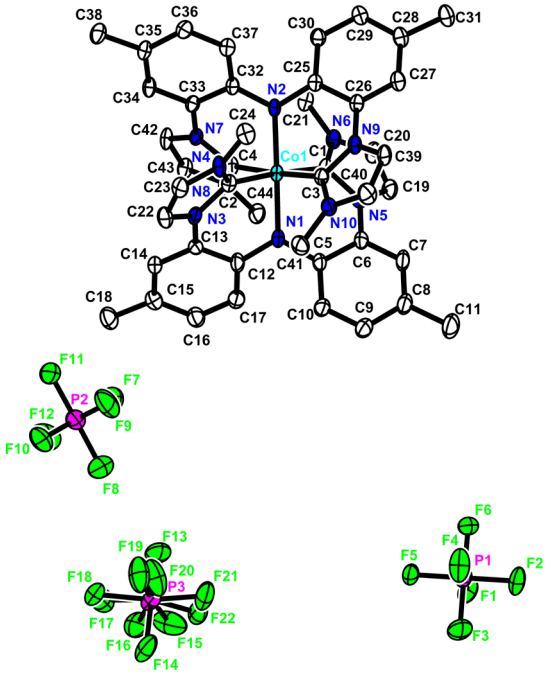

bond distances (Å)		bond angles (°)	
Co(1)–N(1)	1.919(6)	N(1)–Co(1)–N(2)	179.1(4)
Co(1)–N(2)	1.925(3)	N(1)–Co(1)–C(1)	88.2(9)
Co(1)–C(1)	1.939(6)	N(1)–Co(1)–C(2)	87.6(2)
Co(1)–C(2)	1.936(4)	N(1)–Co(1)–C(3)	92.1(3)
Co(1)–C(3)	1.931(4)	N(1)–Co(1)–C(4)	91.0(03)
Co(1)–C(4)	1.940(9)	N(2)–Co(1)–C(1)	92.3(8)
		N(2)–Co(1)–C(2)	91.6(9)
		N(2)–Co(1)–C(3)	88.3(7)
		N(2)–Co(1)–C(4)	88.4(9)
		C(1)–Co(1)–C(2)	175.8(8)
		C(3)–Co(1)–C(4)	176.8(4)
		C(12)–N(1)–C(5)	119.1(6)
		C(5)–N(1)–Co(1)	120.3(4)
		C(12)–N(1)–Co(1)	120.4(7)
		C(32)–N(2)–C(25)	120.6(4)
		C(32)–N(2)–Co(1)	119.6(4)
		C(25)–N(2)–Co(1)	119.7(1)

Supplementary Table 15. The structural parameters for [**Co**]$^{3+}$ obtained from SC-XRD data and DFT calculations

		bond distances (Å)	bond angles (°)
Co–N	experimental	1.925(3), 1.919(6)	
	DFT	1.988, 1.988	
Co–C	experimental	1.936(4)	
		1.931(4)	
		1.939(6)	
		1.940(9)	
	DFT	1.998, 1.998	
		1.998, 1.998	
N–Co–N	experimental		179.1(4)
	DFT		180.0
C–Co–C	experimental		175.8(8), 176.8(4)
	DFT		173.0, 173.0

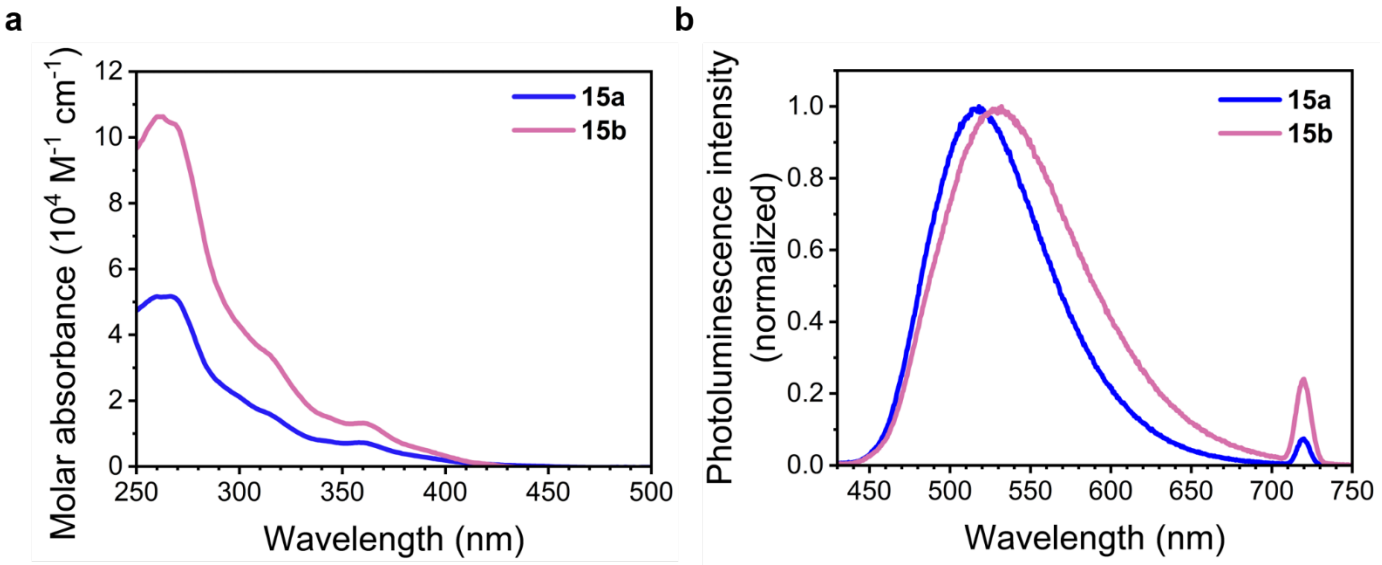

Supplementary Fig. 1 | Photophysical properties. a, UV–Vis absorption spectra of **15a** and **15b** (10 μM in CH_3CN). **b**, Photoluminescence spectra (λ_{ex} = 360 nm) of **15a** and **15b** (10 μM in deaerated CH_3CN).

a

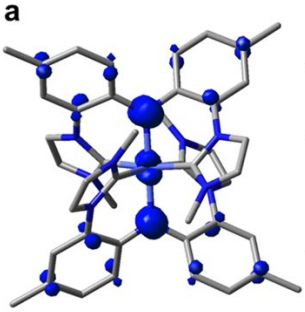

Atom	Spin density
Co	0.167(7)
N1	0.227(7)
N2	0.227(7)

b

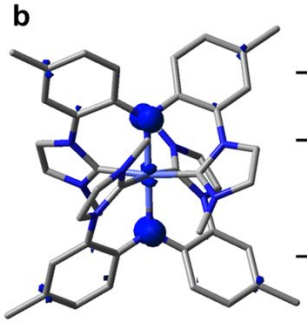

Atom	Spin density
Co	0.026(2)
N1	0.464(3)
N2	0.464(3)

Supplementary Fig. 2 | Radical delocalization. a,b, Mulliken spin density contour (isovalue = 0.006) for $[\mathbf{Co}]^{2+}$ (**a**) and $[\mathbf{Co}]^{3+}$ (**b**) obtained at the UB3LYP/def2-TZVPP level of theory.

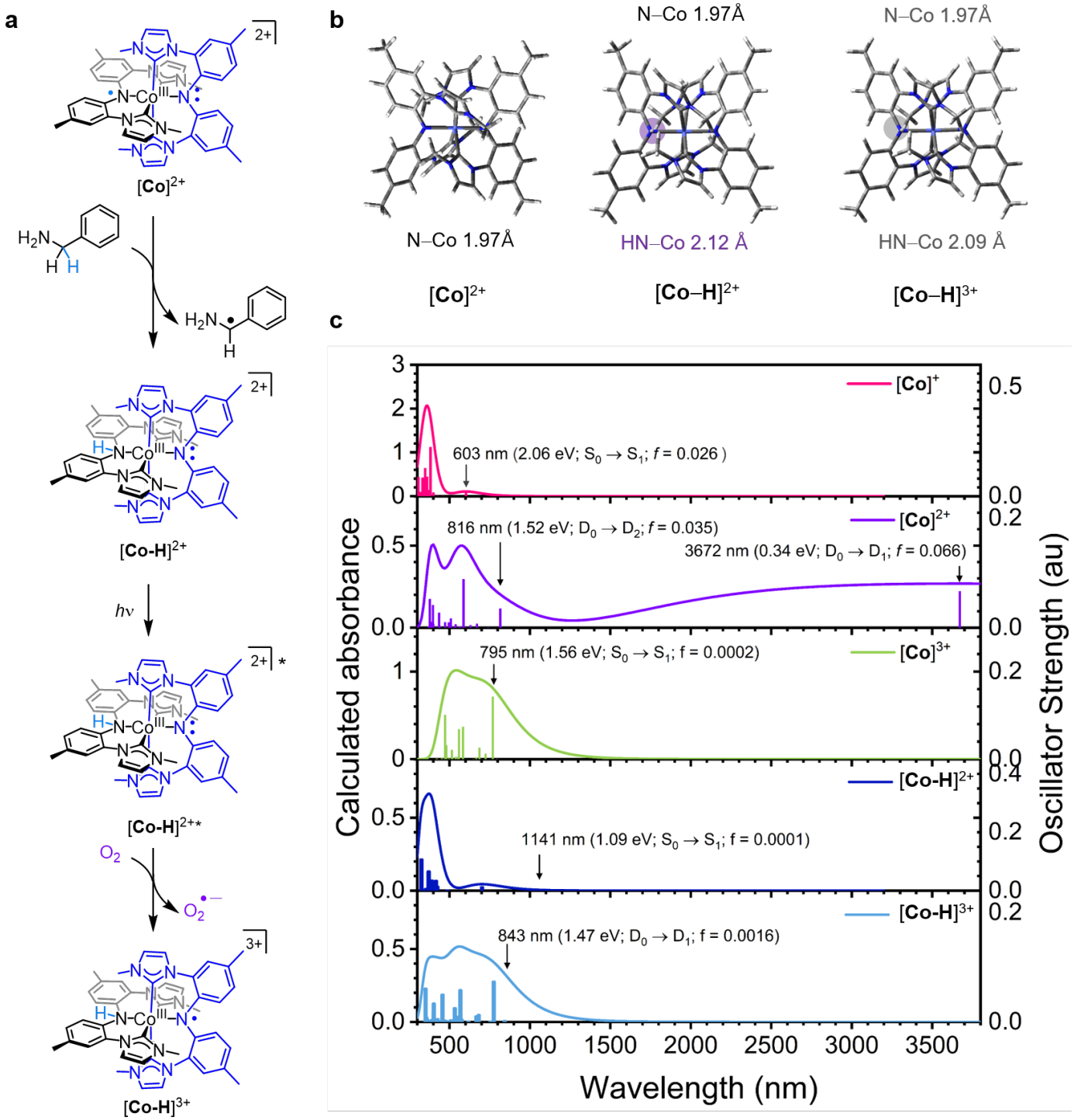

Supplementary Fig. 3 | Simulated electronic transitions. a, Plausible reaction for the formation of intermediate Co species. **b,** Optimized geometries of $[\mathbf{Co}]^{2+}$, $[\mathbf{Co–H}]^{2+}$ and $[\mathbf{Co–H}]^{3+}$ calculated at UB3LYP/def2-SVP level of theory with the conductive polarizable continuum model parameterized for CH_3CN. **c,** Simulated UV–Vis–NIR absorption spectra. Refer to Supplementary Tables 2–4 and 8–13 for the full calculation results.

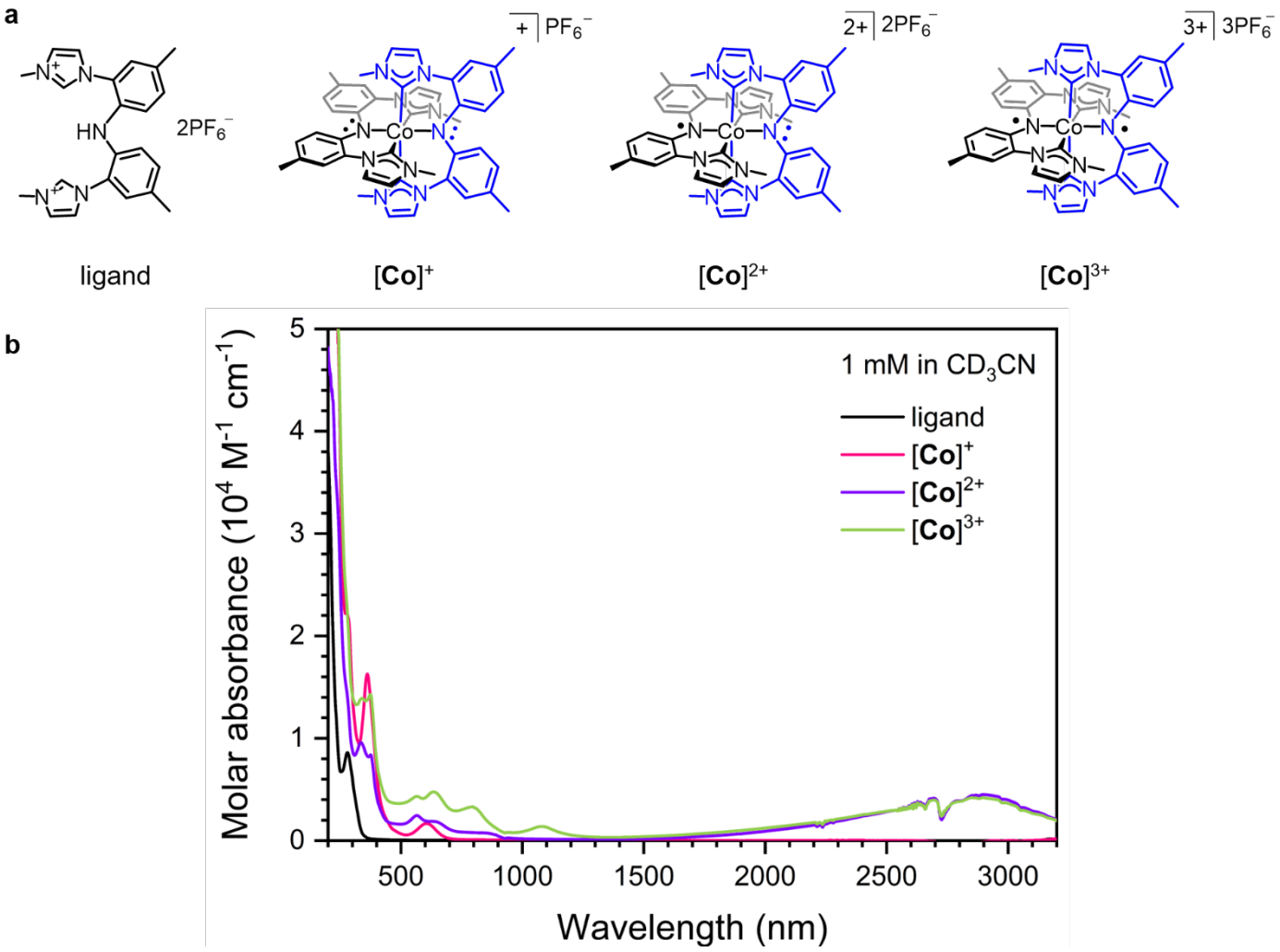

Supplementary Fig. 4 | Vis–NIR absorption spectra. a, Chemical structures of the ligand and three oxidation-state variants of the Co complexes. **b,** Experimental UV–Vis–NIR absorption spectra of CD_3CN solutions of 1.0 mM Co complexes.

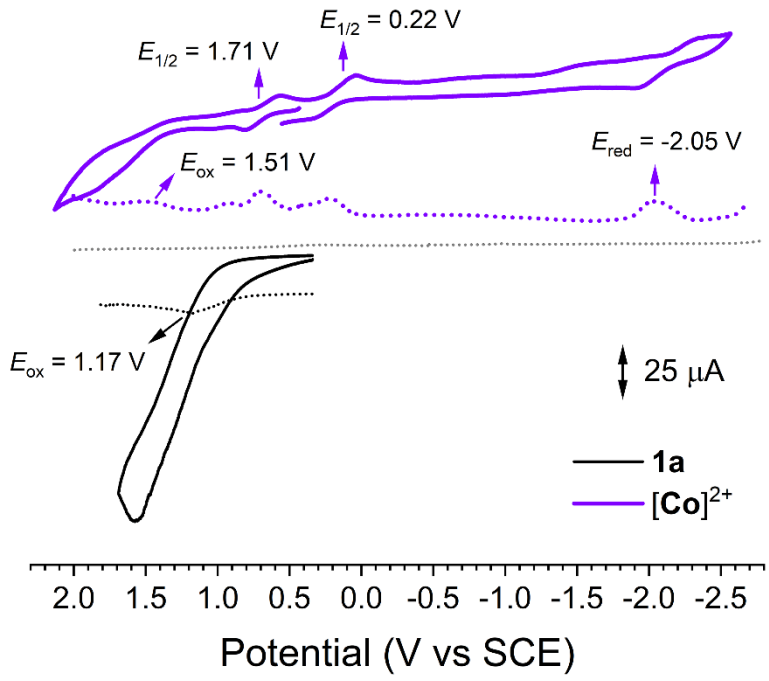

Supplementary Fig. 5 | Electrochemical potentials. Cyclic (CV, solid lines) and differential pulse voltammograms (DPV, dotted lines) for Ar-saturated THF solutions containing 0.10 M (*n*-Bu)$_4$NPF$_6$ and 2.0 mM [**Co**]$^{2+}$ (blue) or 12 mM **1a** (black) and. A glassy carbon disc and a Pt wire for the working and counter electrodes, respectively; an Ag/AgNO$_3$ pseudo reference electrode; scan rate = 0.1 V s^{-1} (CV) and 4 mV s^{-1} (DPV). The grey dotted line is the DPV of the blank solution (i.e., an Ar-saturated THF solution containing 0.10 M (*n*-Bu)$_4$NPF$_6$ only). The ferrocenium/ferrocene redox couple (Fc$^+$/Fc) was used as the external standard.

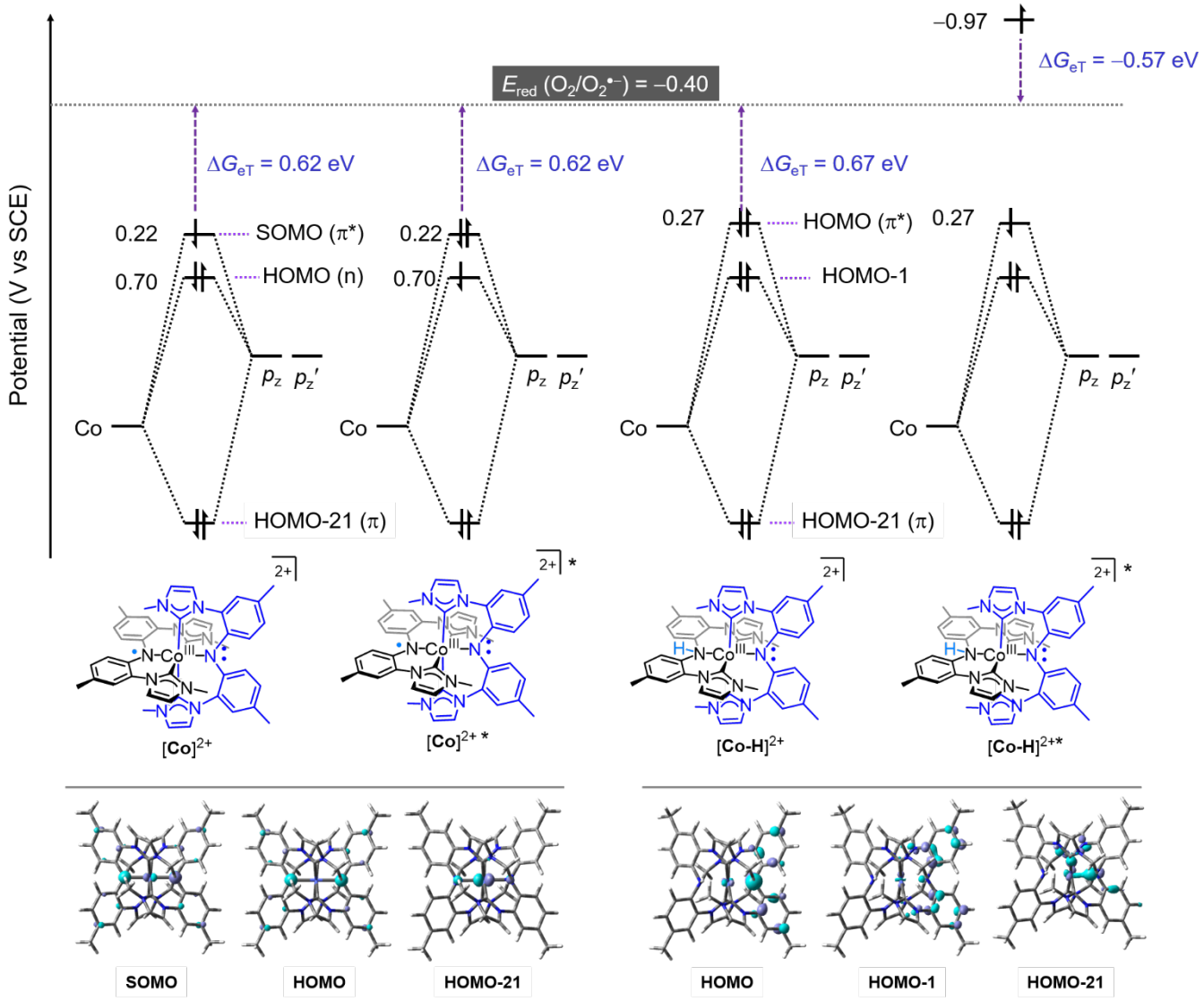

Supplementary Fig. 6 | Thermicity for electron transfer. Molecular orbitals and driving forces for electron transfer from the ground- and excited-state [**Co**]$^{2+}$ and [**Co**–**H**]$^{2+}$ to molecular dioxygen, leading to the formation of a superoxide anion. The electrochemical potentials of [**Co**–**H**]$^{2+}$ were estimated through quantum chemical calculations at the UB3LYP/def2-SVP level of theory in combination with a thermodynamic Born–Haber cycle. The estimated [**Co**–**H**]$^{2+}$ potential value was corrected by referencing the difference between the theoretical and experimental oxidation potentials of [**Co**]$^{2+}$. Shown at the bottom are isosurface plots of molecular orbitals involved in the electron transfer (isovalue = 0.07).

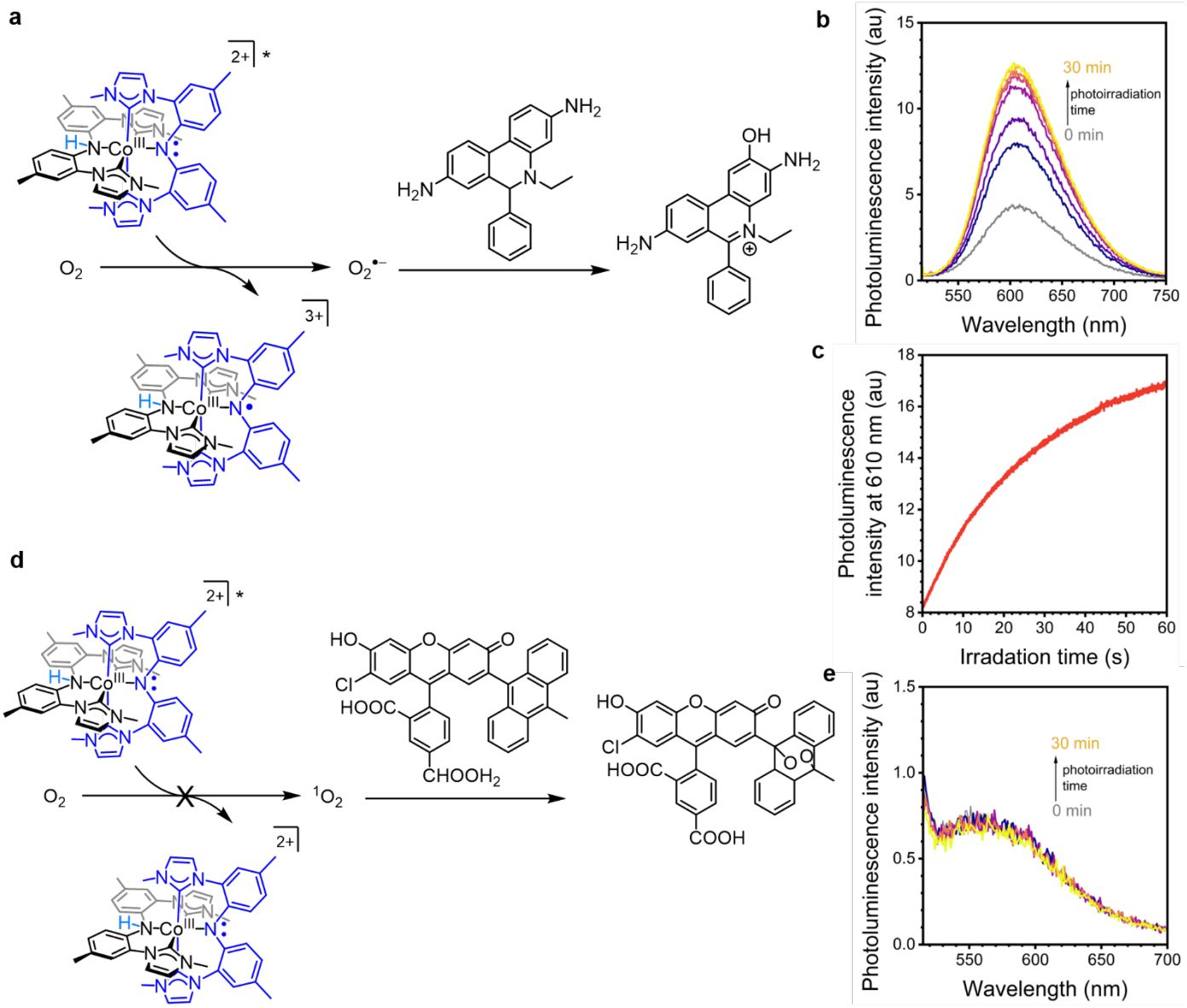

Supplementary Fig. 7 | Photosensitization of superoxide anion. a, Fluorescence detection of the superoxide anion. **b**, Evolution of photoluminescence spectra of a CH_3CN solution containing a 10 μM fluorescent superoxide sensor and a 100 μM $[\mathbf{Co–H}]^{2+}$ upon continuous photoirradiation at a wavelength of 510 nm. **c**, Corresponding photoluminescence intensity increase. **d**, Fluorescence detection of the singlet oxygen. **e**, Evolution of photoluminescence spectra of a CH_3CN containing a 10 μM fluorescent singlet oxygen sensor and a 100 μM $[\mathbf{Co–H}]^{2+}$ upon continuous photoirradiation at a wavelength of 510 nm.

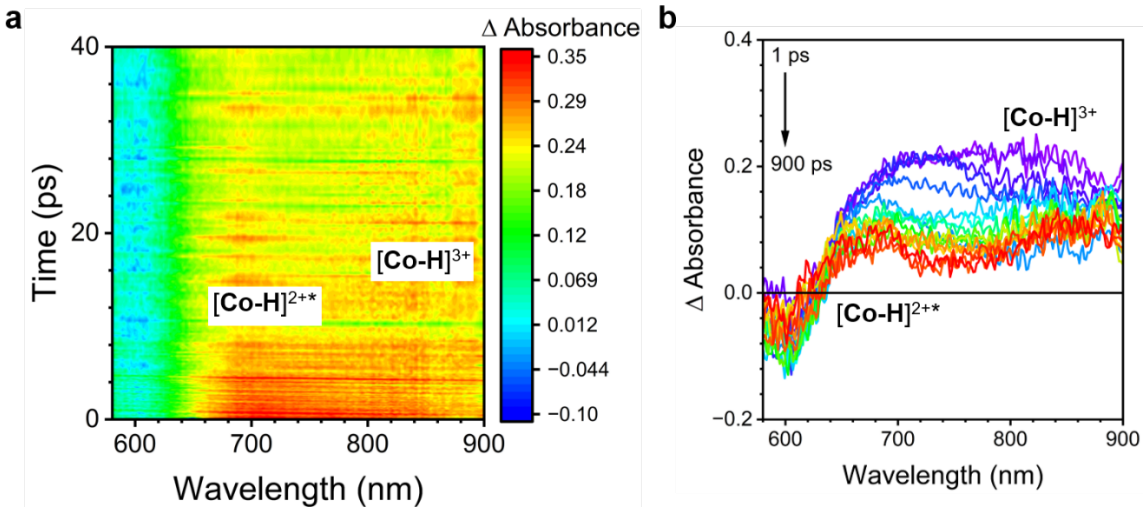

Supplementary Fig. 8 | Superoxide anion scavenging. a, Heatmap of the transient absorption signals of an CH_3CN solution containing 2.0 mM $[\mathbf{Co}]^{2+}$, 200 mM **1a**, and 1.0 M TEMPOL, a superoxide anion scavenger, recorded after femtosecond pulsed laser photoexcitation at 550 nm. **b,** Selected transient absorption spectra.

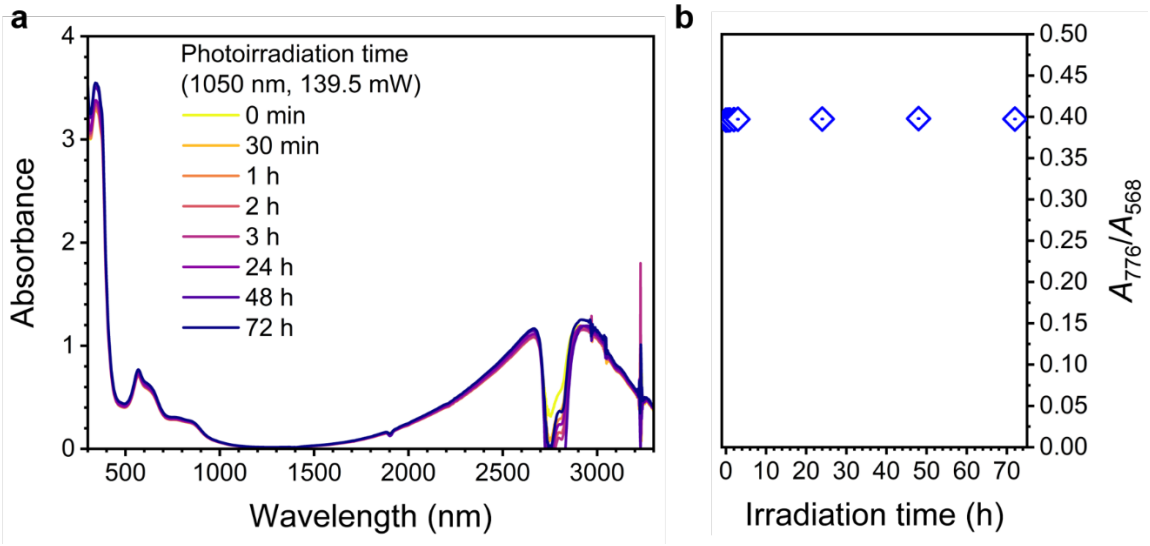

Supplementary Fig. 9 | Photostability of $[Co]^{2+}$. **a**, Vis–NIR absorption spectral changes of a 1.0 mM $[\mathbf{Co}]^{2+}$ in CD_3CN upon continuous photoirradiation at 1050 nm (139.5 mW). **b**, The absorbance ratio at 776 nm over 568 nm was plotted as a function of photoirradiation time to evaluate photostability.

Supplementary Characterization.

Analytical data for the synthesized compounds

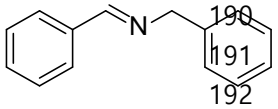

Synthesis of 1b. An oven-dried reaction vial equipped with a magnetic stir bar was charged with **1a** (11 mg, 0.10 mmol), $[\mathbf{Co}]^{2+}$ (8.0 mg, 10 mol%), and anhydrous CH_3CN (1.0 mL). The vial was sealed with a screw cap fitted with a PTFE/silicone septum, through which molecular oxygen was introduced by bubbling via a needle connected to an oxygen balloon for 10 min. The reaction mixture was then stirred under irradiation with a 1050-nm lamp in a light-shielded UV viewing cabinet. Upon completion of the reaction, as monitored by TLC and GC–MS, the solvent was removed under reduced pressure. The resulting residue was purified by flash column chromatography on silica gel using a mixture of hexanes and ethyl acetate containing 1 vol% triethylamine as the eluent. **1b** as a colorless oil in a 75% yield (15 mg). ^{1}H NMR (600 MHz, $CDCl_3$) δ (ppm): 8.32 (s, 1H), 7.73 – 7.68 (m, 2H), 7.37 – 7.31 (m, 3H), 7.29 – 7.23 (m, 4H), 7.21 – 7.16 (m, 1H), 4.75 (s, 2H). ^{13}C{^{1}H} NMR (150 MHz, $CDCl_3$) δ (ppm): 162.2, 139.5, 136.4, 131.0, 128.8, 128.7, 128.5, 128.2, 127.2, 65.3. IR (neat): ν_{max} = 3062, 2840, 1643, 1461, 1220 cm^{-1}. R_f 0.6 (Hex/TEA, 20/1).

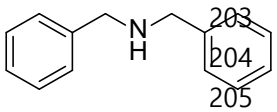

Synthesis of 1c. An oven-dried reaction vial equipped with a magnetic stir bar was charged with **1a** (11 mg, 0.10 mmol), $[\mathbf{Co}]^{2+}$ (1.1 mg, 1.0 mol%), $[Ru(bpy)_3]^{2+}$ (0.8 mg, 1.0 mol%), a Hantzsch ester (50 mg, 0.20 mmol), and anhydrous CH_3CN (1.0 mL). The vial was sealed with a screw cap fitted with a PTFE/silicone septum, through which molecular oxygen was introduced by bubbling via a needle connected to an oxygen balloon for 10 min. The reaction mixture was then stirred under irradiation with 1050-nm LEDs (3 W) for 3 days, followed by irradiation with 450-nm LEDs for an additional 24 h. Upon completion of the reaction, as monitored by TLC, the solvent was removed under reduced pressure. The resulting residue was purified by flash column chromatography on a silica gel using dichloromethane as an eluent, affording **1c** as a brown solid in a 21% yield (4.1 mg). ^{1}H NMR (400 MHz, $CDCl_3$) δ (ppm): 7.20 – 7.34 (m, 10H), 3.80 (s, 4H). R_f 0.33 (Hex/EtOAc, 5/1). ^{13}C{^{1}H} NMR (100 MHz, $CDCl_3$) δ (ppm): 140.4, 128.5, 128.2, 127.0, 53.24.

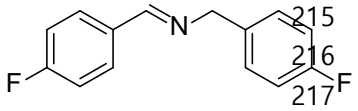

Synthesis of 2b. The method identical to that for **1b** was employed, except the use of 4-fluorobenzylamine (**2a**, 13 mg, 0.1 mmol) in place of **1a**. Colorless oil (54%, 12 mg). ^{1}H NMR (600 MHz, CD_2Cl_2) δ (ppm): 8.35 (s, 1H), 7.77 (dd, J = 7.9, 5.6 Hz, 2H), 7.30 (dd, J = 7.9, 5.6 Hz, 2H), 7.10 (t, J = 8.8 Hz, 2H), 7.03 (t, J = 8.8 Hz, 2H), 4.77 (s, 2H). ^{13}C{^{1}H} NMR (150 MHz, CD_2Cl_2) δ (ppm): 164.7 (d, J = 251.1 Hz), 162.2 (d, J = 244.8 Hz), 160.7, 135.2, 132.5, 130.4 (d, J = 8.7 Hz), 129.7 (d, J = 8.0 Hz), 116.0 (d, J = 21.9 Hz), 115.6 (d, J = 21.4 Hz), 64.4. ^{19}F NMR (564 MHz, $CDCl_3$) δ (ppm): −109.25, −116.01. IR (neat): ν_{max} = 3043, 2840, 1648, 1508, 1228, 1152 cm^{-1}. R_f 0.6 (Hex/TEA, 20/1).

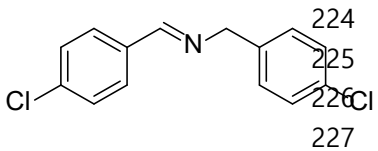

Synthesis of 3b. The method identical to that for **1b** was employed, except the use of 4-chlorobenzylamine (**3a**, 14 mg, 0.1 mmol) in place of **1a**. Yellow oil (57%, 15 mg). ^{1}H NMR (600 MHz, $CDCl_3$) δ (ppm): 8.27 (s, 1H), 7.64 (d, J = 8.5 Hz, 2H), 7.32 (d, J = 8.5 Hz, 2H), 7.24 (d, J = 8.2 Hz, 2H), 7.19 (d, J = 8.2 Hz, 2H), 4.70 (s, 2H). ^{13}C{^{1}H} NMR (150 MHz, $CDCl_3$) δ (ppm): 161.1, 137.8, 137.1, 134.7, 133.1, 129.7, 129.5, 129.2, 128.9, 64.4. IR (neat): ν_{max} = 2975, 2835, 1644, 1490, 1404 cm^{-1}. R_f 0.6 (Hex/TEA, 20/1).

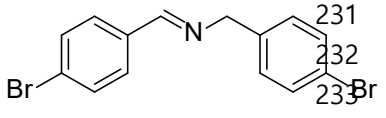

Synthesis of 4b. The method identical to that for **1b** was employed, except the use of 4-bromobenzylamine (**4a**, 19 mg, 0.1 mmol) in place of **1a**. White solid (63%, 22 mg). ^{1}H NMR (600 MHz, $CDCl_3$) δ (ppm): 8.33 (s, 1H), 7.64 (d, J = 8.3 Hz, 2H), 7.55 (d, J = 8.3 Hz, 2H), 7.47 (d, J = 8.2 Hz, 2H), 7.21 (d, J = 8.2 Hz, 2H), 4.75 (s, 2H).

$^{13}C\{^1H\}$ NMR (150 MHz, $CDCl_3$) δ (ppm): 161.2, 138.3, 135.1, 132.1, 131.8, 129.9, 129.8, 125.6, 121.1, 64.4. IR (neat): ν_{max} = 2835, 2815, 1645, 1586, 1487, 1401 cm^{-1}. R_f 0.6 (Hex/TEA, 20/1).

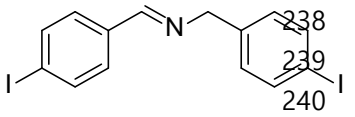

Synthesis of 5b. The method identical to that for **1b** was employed, except the use of 4-iodobenzylamine (**5a**, 24 mg, 0.1 mmol) in place of **1a**. White solid (63%, 18 mg). ^1H NMR (400 MHz, $CDCl_3$) δ (ppm): 8.30 (s, 1H), 7.76 (d, J = 8.4 Hz, 2H), 7.66 (d, J = 8.4 Hz, 2H), 7.49 (d, J = 8.4 Hz, 2H), 7.08 (d, J = 8.4 Hz, 2H), 4.73 (s, 2H). $^{13}C\{^1H\}$ NMR (101 MHz, $CDCl_3$) δ (ppm): 161.46, 138.92, 138.06, 137.80, 137.77, 135.58, 130.13, 129.94, 129.46, 64.50. R_f 0.6 (Hex/TEA, 20/1).

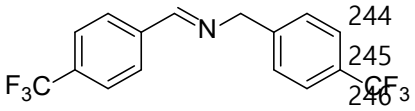

Synthesis of 6b. The method identical to that for **1b** was employed, except the use of 4-trifluoromethylbenzylamine (**6a**, 18 mg, 0.1 mmol) in place of **1a**. Yellow oil (83%, 27 mg). ^1H NMR (600 MHz, $CDCl_3$) δ (ppm): 8.47 (s, 1H), 7.91 (d, J = 8.1 Hz, 2H), 7.69 (d, J = 8.1 Hz, 2H), 7.62 (d, J = 8.0 Hz, 2H), 7.48 (d, J = 8.0 Hz, 2H), 4.90 (s, 2H). $^{13}C\{^1H\}$ NMR (150 MHz, $CDCl_3$) δ (ppm): 161.3, 143.2, 139.2, 132.8 (q, J = 32.7 Hz), 129.7 (q, J = 32.4 Hz), 128.7, 128.3, 125.9 (q, J = 3.8 Hz), 125.7 (q, J = 3.8 Hz), 124.4 (q, J = 272.2 Hz), 123.7 (q, J = 272.8 Hz), 64.6. ^{19}F NMR (564 MHz, $CDCl_3$) δ (ppm): –62.48, –62.86. IR (neat): ν_{max} = 2987, 2903, 1645, 1260, 1169 cm^{-1}. R_f 0.6 (Hex/EtOAc/TEA, 20/4/1).

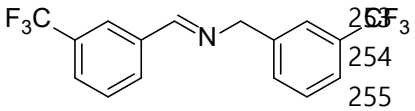

Synthesis of 7b. The method identical to that for **1b** was employed, except the use of 3-trifluoromethylbenzylamine (**7a**, 18 mg, 0.1 mmol) in place of **1a**. Colorless oil (70%, 23 mg). ^1H NMR (600 MHz, $CDCl_3$) δ (ppm): 8.06 (s, 1H), 7.98 (d, J = 7.8 Hz, 1H), 7.70 (d, J = 7.8 Hz, 1H), 7.61 (s, 1H), 7.58 – 7.53 (m, 3H), 7.48 (t, J = 7.7 Hz, 1H), 4.89 (s, 2H). $^{13}C\{^1H\}$ NMR (150 MHz, $CDCl_3$) δ (ppm): 161.2, 140.1, 136.8, 131.7 (d, J = 1.5 Hz), 131.5 (d, J = 1.3 Hz), 129.4, 129.2, 127.7 (q, J = 3.8 Hz), 125.3 (q, J = 3.8 Hz), 124.7 (q, J = 3.8 Hz), 124.2 (q, J = 3.8 Hz), 124.2 (q, J = 272.5 Hz), 124.1 (q, J = 272.5 Hz), 123.5, 123.2, 64.7. ^{19}F NMR (564 MHz, $CDCl_3$) δ (ppm): –62.9, –63.0. IR (neat): ν_{max} = 2987, 2886, 1649, 1258, 1163 cm^{-1}. R_f 0.6 (Hex/EtOAc/TEA, 20/1).

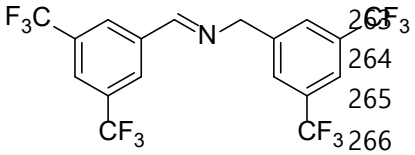

Synthesis of 8b. The method identical to that for **1b** was employed, except the use of 3,5-bis(trifluoromethyl)benzylamine (**8a**, 24 mg, 0.1 mmol) in place of **1a**. Yellow solid (52%, 24 mg). ^1H NMR (600 MHz, $CDCl_3$) δ (ppm): 8.55 (s, 1H), 8.25 (s, 2H), 7.97 (s, 1H), 7.84 – 7.82 (m, 3H), 4.97 (s, 2H). $^{13}C\{^1H\}$ NMR (150 MHz, $CDCl_3$) δ (ppm): 160.3, 141.2, 137.7, 132.6 (q, J = 33.8 Hz), 132.1 (q, J = 33.3 Hz), 128.5, 128.3, 124.8, 123.6 (q, J = 273.1 Hz), 123.0 (q, J = 272.8 Hz), 121.6, 64.1. ^{19}F NMR (564 MHz, $CDCl_3$) δ (ppm): –62.87, –63.03. IR (neat): ν_{max} = 2989, 2893, 1655, 1278, 1171 cm^{-1}. R_f 0.5 (Hex/TEA, 20/1).

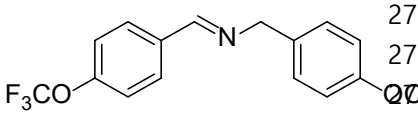

Synthesis of 9b. The method identical to that for **1b** was employed, except the use of 4-(trifluoromethoxy)benzylamine (**9a**, 19 mg, 0.1 mmol) in place of **1a**. Yellow oil (80%, 29 mg). ^1H NMR (600 MHz, $CDCl_3$) δ (ppm): 8.39 (s, 1H), 7.82 (d, J = 8.4 Hz, 2H), 7.36 (d, J = 8.4 Hz, 2H), 7.27 (d, J = 8.2 Hz, 2H), 7.20 (d, J = 8.2 Hz, 2H), 4.81 (s, 2H). $^{13}C\{^1H\}$ NMR (150 MHz, $CDCl_3$) δ (ppm): 160.8, 151.3, 148.5, 138.1, 134.7, 130.0, 129.4, 121.3, 121.1, 120.7 (q, J = 256.9), 120.6 (q, J = 258.1), 64.3. ^{19}F NMR (564 MHz, $CDCl_3$) δ (ppm): –57.75, –57.94. IR (neat): ν_{max} = 2987, 2866, 1647, 1513, 1251, 1172 cm^{-1}. R_f 0.5 (Hex/EtOAc/TEA, 20/5/1).

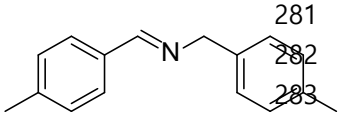

Synthesis of 10b. The method identical to that for **1b** was employed, except the use of 4-methylbenzylamine (**10a**, 12 mg, 0.1 mmol) in place of **1a**. Colorless oil (70%, 16 mg). ^{1}H NMR (600 MHz, $CDCl_3$) δ (ppm): 8.34 (s, 1H), 7.67 (d, J = 7.8 Hz, 2H), 7.24 – 7.20 (m, 4H), 7.15 (d, J = 7.8 Hz, 2H), 4.77 (s, 2H), 2.38 (s, 3H), 2.34 (s, 3H). ^{13}C{^{1}H} NMR (150 MHz, $CDCl_3$) δ (ppm): 161.9, 136.7, 136.5, 129.5, 129.4, 128.5, 128.2, 65.0, 21.7, 21.3. IR (neat): ν_{max} = 2974, 2865, 1650, 1418, 1324 cm^{-1}. R_f 0.6 (Hex/TEA, 20/1).

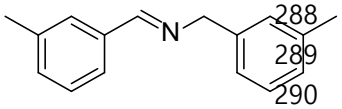

Synthesis of 11b. The method identical to that for **1b** was employed, except the use of 3-methylbenzylamine (**11a**, 13 mg, 0.1 mmol) in place of **1a**. Colorless oil (61%, 14 mg). ^{1}H NMR (600 MHz, $CDCl_3$) δ (ppm): 8.36 (s, 1H), 7.65 (s, 1H), 7.54 (d, J = 7.6 Hz, 1H), 7.31 (t, J = 7.7 Hz, 1H), 7.25 – 7.21 (m, 2H), 7.16 – 7.12 (m, 2H), 7.08 (d, J = 7.6 Hz, 1H), 4.78 (s, 2H), 2.38 (s, 3H), 2.35 (s, 3H). ^{13}C{^{1}H} NMR (150 MHz, $CDCl_3$) δ (ppm): 162.3, 139.4, 138.6, 138.3, 136.3, 131.8, 129.0, 128.7, 128.6, 128.6, 127.9, 126.1, 125.3, 65.4, 21.6, 21.5. IR (neat): ν_{max} = 2975, 2882, 1639, 1489, 1288 cm^{-1}. R_f 0.6 (Hex/TEA, 20/1).

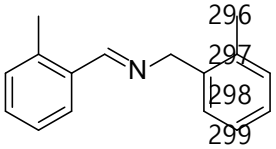

Synthesis of 12b. The method identical to that for **1b** was employed, except the use of 2-methylbenzylamine (**12a**, 12 mg, 0.1 mmol) in place of **1a**. Colorless oil (58%, 13 mg). ^{1}H NMR (600 MHz, $CDCl_3$) δ (ppm): 8.68 (s, 1H), 7.93 (dd, J = 7.8, 1.5 Hz, 1H), 7.32 – 7.28 (m, 2H), 7.24 (t, J = 7.5 Hz, 1H), 7.21 – 7.17 (m, 4H), 4.83 (s, 2H), 2.51 (s, 3H). ^{13}C{^{1}H} NMR (150 MHz, $CDCl_3$) δ (ppm): 160.8, 137.9, 137.8, 136.3, 134.5, 131.0, 130.5, 130.3, 128.5, 127.9, 127.3, 126.4, 126.3, 63.5, 19.6, 19.5. IR (neat): ν_{max} = 2960, 2867, 1644, 1487, 1257 cm^{-1}. R_f 0.6 (Hex/TEA, 20/1).

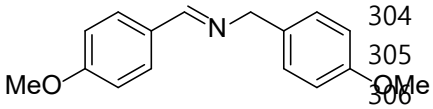

Synthesis of 13b. The method identical to that for **1b** was employed, except the use of 4-methoxybenzylamine (**13a**, 14 mg, 0.1 mmol) in place of **1a**. Yellow oil (60%, 15 mg). ^{1}H NMR (600 MHz, $CDCl_3$) δ (ppm): 8.30 (s, 1H), 7.71 (d, J = 8.7 Hz, 2H), 7.25 (d, J = 8.7 Hz, 2H), 6.92 (d, J = 8.7 Hz, 2H), 6.88 (d, J = 8.7 Hz, 2H), 4.73 (s, 2H), 3.84 (s, 3H), 3.80 (s, 3H). ^{13}C{^{1}H} NMR (150 MHz, $CDCl_3$) δ (ppm): 162.0, 161.3, 158.9, 132.2, 130.2, 130.2, 129.4, 114.2, 114.1, 64.3, 55.6, 55.5. IR (neat): ν_{max} = 2960, 2901, 2835, 1644, 1511, 1247 cm^{-1}. R_f 0.5 (Hex/EtOAc/TEA, 20/5/1).

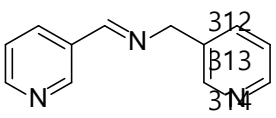

Synthesis of 14b. The method identical to that for **1b** was employed, except the use of 3-(aminomethyl)pyridine (**14a**, 11 mg, 0.1 mmol) in place of **1a**. Colorless oil (21%, 4.1 mg). ^{1}H NMR (600 MHz, $CDCl_3$) δ (ppm): 8.90 (s, 1H), 8.67 (d, J = 4.8 Hz, 1H), 8.62 (s, 1H), 8.54 (d, J = 4.8 Hz, 1H), 8.47 (s, 1H), 8.16 (d, J = 8.0 Hz, 1H), 7.69 (d, J = 8.0 Hz, 1H), 7.36 (dd, J = 8.0, 4.8 Hz, 1H), 7.29 (dd, J = 8.0, 4.8 Hz, 1H), 4.85 (s, 2H). ^{13}C{^{1}H} NMR (150 MHz, $CDCl_3$) δ (ppm): 160.0, 152.1, 150.6, 149.6, 148.9, 135.8, 134.8, 134.6, 131.6, 124.0, 123.7, 62.7. IR (neat): ν_{max} = 2988, 2884, 1646, 1575, 1423, 1252 cm^{-1}. R_f 0.4 (CH_2Cl_2/CH_3OH/TEA, 20/4/1).

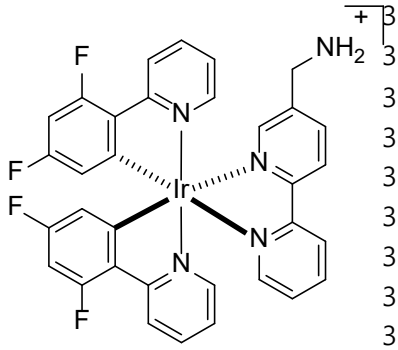

Synthesis of 15a. An anhydrous CH_2Cl_2 (50 mL) solution containing dichlorotetrakis[3,5-difluoro-2-(2-pyridiny)phenyl]diiridium(III) (0.57 g, 0.47 mmol), and 2,2′-bipyridine-5-methanamine (0.13 g, 0.71 mmol) was refluxed for 6 h in the dark. The reaction mixture was cooled to room temperature, and NH_4PF_6 (15 equiv) was slowly added to the solution. After 12 h, the reaction mixture was filtered to remove residual NH_4PF_6 and concentrated under vacuum. The crude mixture was subjected to column chromatography on silica gel with CH_2Cl_2 to CH_2Cl_2:CH_3OH = 9:1 as eluents. A yellow powder was obtained in a 56% yield (0.36 g). ^{1}H NMR (400 MHz, CD_2Cl_2) δ (ppm): 8.46 – 8.51 (m, 2H), 8.32 (d, J = 8.8 Hz, 2H), 8.14 – 8.22 (m, 2H), 7.97 – 8.04 (m, 2H), 7.82 – 7.86 (t, J = 8.0 Hz, 2H), 7.47 – 7.52 (m, 3H), 7.03 – 7.07 (m, 2H), 6.58 – 6.64 (m, 2H), 5.71 – 5.77 (m, 2H), 3.89 (s, 2H), 1.26 (s, 2H). ^{13}C{^{1}H} NMR (100 MHz, CD_2Cl_2) δ (ppm): 156.07, 154.12, 150.85 149.74, 149.22, 148.99, 145.05, 140.41, 139.60, 139.33, 128.66, 125.09, 125.03, 124.41, 124.17, 124.03, 99.49, 99.22, 43.14. ^{19}F NMR (282 MHz, CD_2Cl_2) δ (ppm): –73.05 (d, J = 705 Hz), –106.38, –109.04.

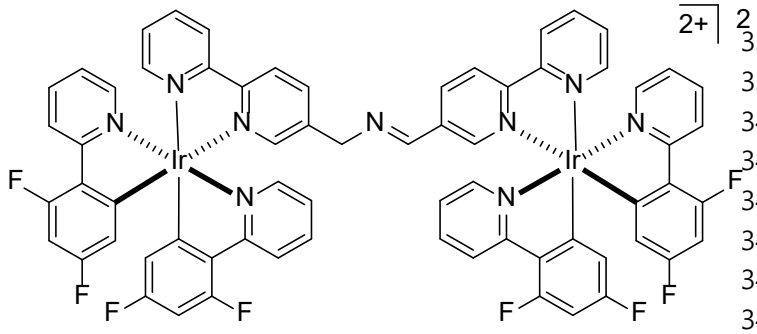

Synthesis of 15b. The method identical to that for **1a** was employed, except the use of **15a** (36 mg, 0.04 mmol) in place of benzylamine. A brown solid was obtained in a 20% yield (7.1 mg). ^{1}H NMR (400 MHz, $CDCl_3$) δ (ppm): 8.62 (t, J = 8.0 Hz, 3H), 8.48 (d, J = 8.4 Hz, 2H), 8.39 (s, 2H), 8.31 (d, J = 10.0 Hz, 4H), 8.29 (d, J = 8.4 Hz, 2H), 8.17 (d, J = 6.8 Hz, 2H), 8.14 (m, 2H), 7.98 (d, J = 6.0 Hz, 2H), 7.82 (m, 4H), 7.57 – 7.51 (m, 4H), 7.40 (d, J = 5.2 Hz, 2H), 7.15 (m, 2H), 7.02 (m, 4H), 6.57 (m, 4H), 5.65 (t, J = 8.0 Hz, 4H), 3.90 (s, 2H). ^{13}C{^{1}H} NMR (100 MHz, $CDCl_3$) δ (ppm): 162.74, 161.69, 150.21, 149.60, 149.20, 148.66, 139.28, 137.28, 136.81, 128.97, 127.53, 123.83, 121.33, 121,19, 116.55, 113.99, 60.50, 58.50, 53.56, 29.79, 23.18, 22.78, 21.15, 18.50, 14.29, 14.22, 9.89, 1.97. ^{19}F NMR (377 MHz, $CDCl_3$) δ (ppm): –72.21 (d, J = 713 Hz), –105.39, –108.31.

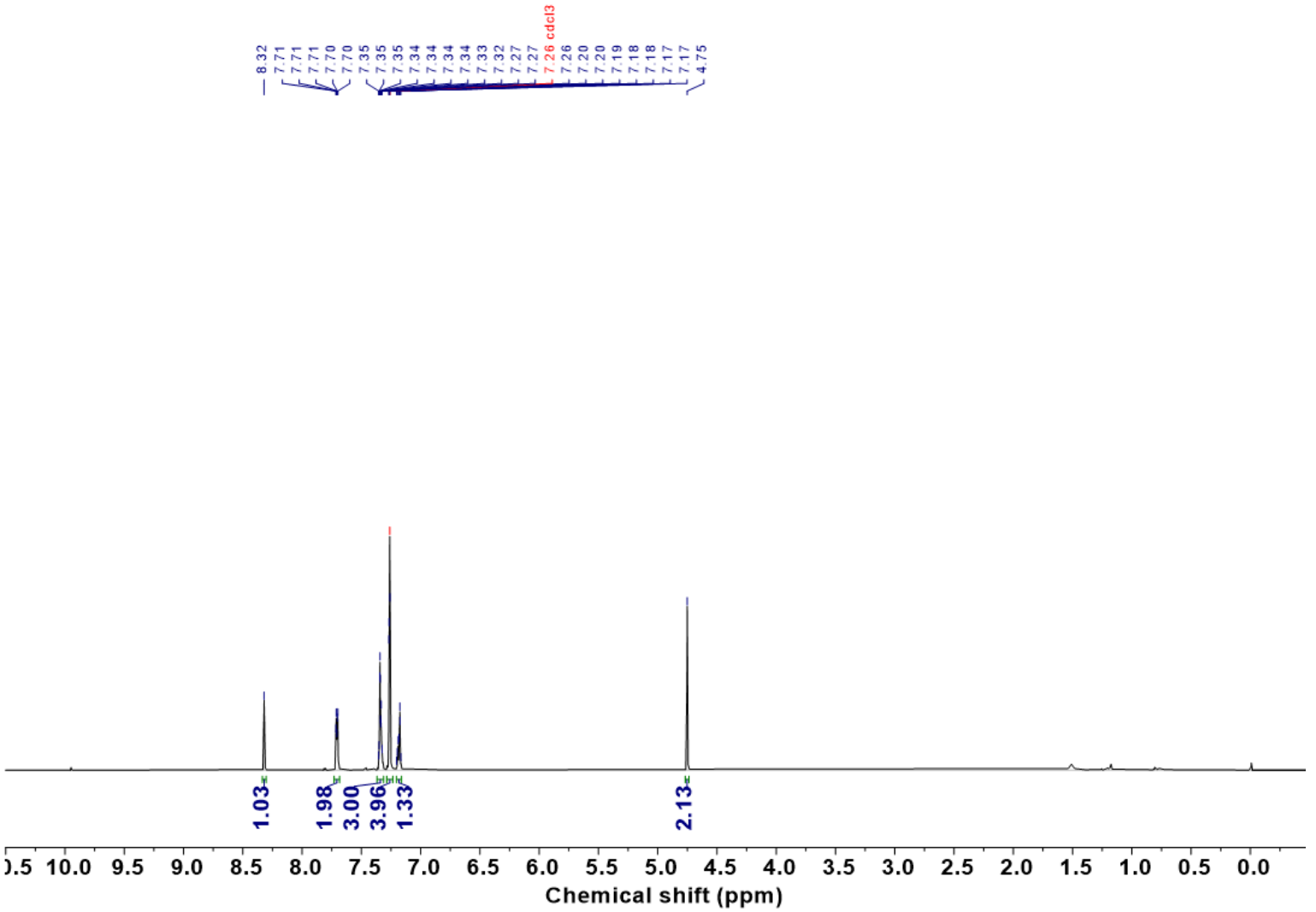

Supplementary Fig. 10 | ^{1}H NMR (600 MHz, $CDCl_3$) spectrum of 1b.

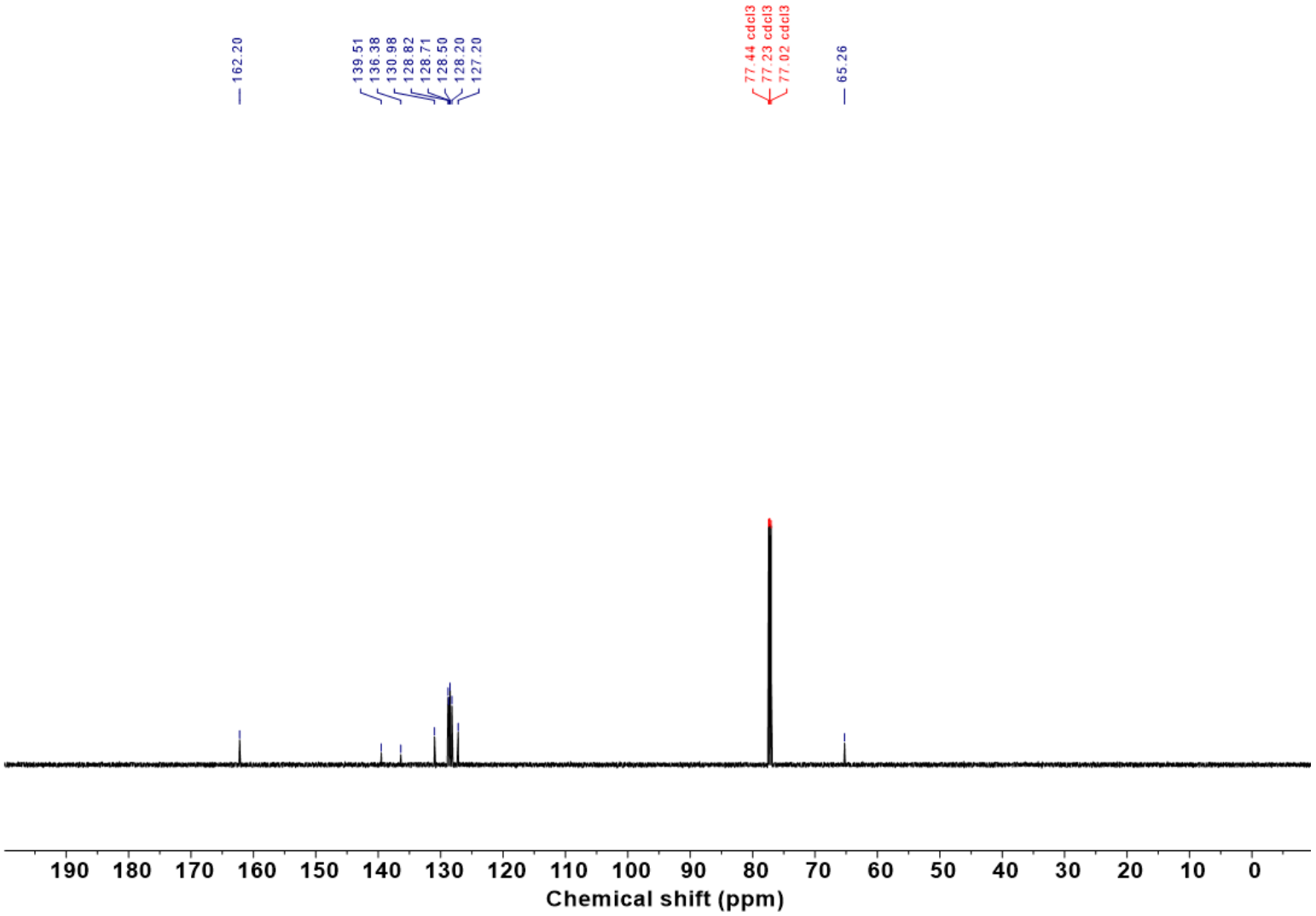

Supplementary Fig. 11 | $^{13}C\{^{1}H\}$ NMR (150 MHz, $CDCl_3$) spectrum of 1b.

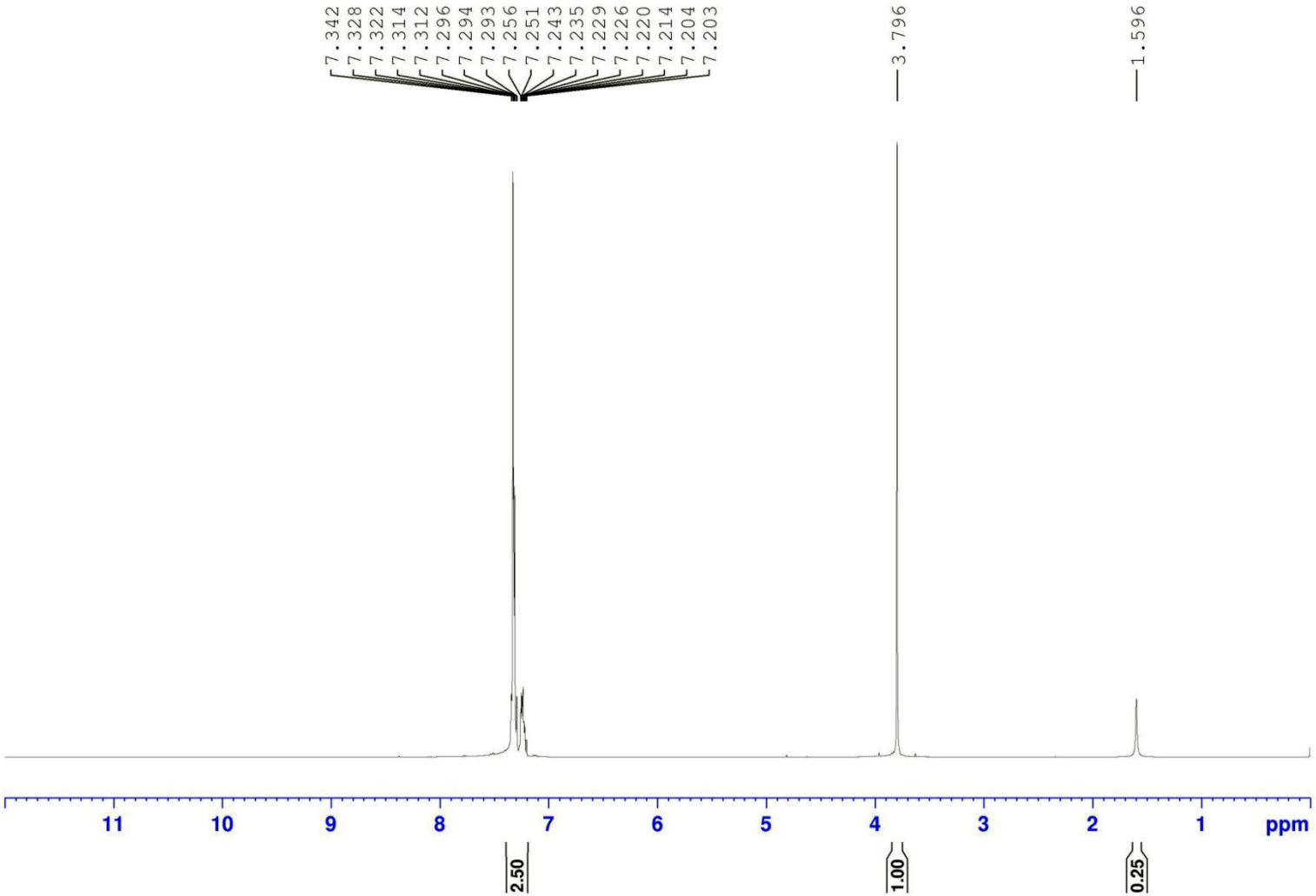

Supplementary Fig. 12 | ^{1}H NMR (400 MHz, $CDCl_3$) spectrum of 1c.

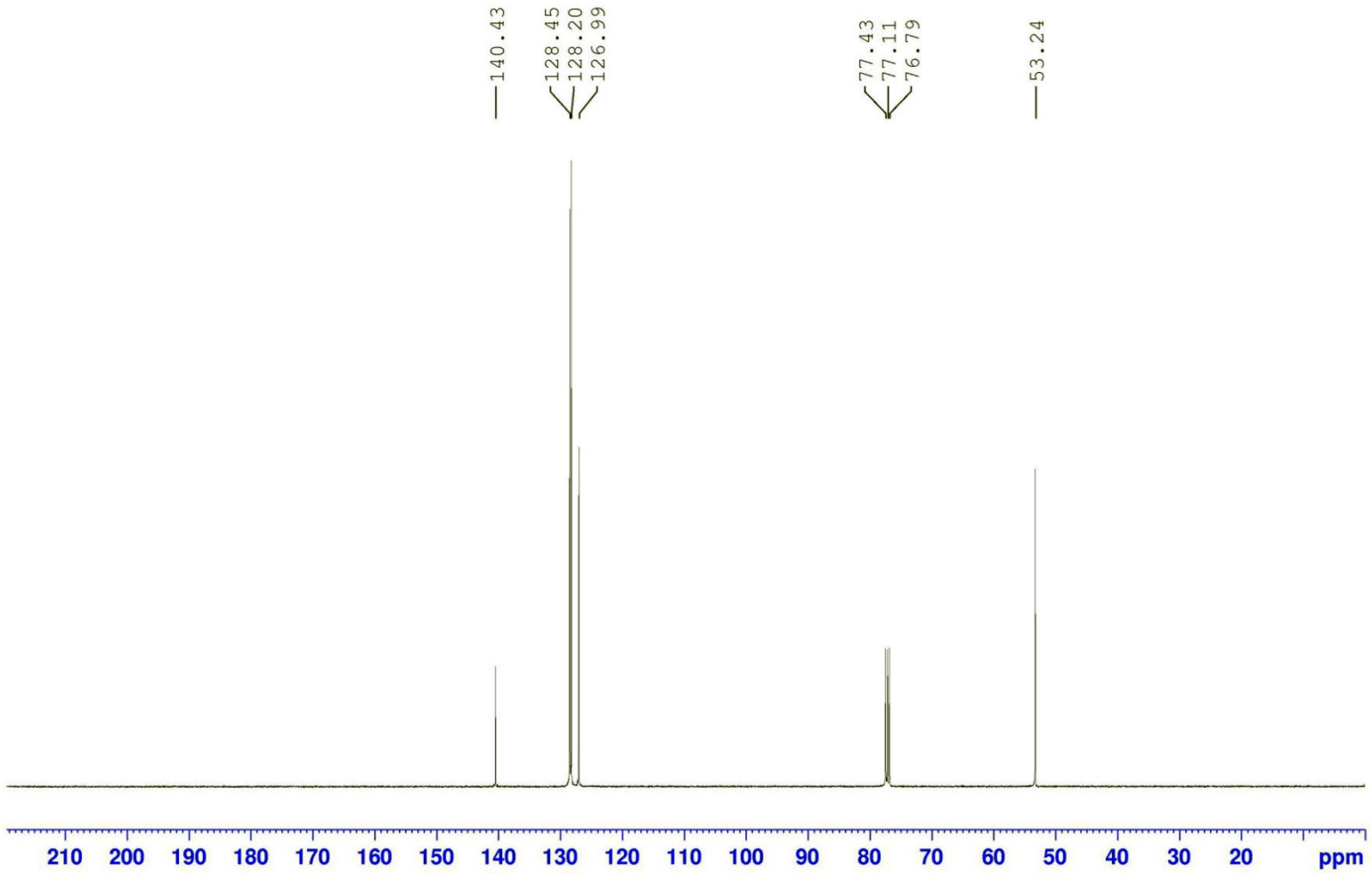

Supplementary Fig. 13 | $^{13}C\{^{1}H\}$ NMR (100 MHz, $CDCl_3$) spectrum of 1c.

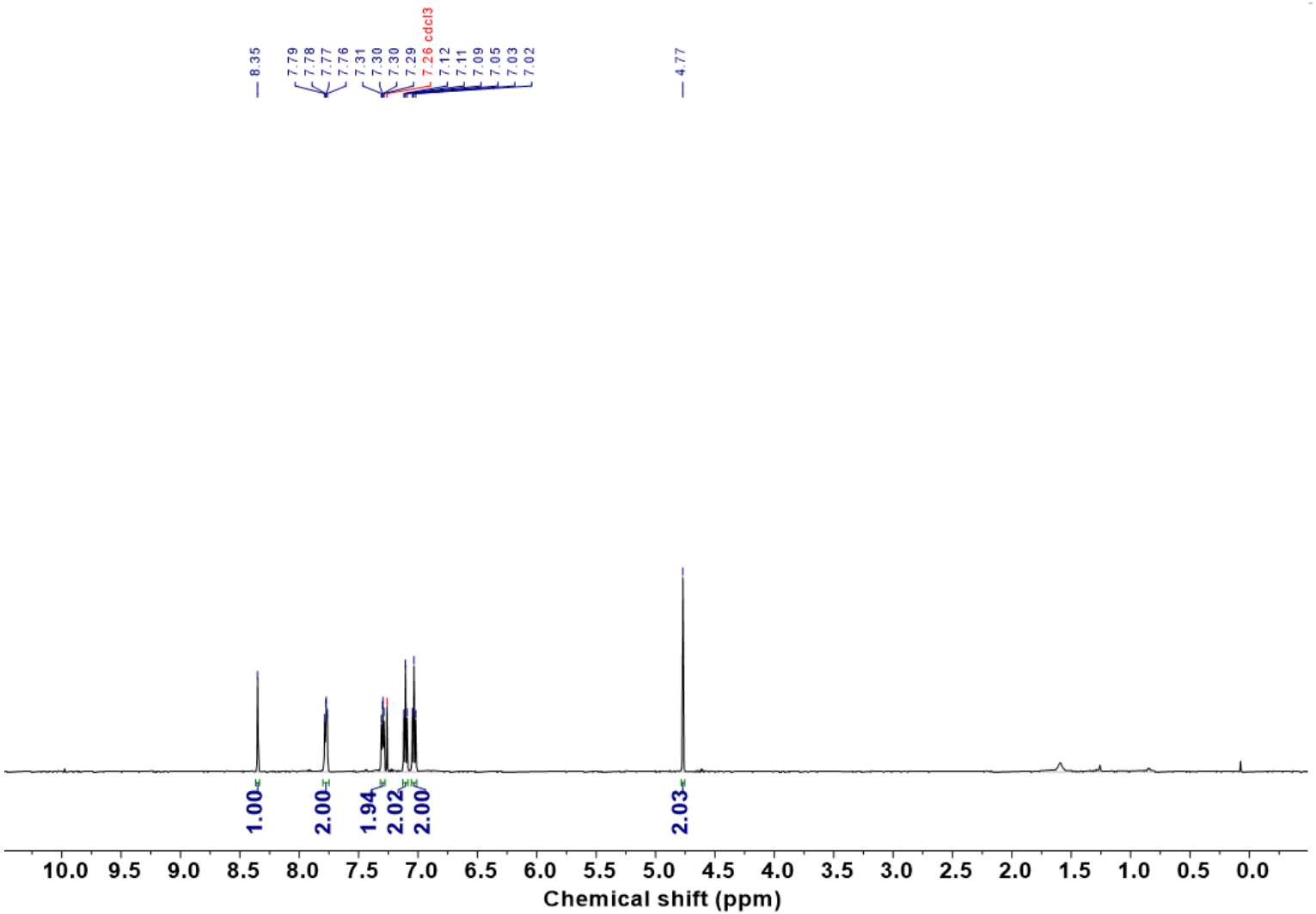

Supplementary Fig. 14 | ^{1}H NMR (600 MHz, $CDCl_3$) spectrum of 2b.

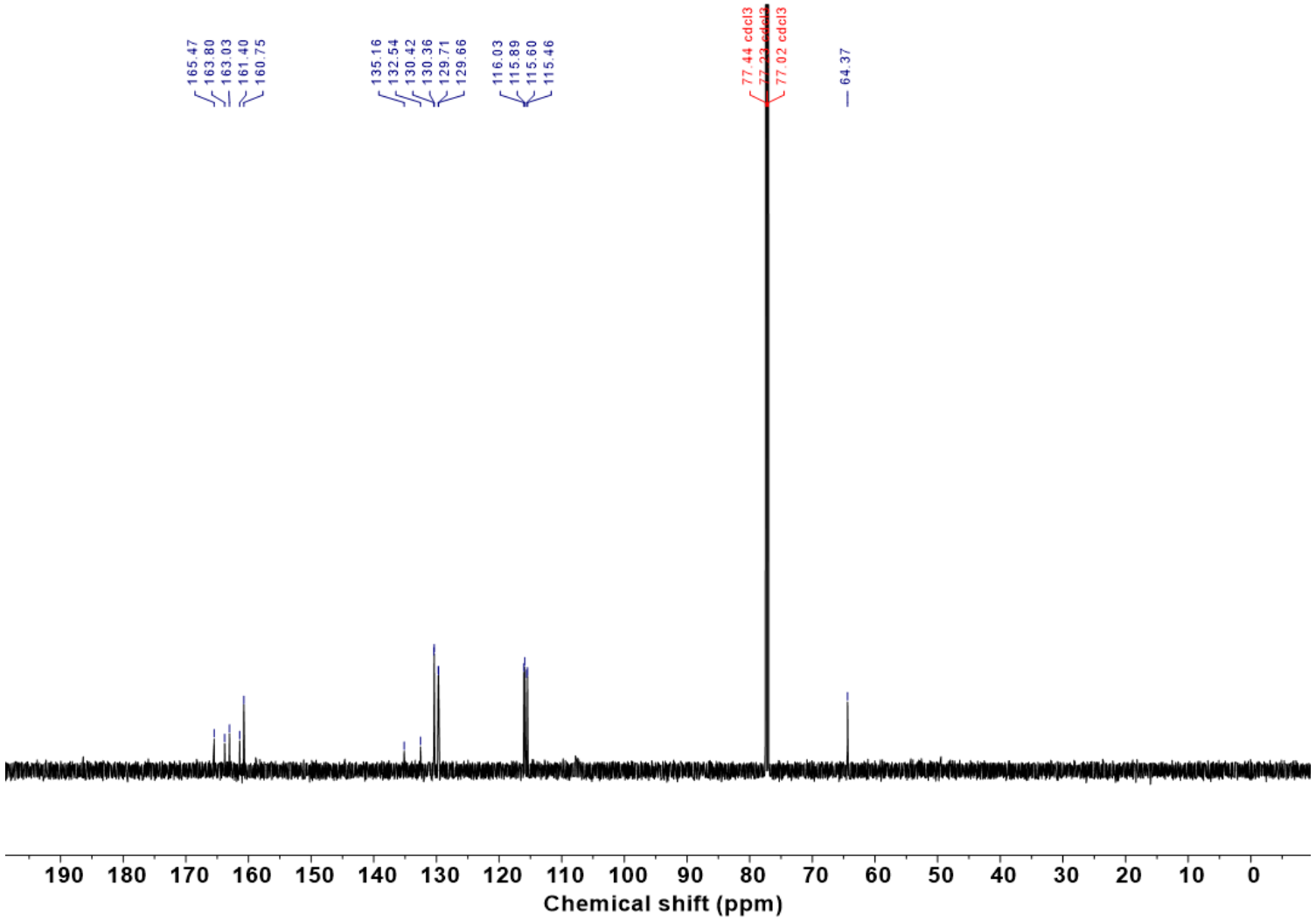

Supplementary Fig. 15 | $^{13}C\{^{1}H\}$ NMR (150 MHz, $CDCl_3$) spectrum of 2b.

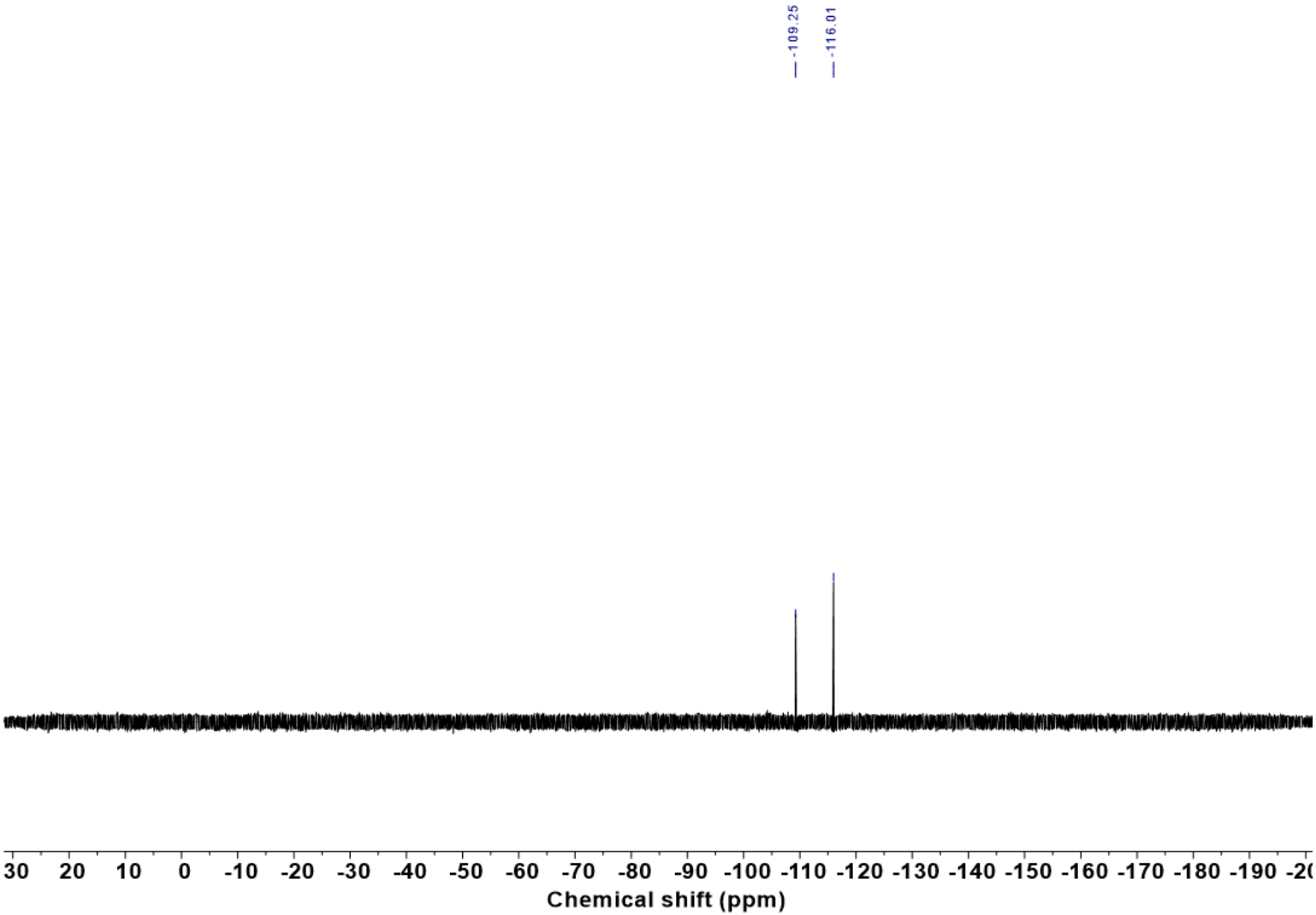

Supplementary Fig. 16 | ^{19}F NMR (564 MHz, $CDCl_3$) spectrum of 2b.

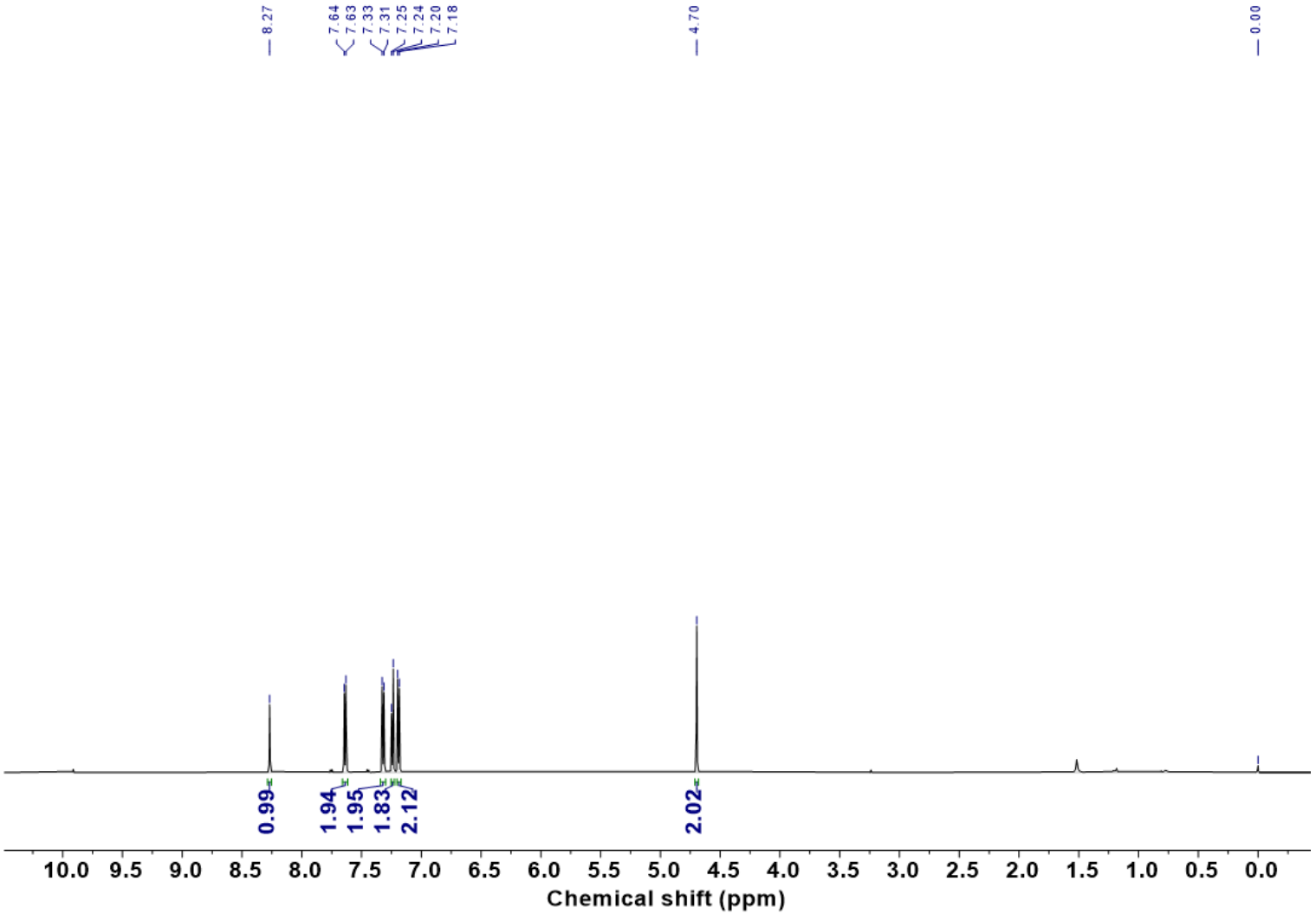

Supplementary Fig. 17 | ^{1}H NMR (600 MHz, $CDCl_3$) spectrum of 3b.

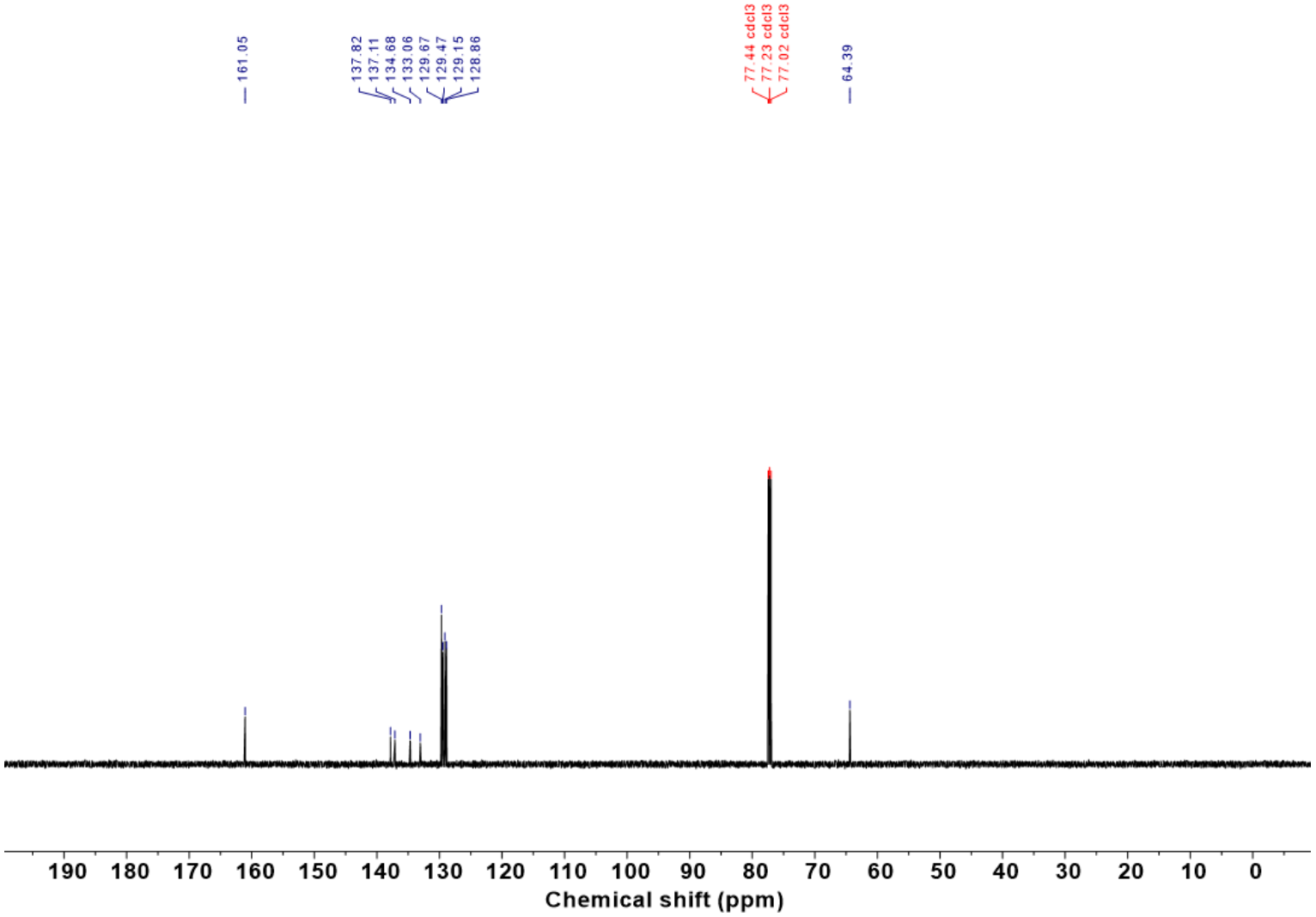

Supplementary Fig. 18 | $^{13}C\{^{1}H\}$ NMR (150 MHz, $CDCl_3$) spectrum of 3b.

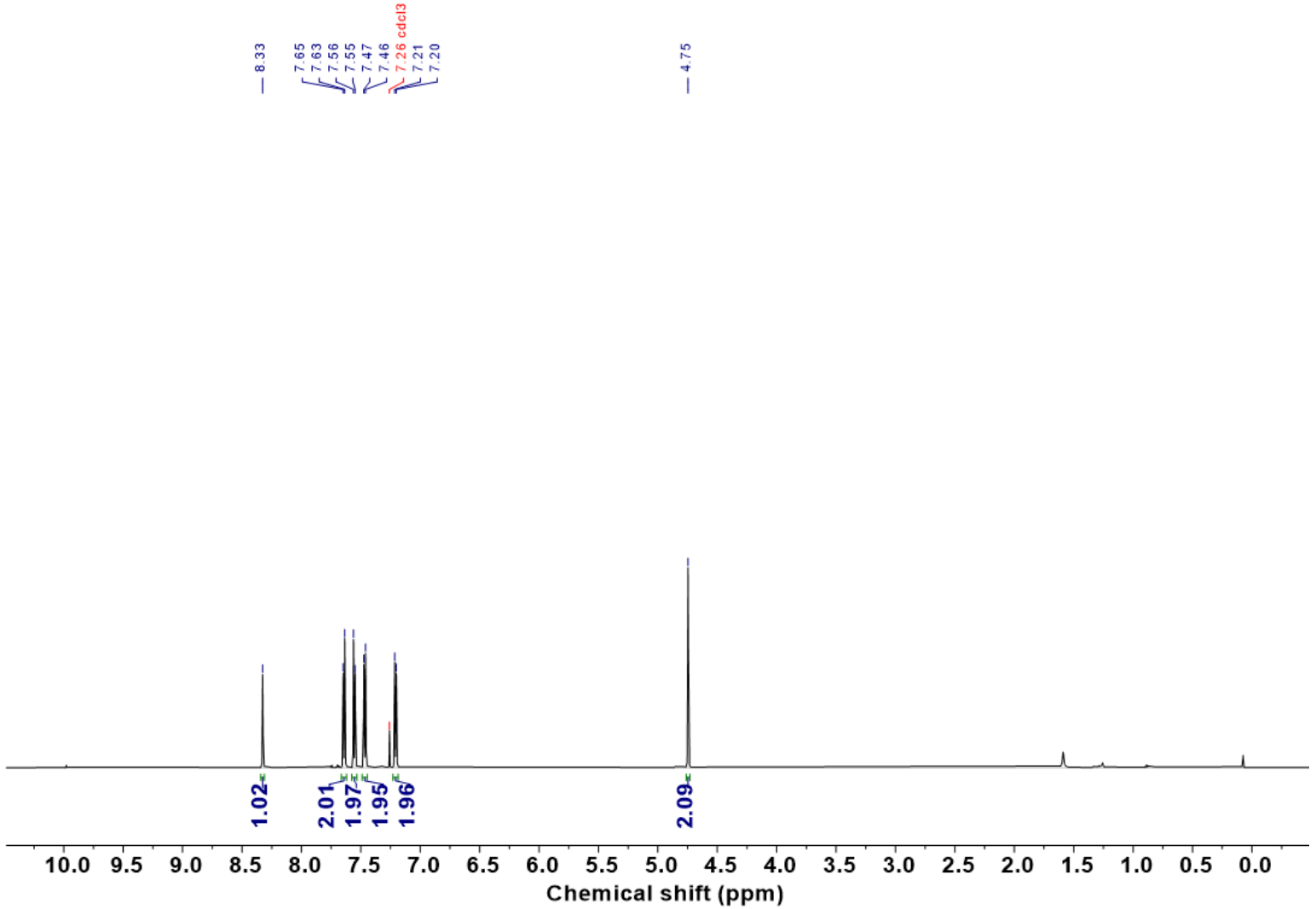

Supplementary Fig. 19 | ^{1}H NMR (600 MHz, $CDCl_3$) spectrum of 4b.

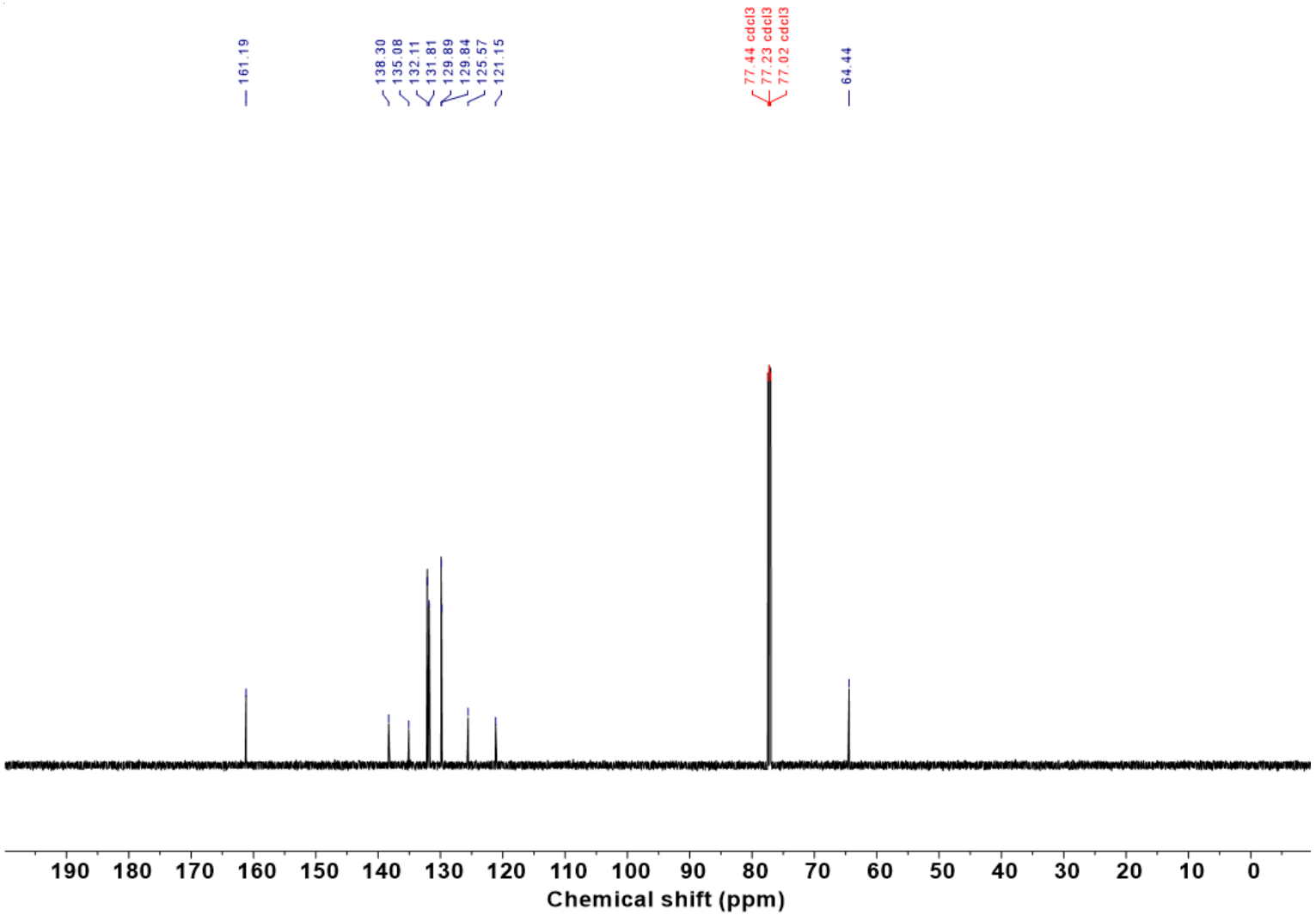

Supplementary Fig. 20 | $^{13}C\{^{1}H\}$ NMR (150 MHz, $CDCl_3$) spectrum of 4b.

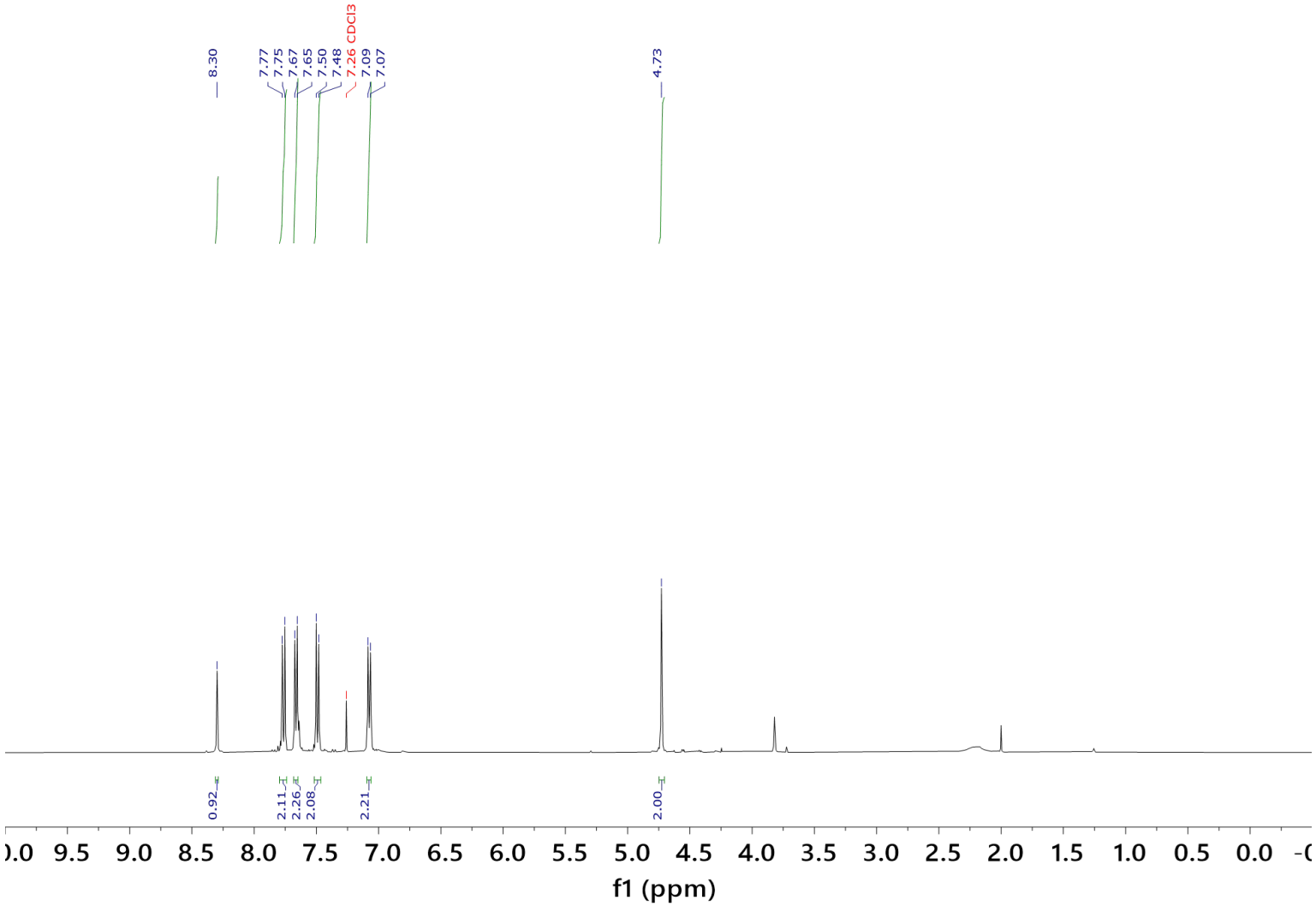

Supplementary Fig. 21 | ^{1}H NMR (600 MHz, $CDCl_3$) spectrum of 5b.

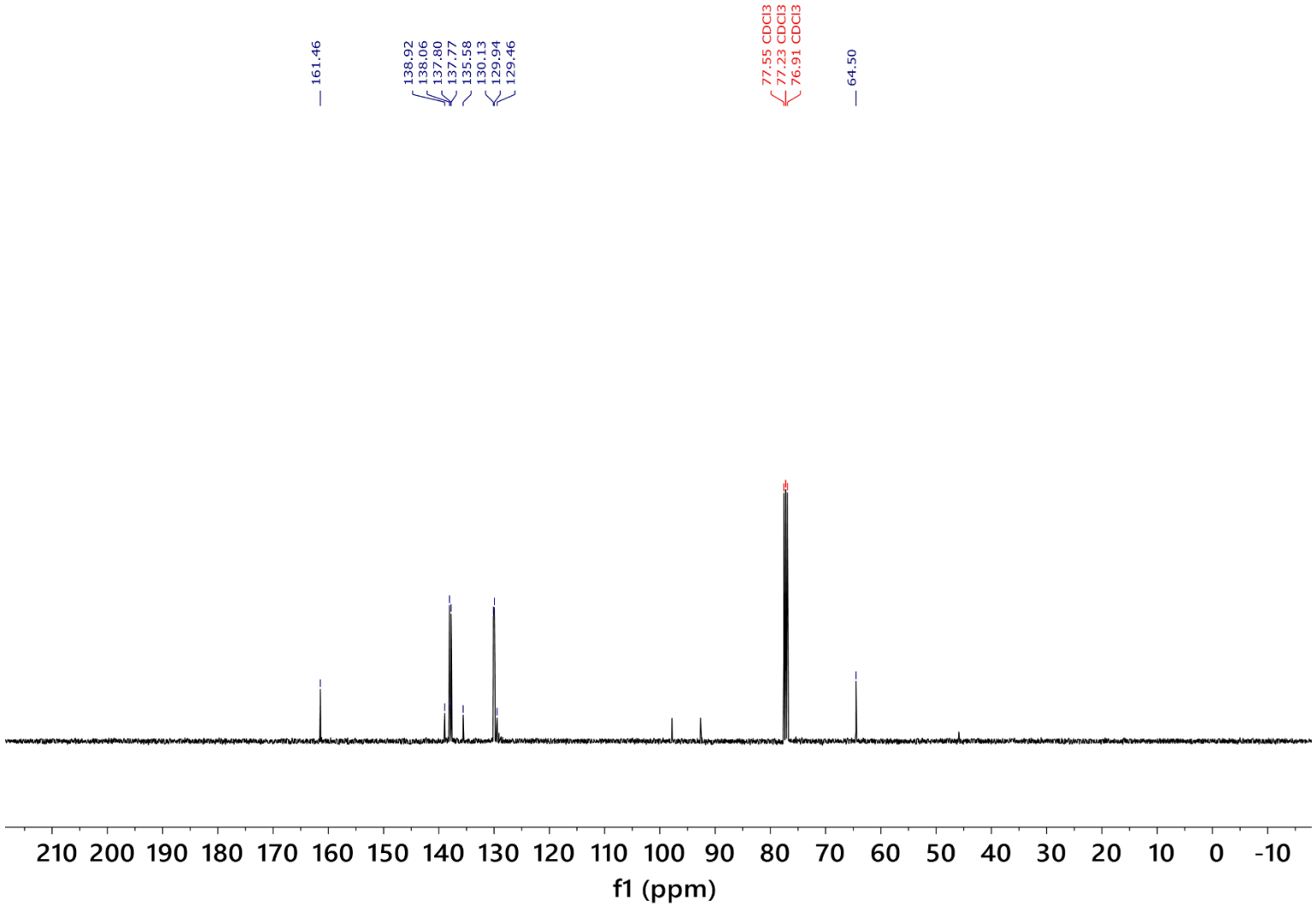

Supplementary Fig. 22 | $^{13}C\{^{1}H\}$ NMR (150 MHz, $CDCl_3$) spectrum of 5b.

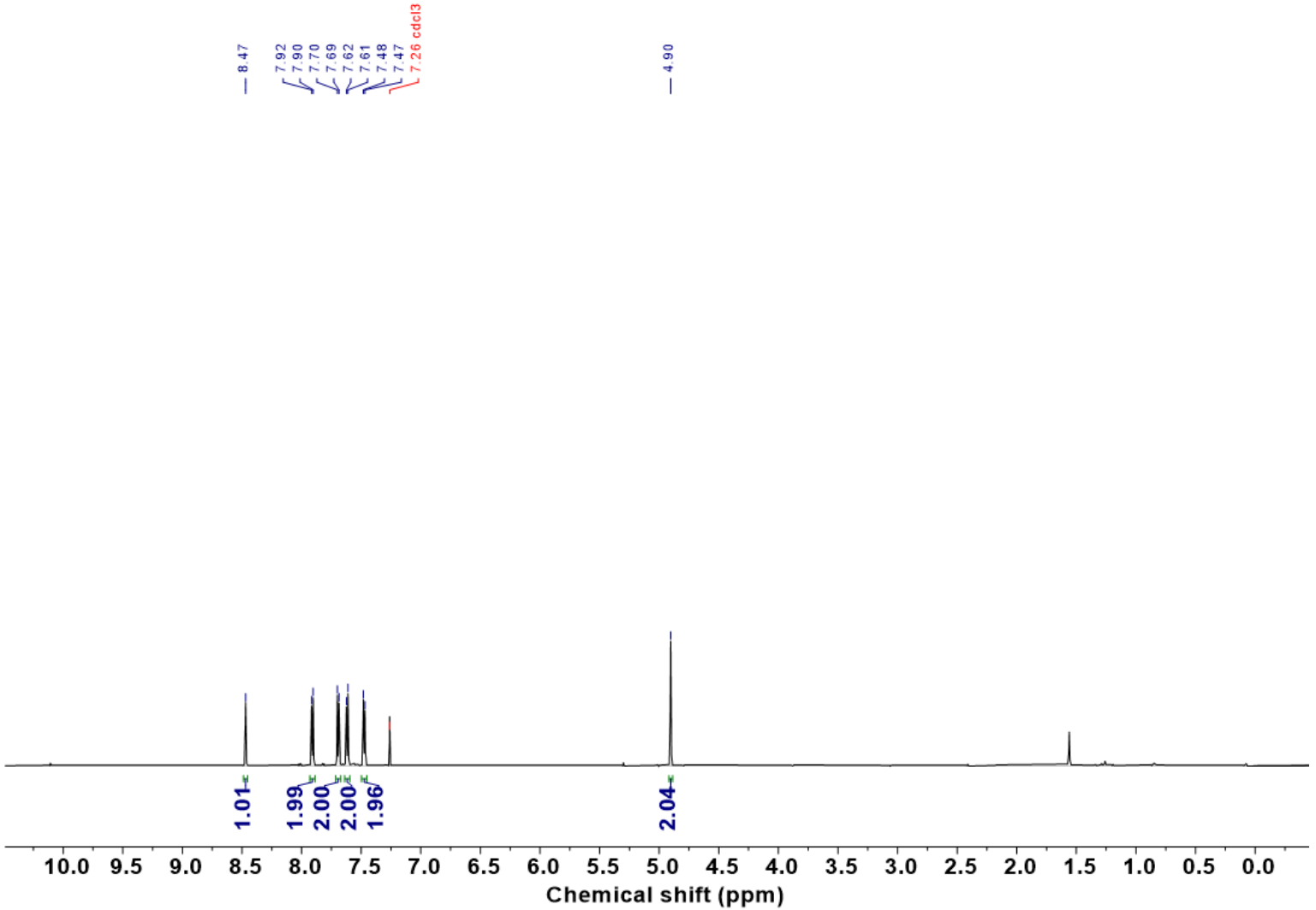

Supplementary Fig. 23 | ^{1}H NMR (600 MHz, $CDCl_3$) spectrum of 6b.

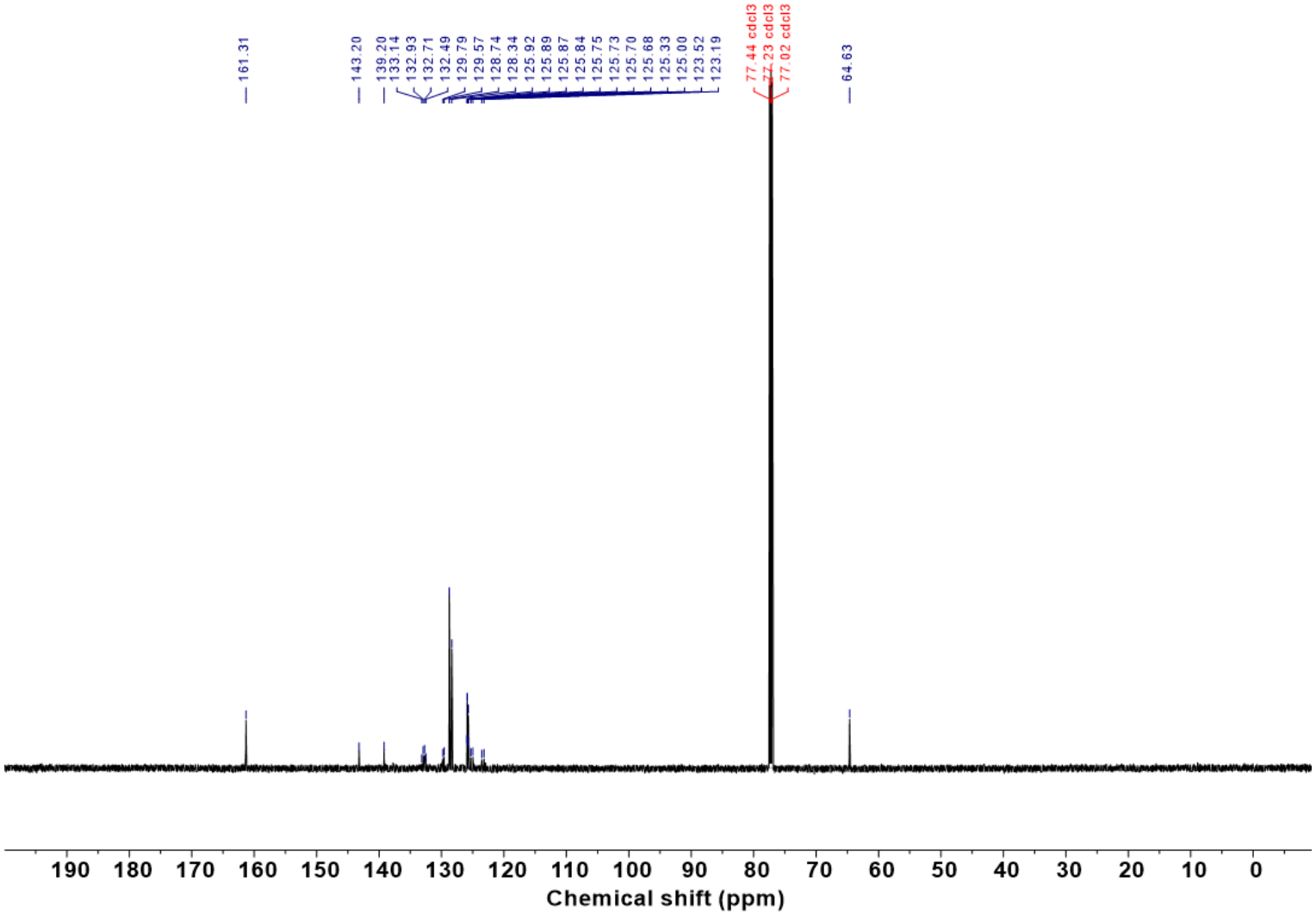

Supplementary Fig. 24 | $^{13}C\{^{1}H\}$ NMR (150 MHz, $CDCl_3$) spectrum of 6b.

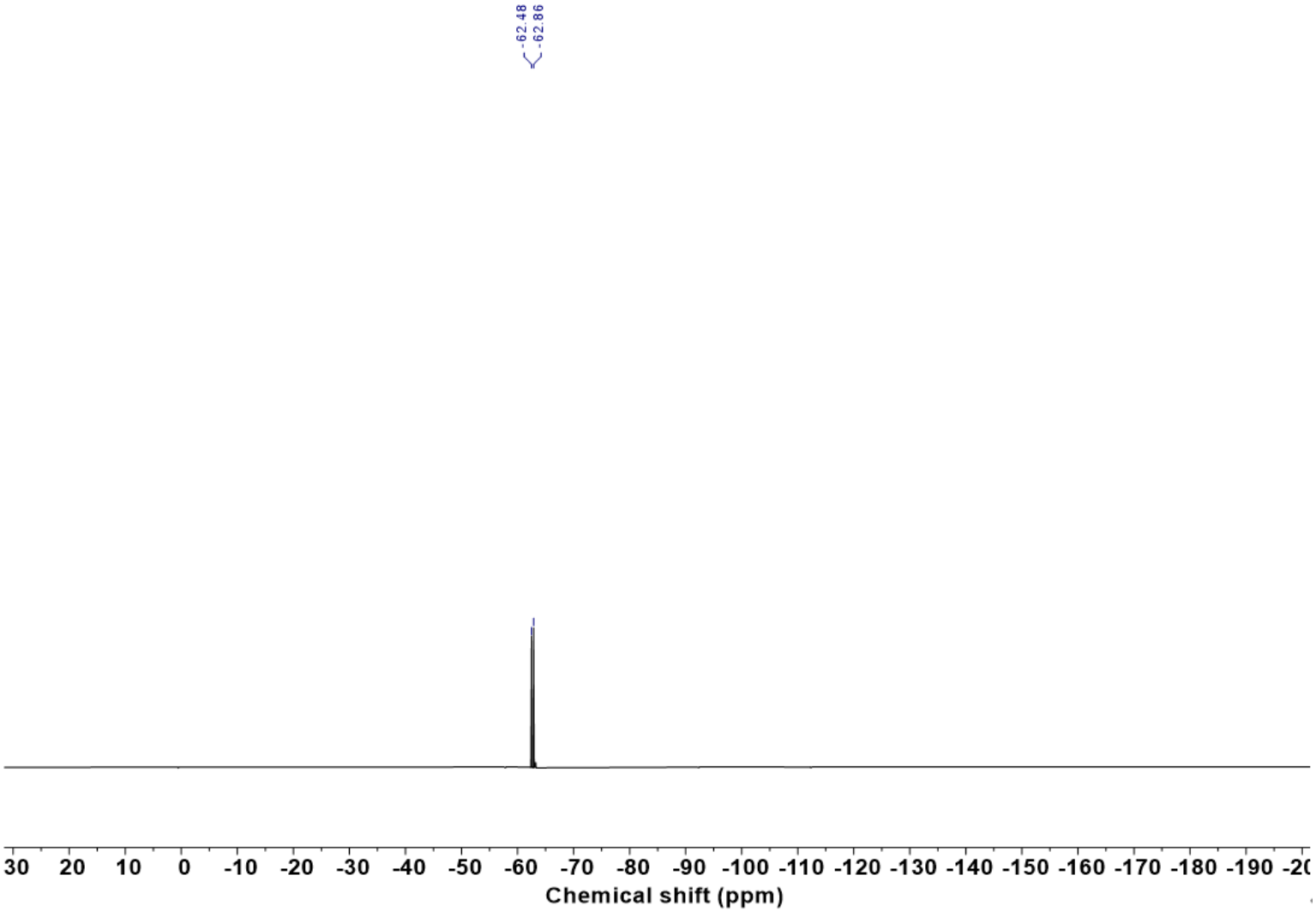

Supplementary Fig. 25 | ^{19}F NMR (564 MHz, $CDCl_3$) spectrum of 6b.

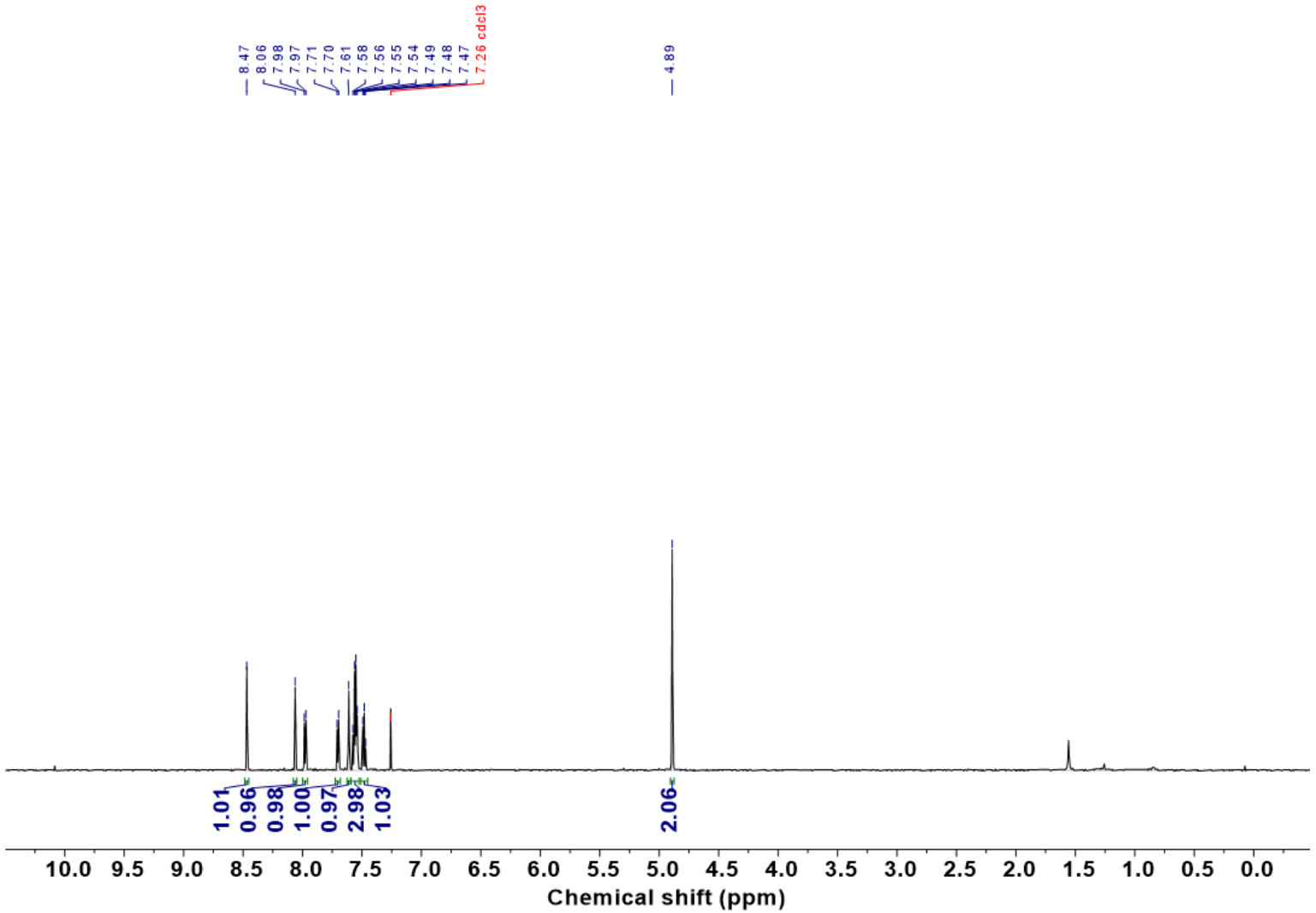

Supplementary Fig. 26 | ^{1}H NMR (600 MHz, $CDCl_3$) spectrum of 7b.

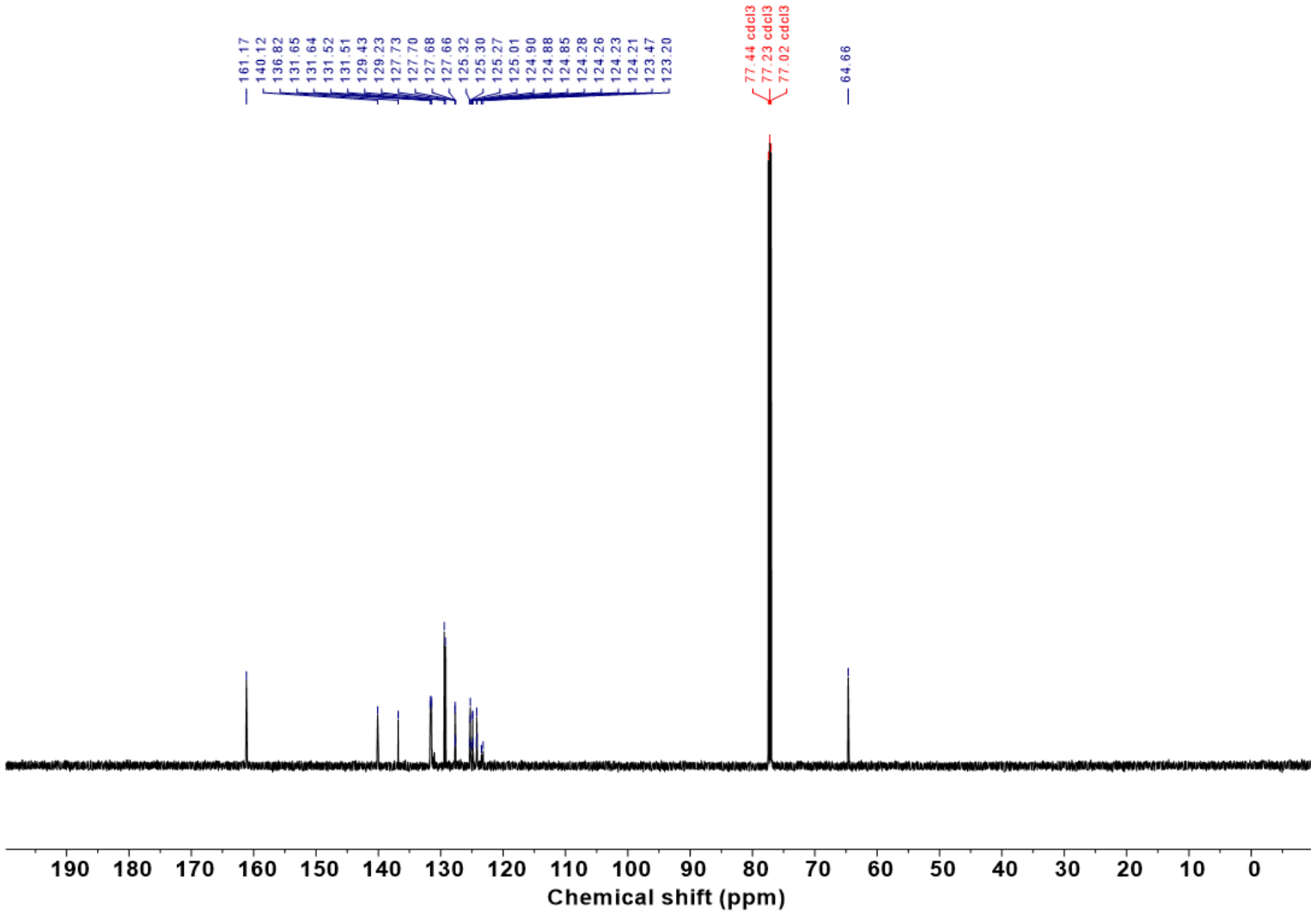

Supplementary Fig. 27 | $^{13}C\{^{1}H\}$ NMR (150 MHz, $CDCl_3$) spectrum of 7b.

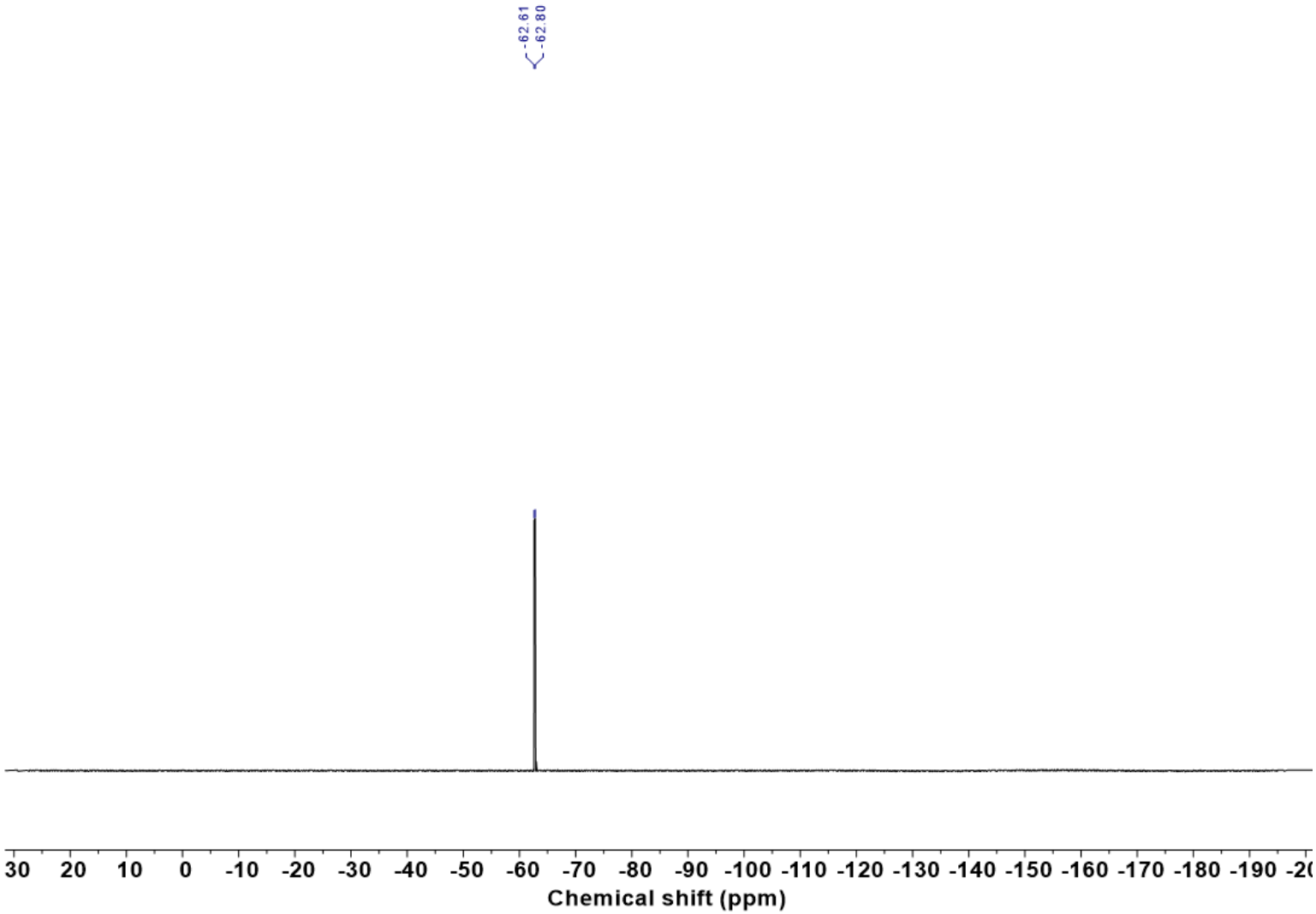

Supplementary Fig. 28 | ^{19}F NMR (564 MHz, $CDCl_3$) spectrum of 7b.

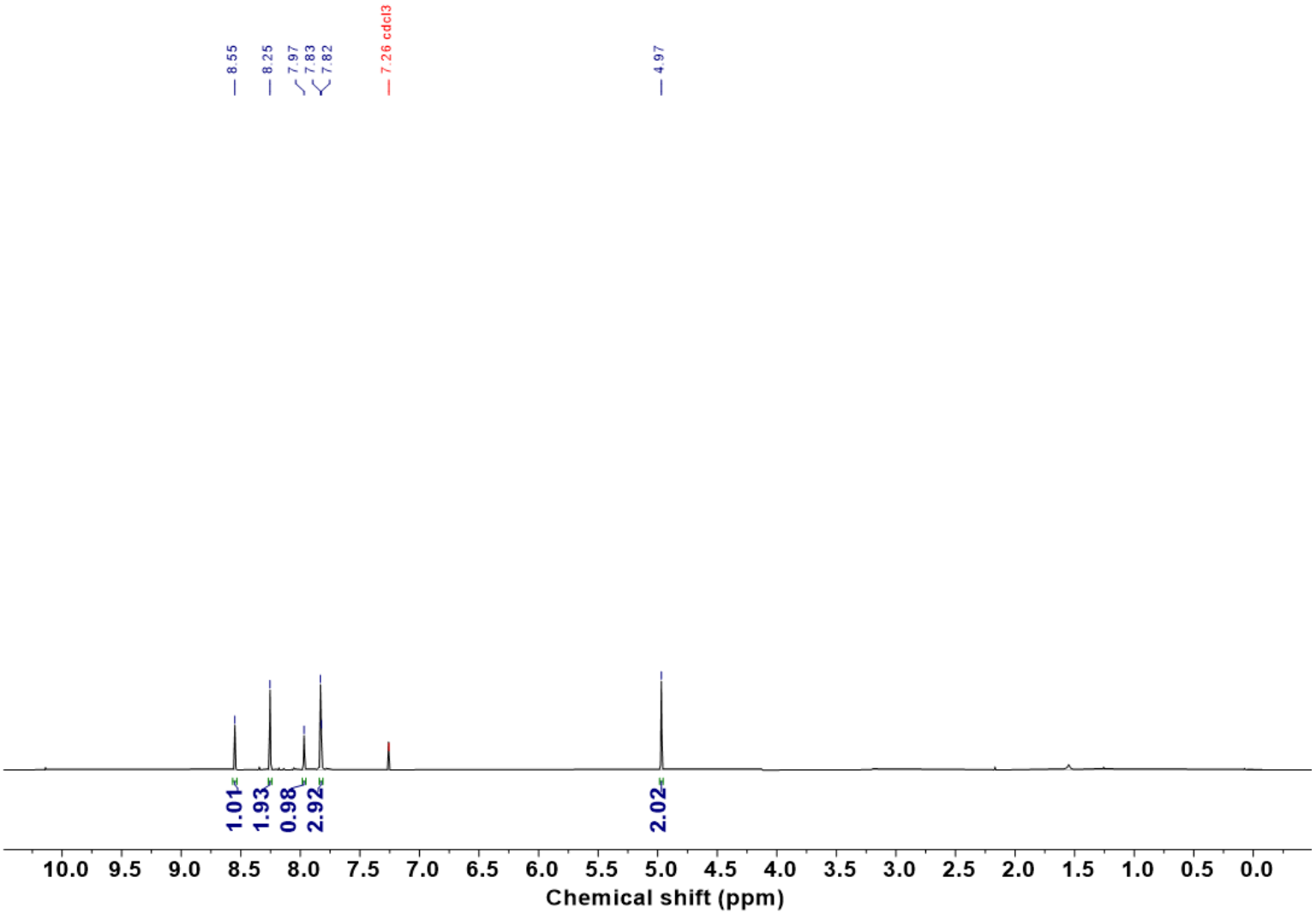

Supplementary Fig. 29 | ^{1}H NMR (600 MHz, $CDCl_3$) spectrum of 8b.

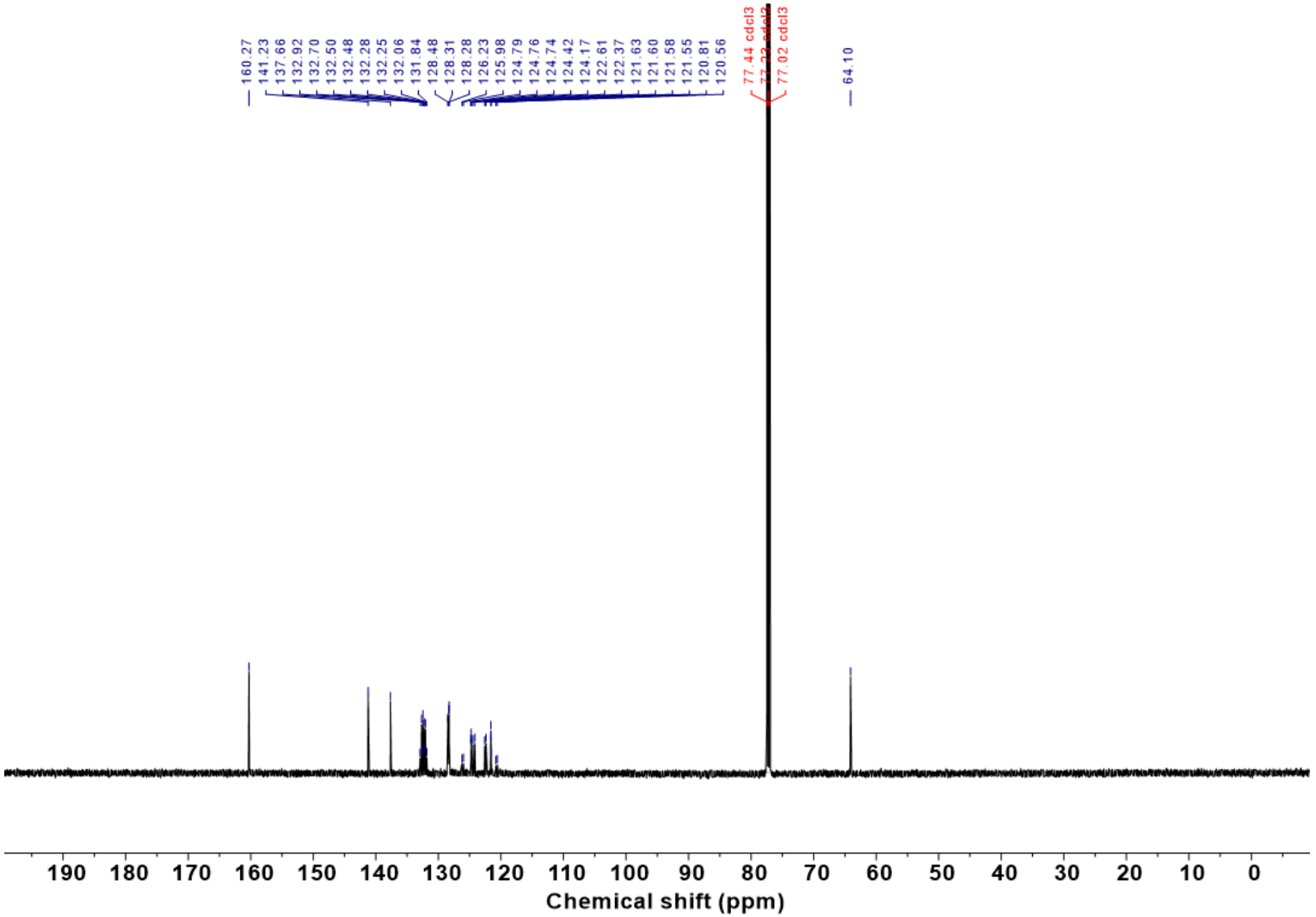

Supplementary Fig. 30 | $^{13}C\{^{1}H\}$ NMR (150 MHz, $CDCl_3$) spectrum of 8b.

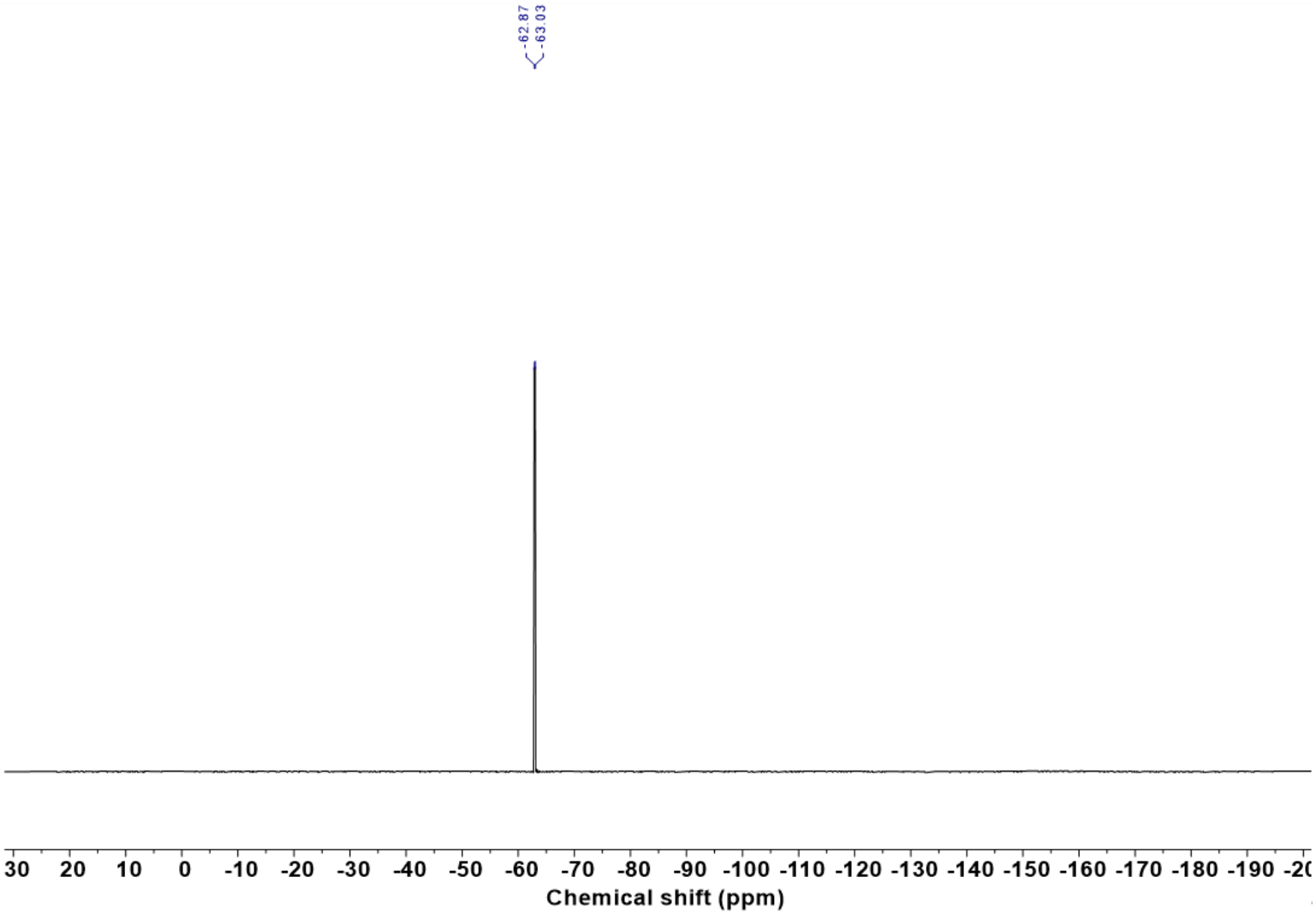

Supplementary Fig. 31 | ^{19}F NMR (564 MHz, $CDCl_3$) spectrum of 8b.

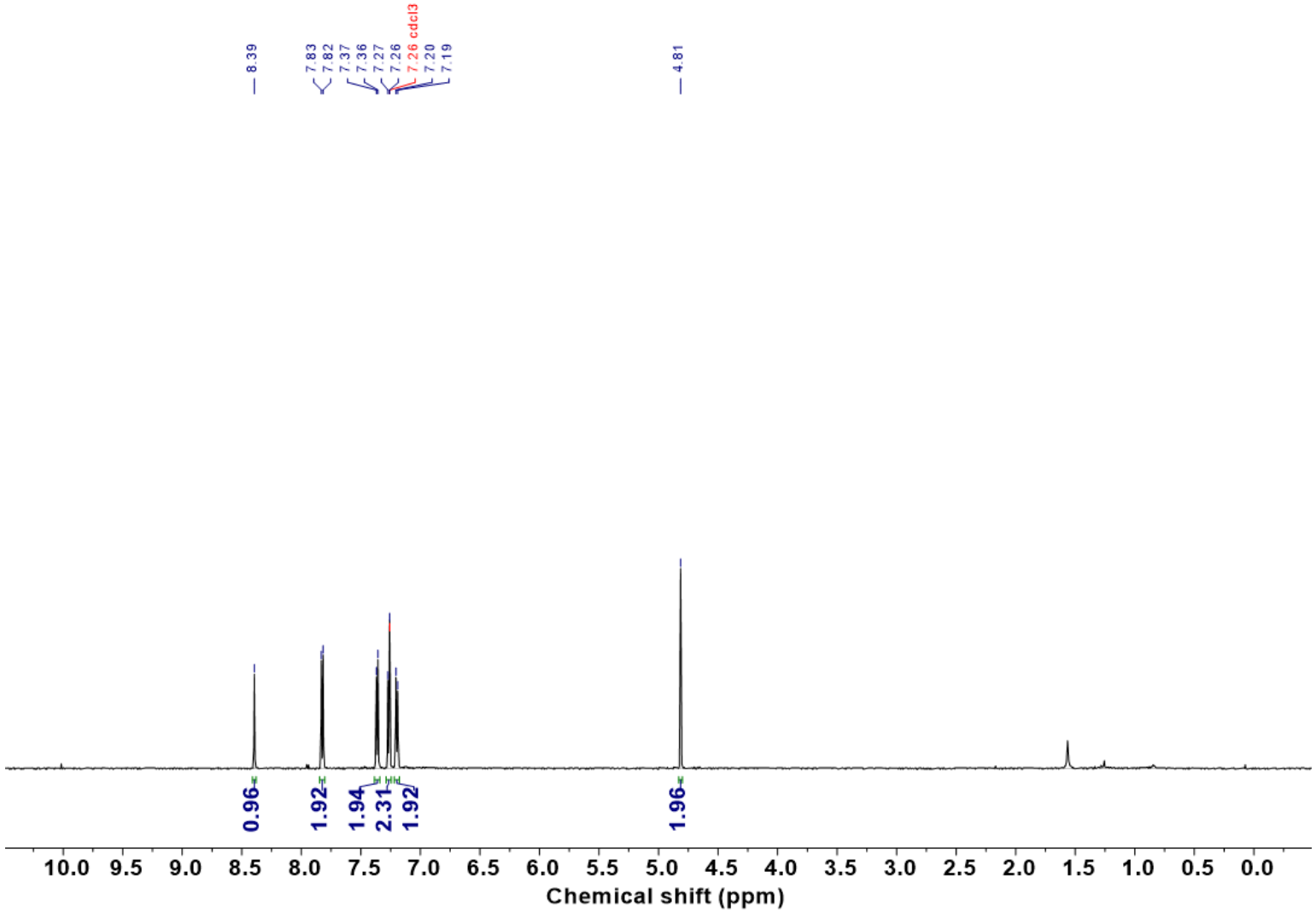

Supplementary Fig. 32 | ^{1}H NMR (600 MHz, $CDCl_3$) spectrum of 9b.

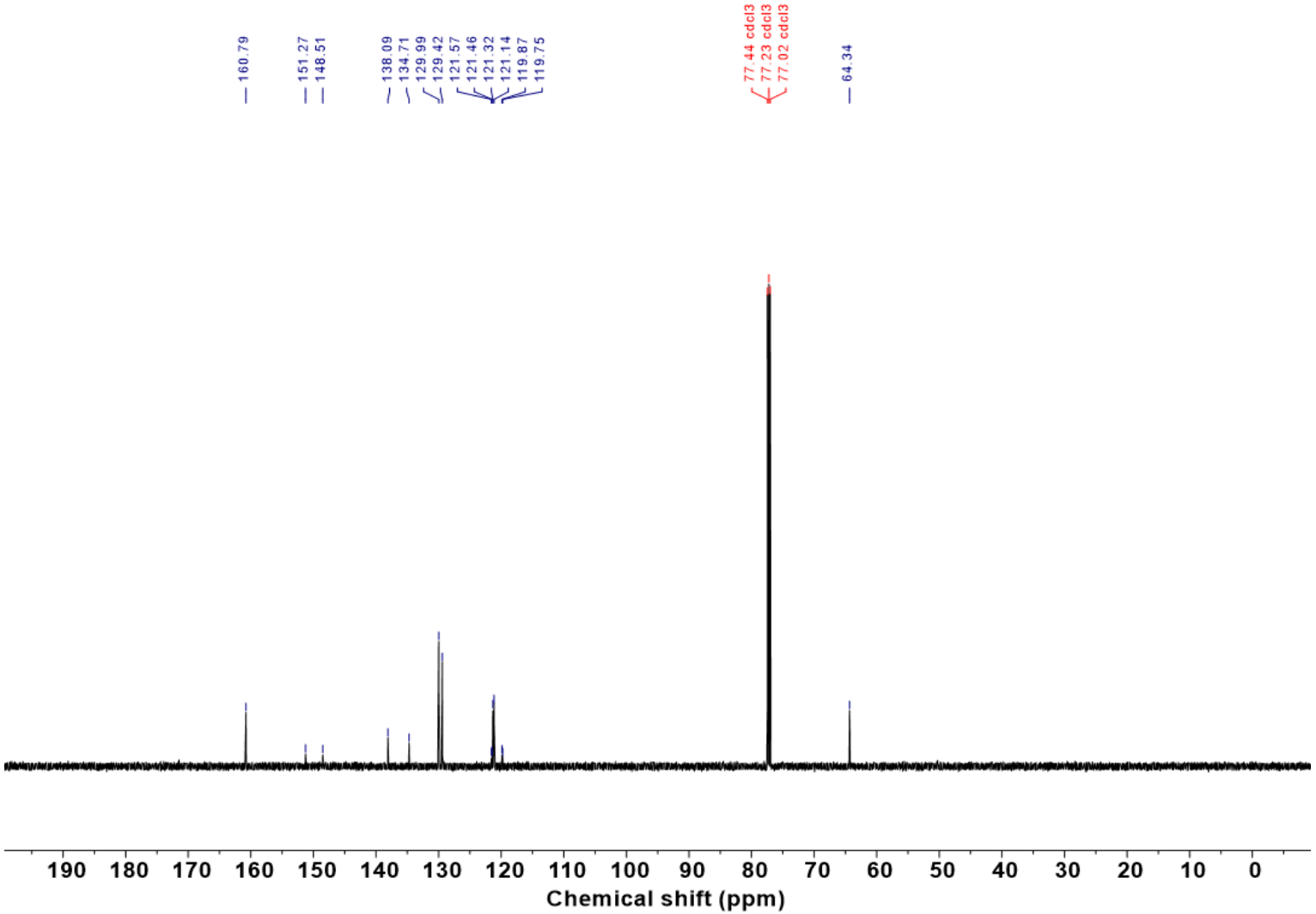

Supplementary Fig. 33 | $^{13}C\{^{1}H\}$ NMR (150 MHz, $CDCl_3$) spectrum of 9b.

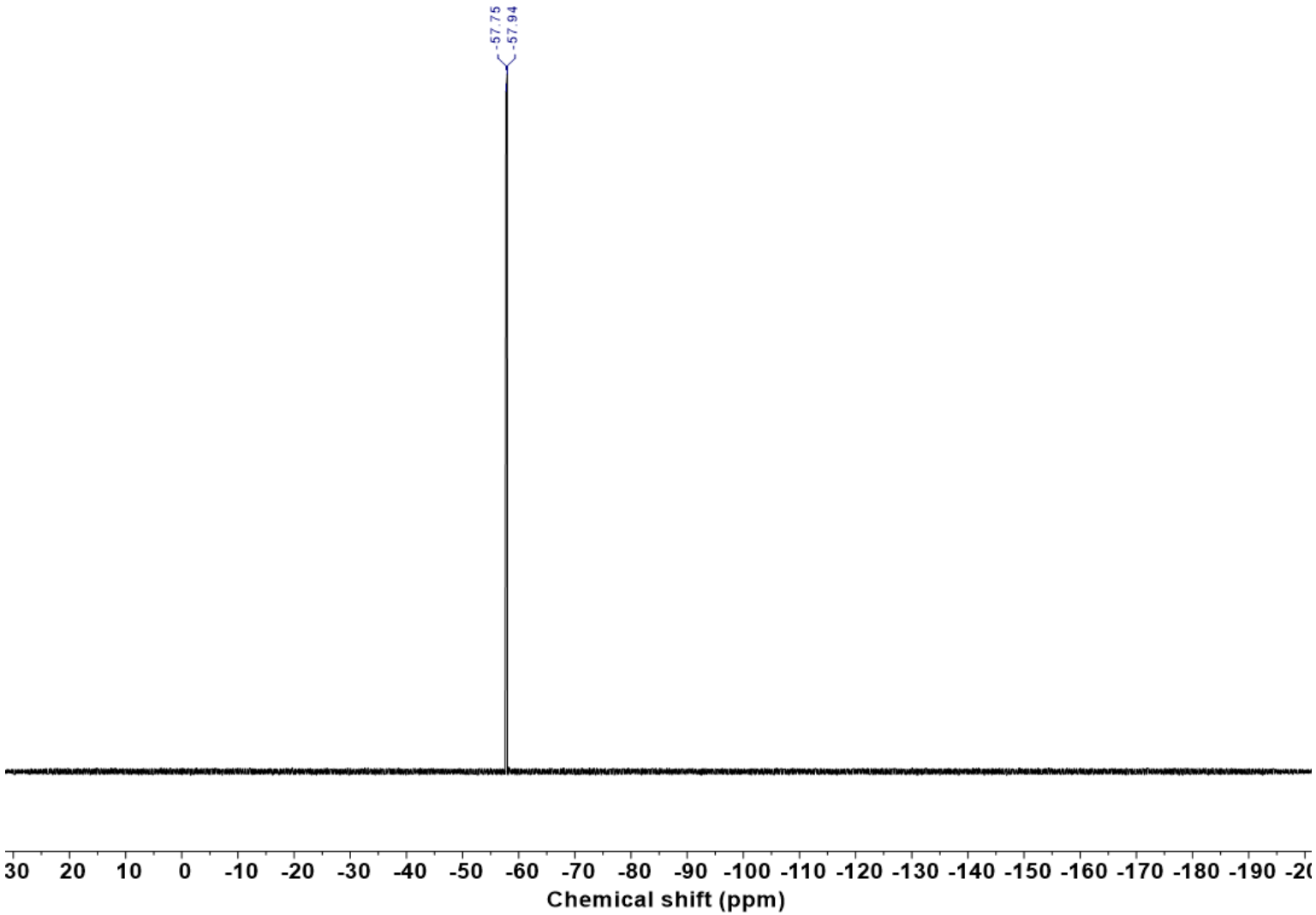

Supplementary Fig. 34 | ^{19}F NMR (564 MHz, $CDCl_3$) spectrum of 9b.

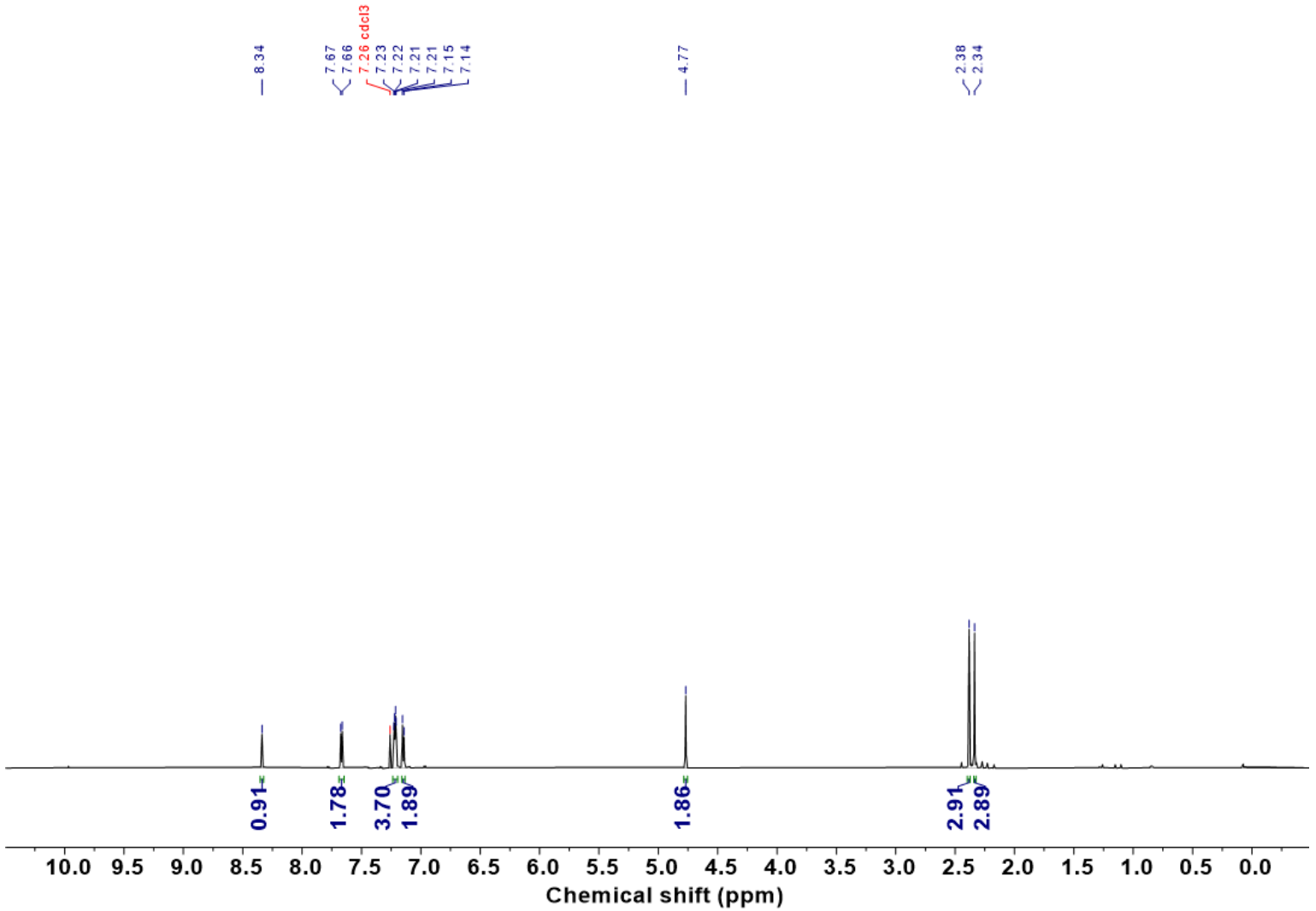

Supplementary Fig. 35 | ^{1}H NMR (600 MHz, $CDCl_3$) spectrum of 10b.

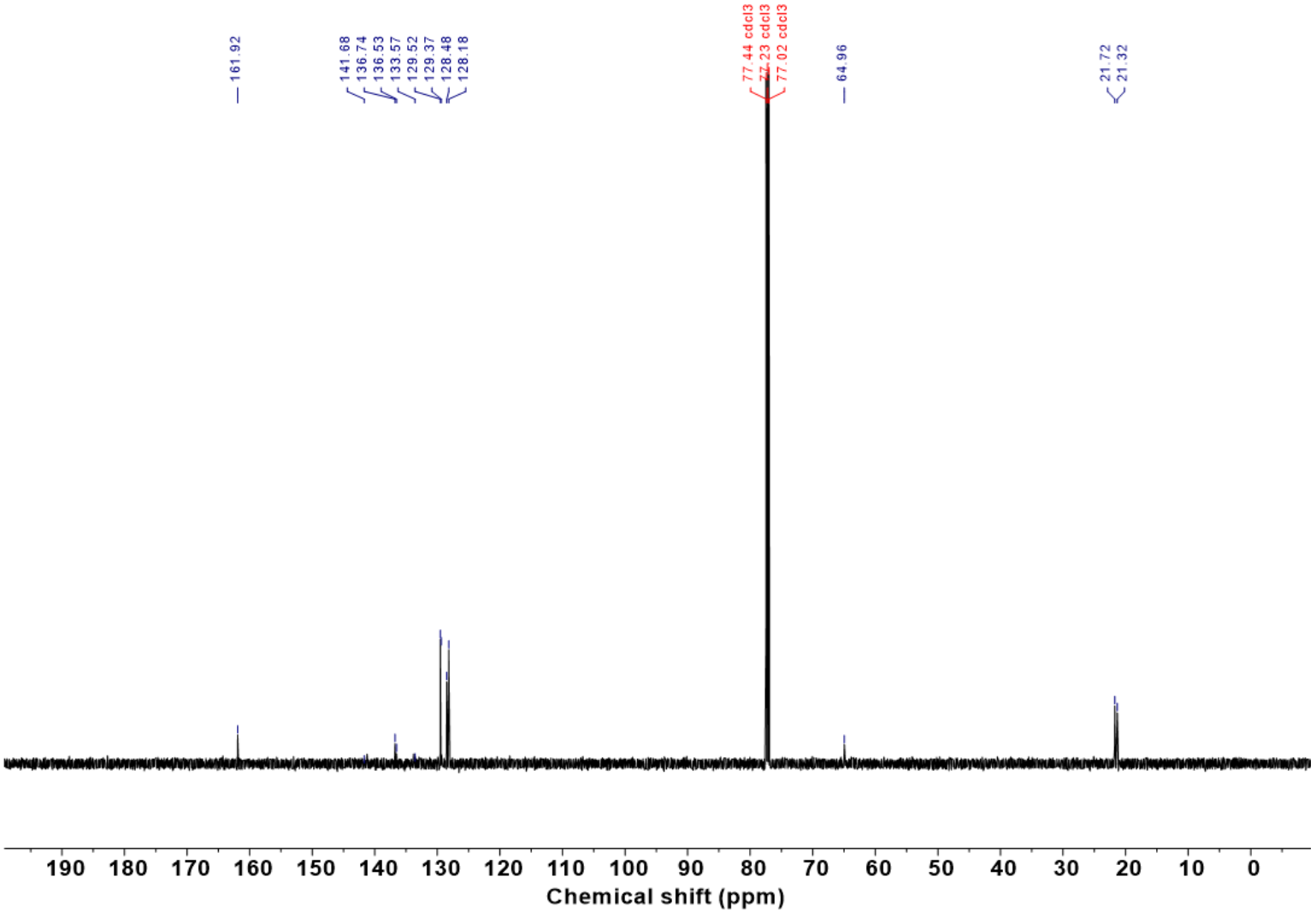

Supplementary Fig. 36 | $^{13}C\{^{1}H\}$ NMR (150 MHz, $CDCl_3$) spectrum of 10b.

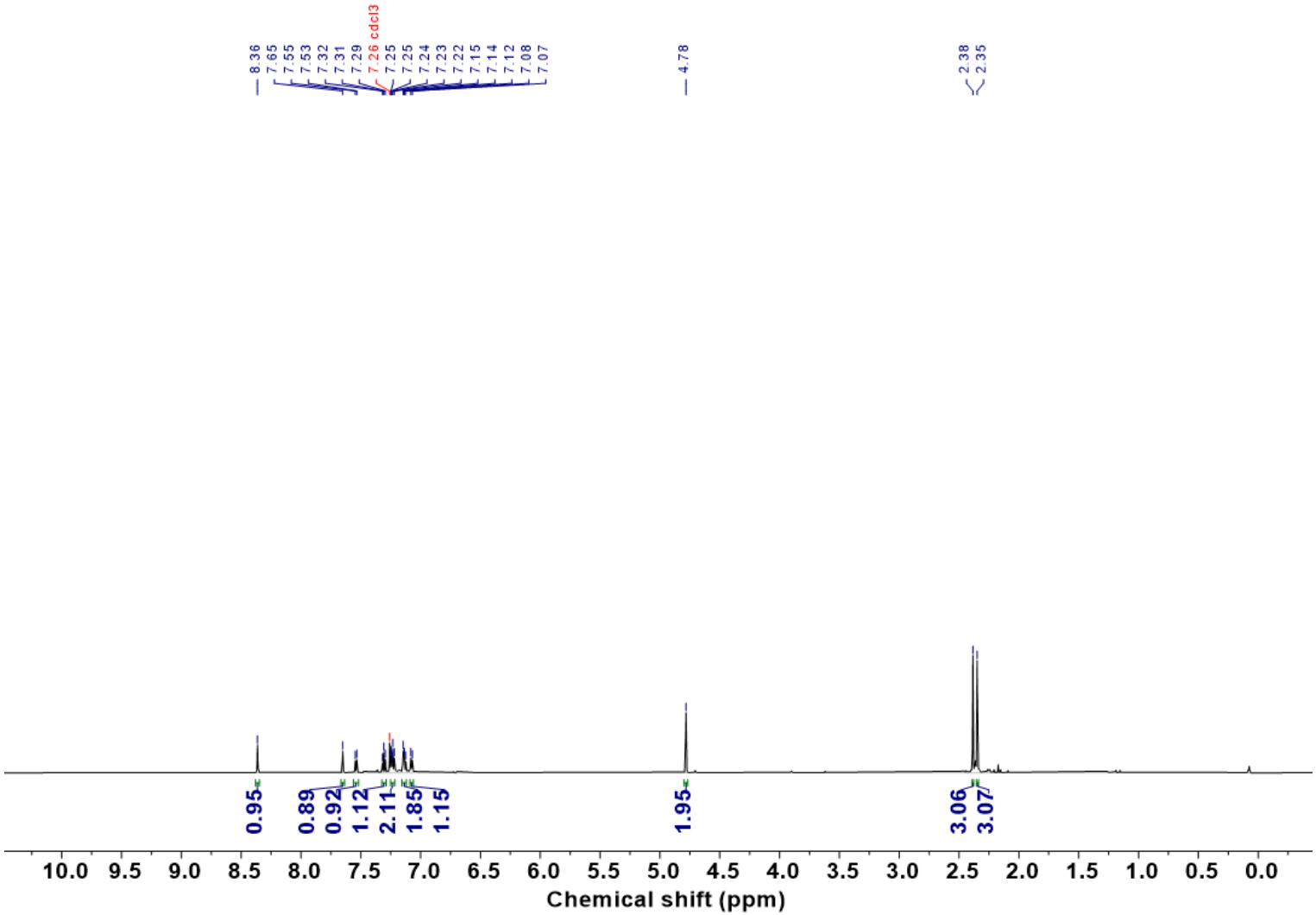

Supplementary Fig. 37 | ^{1}H NMR (600 MHz, $CDCl_3$) spectrum of 11b.

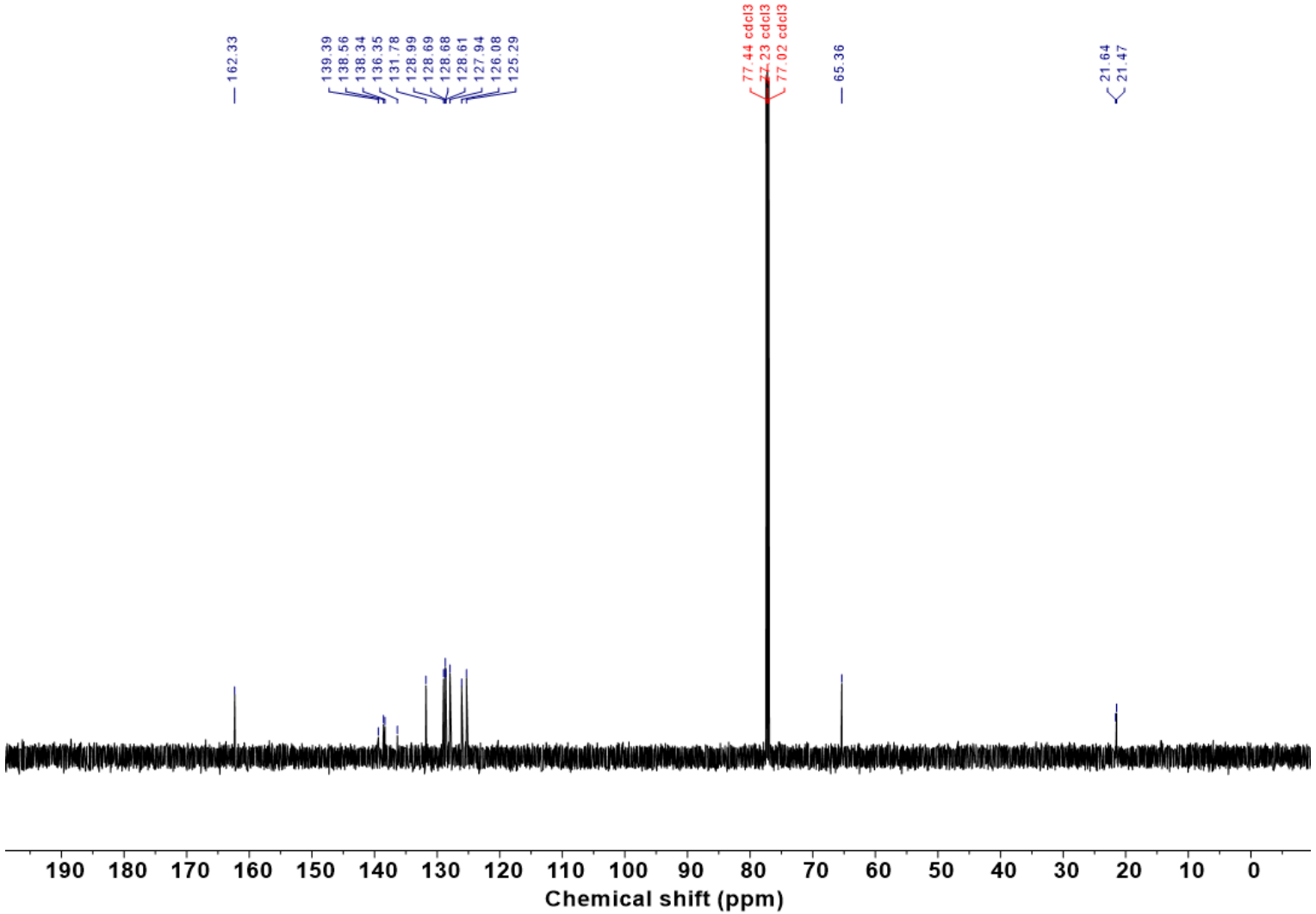

Supplementary Fig. 38 | $^{13}C\{^{1}H\}$ NMR (150 MHz, $CDCl_3$) spectrum of 11b.

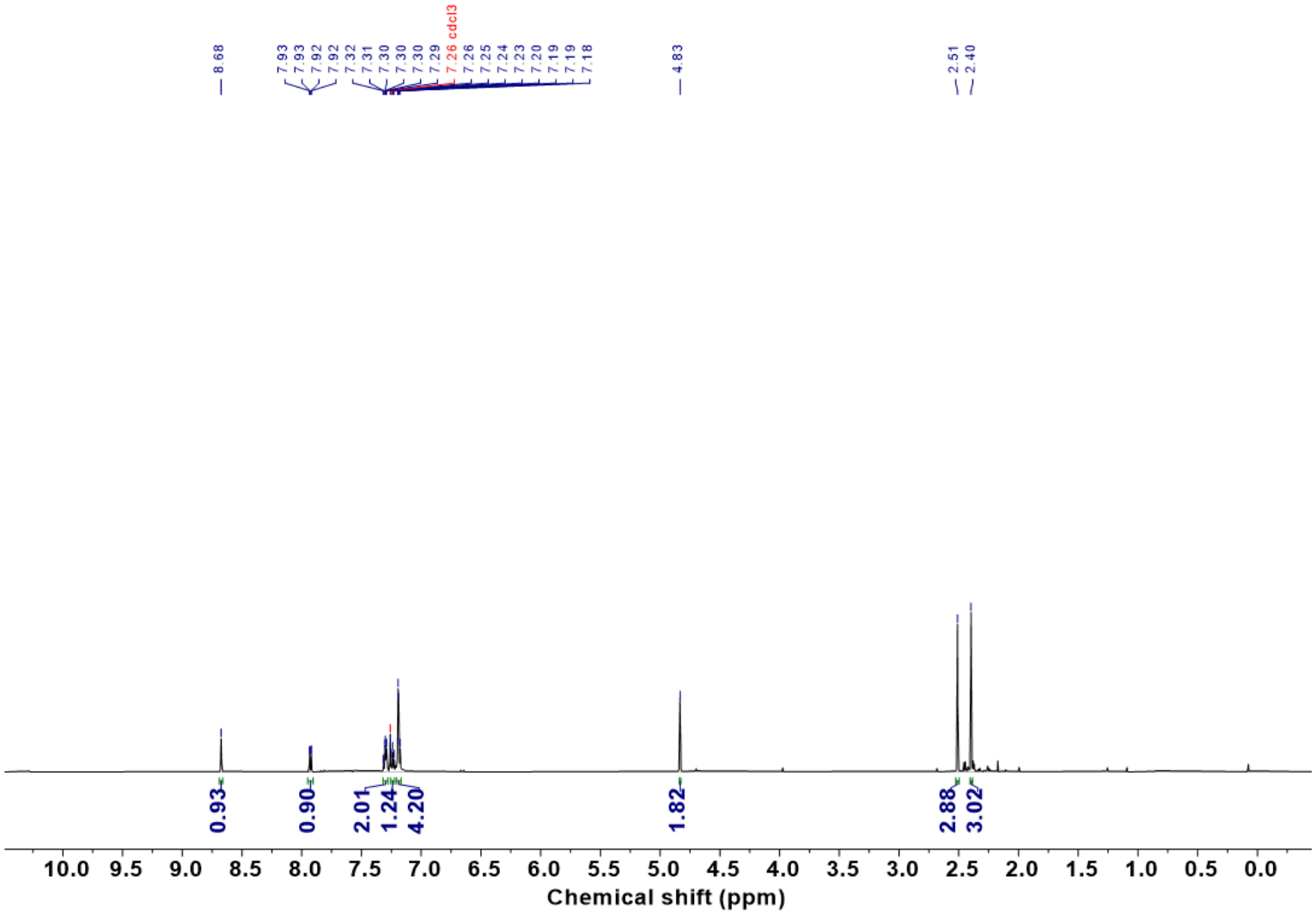

Supplementary Fig. 39 | ^{1}H NMR (600 MHz, $CDCl_3$) spectrum of 12b.

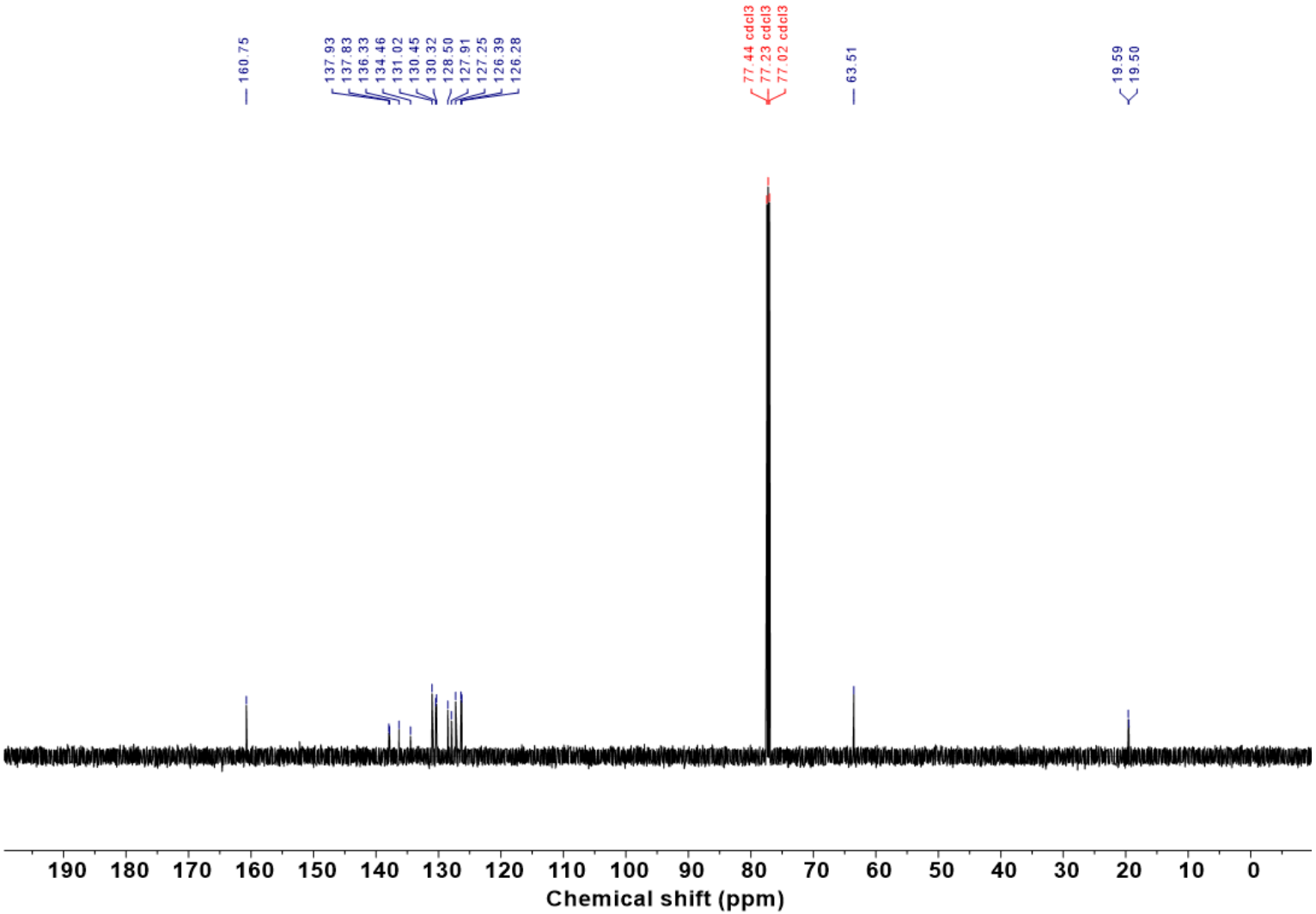

Supplementary Fig. 40 | $^{13}C\{^{1}H\}$ NMR (150 MHz, $CDCl_3$) spectrum of 12b.

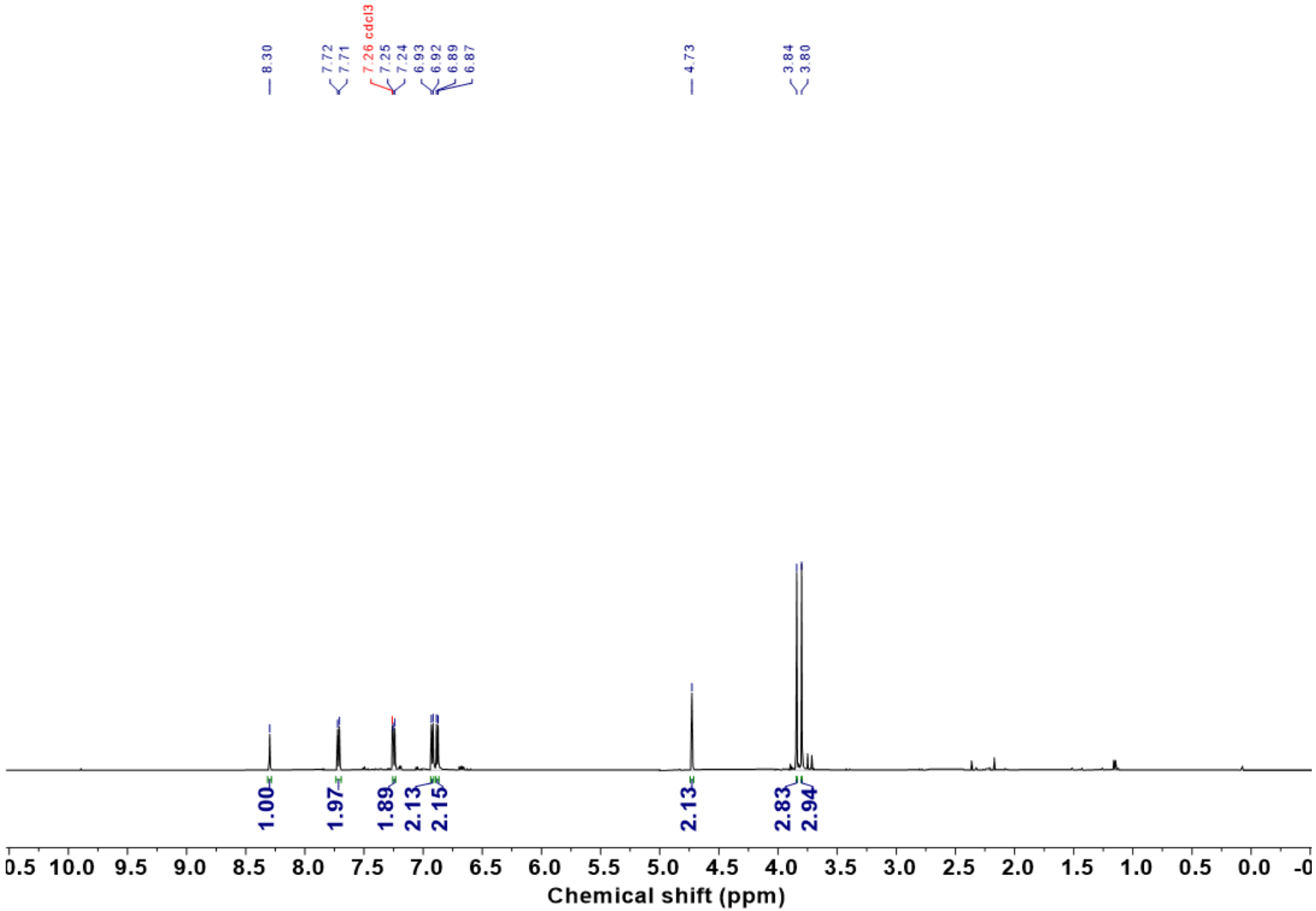

Supplementary Fig. 41 | ^{1}H NMR (600 MHz, $CDCl_3$) spectrum of 13b.

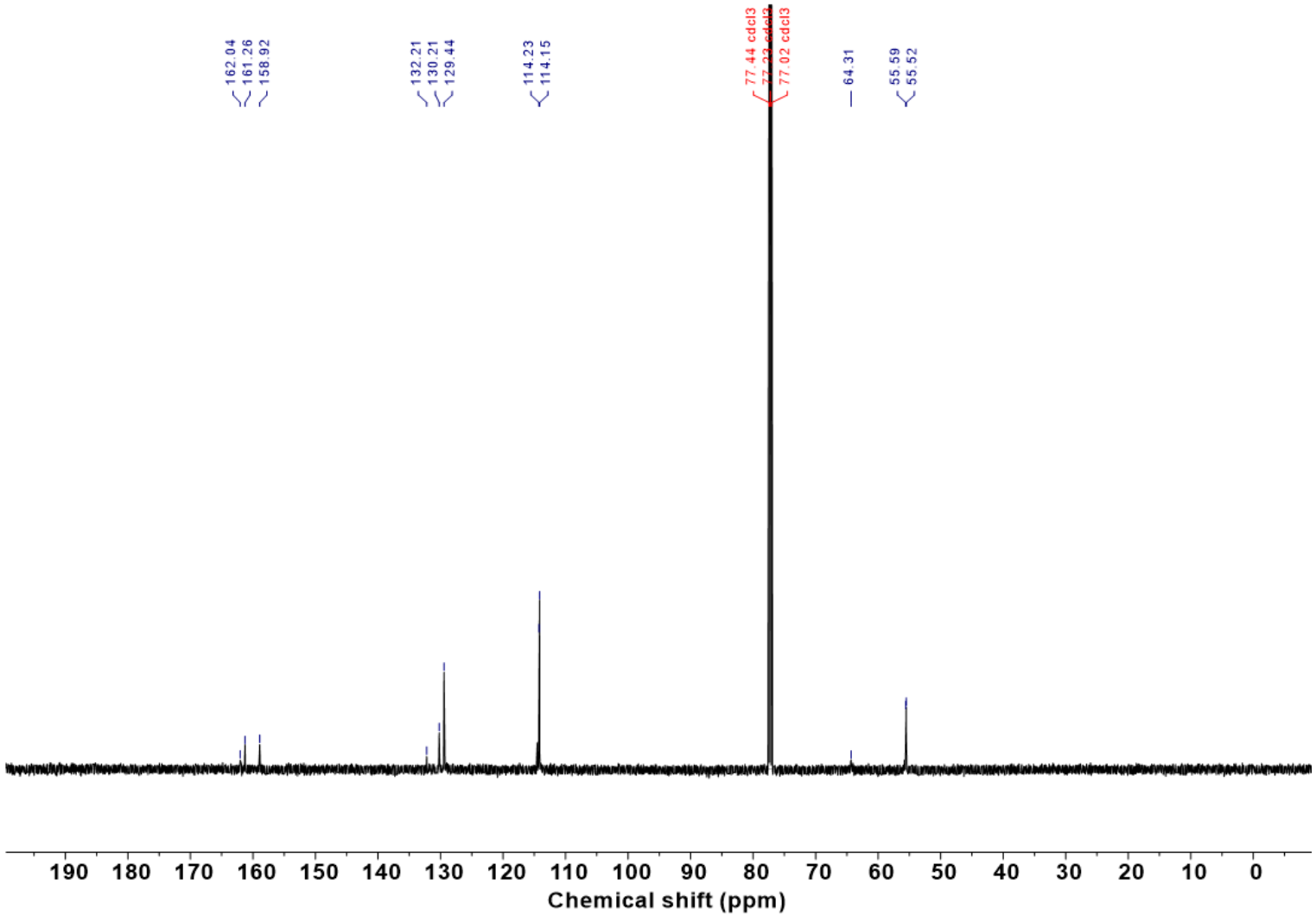

Supplementary Fig. 42 | $^{13}C\{^{1}H\}$ NMR (150 MHz, $CDCl_3$) spectrum of 13b.

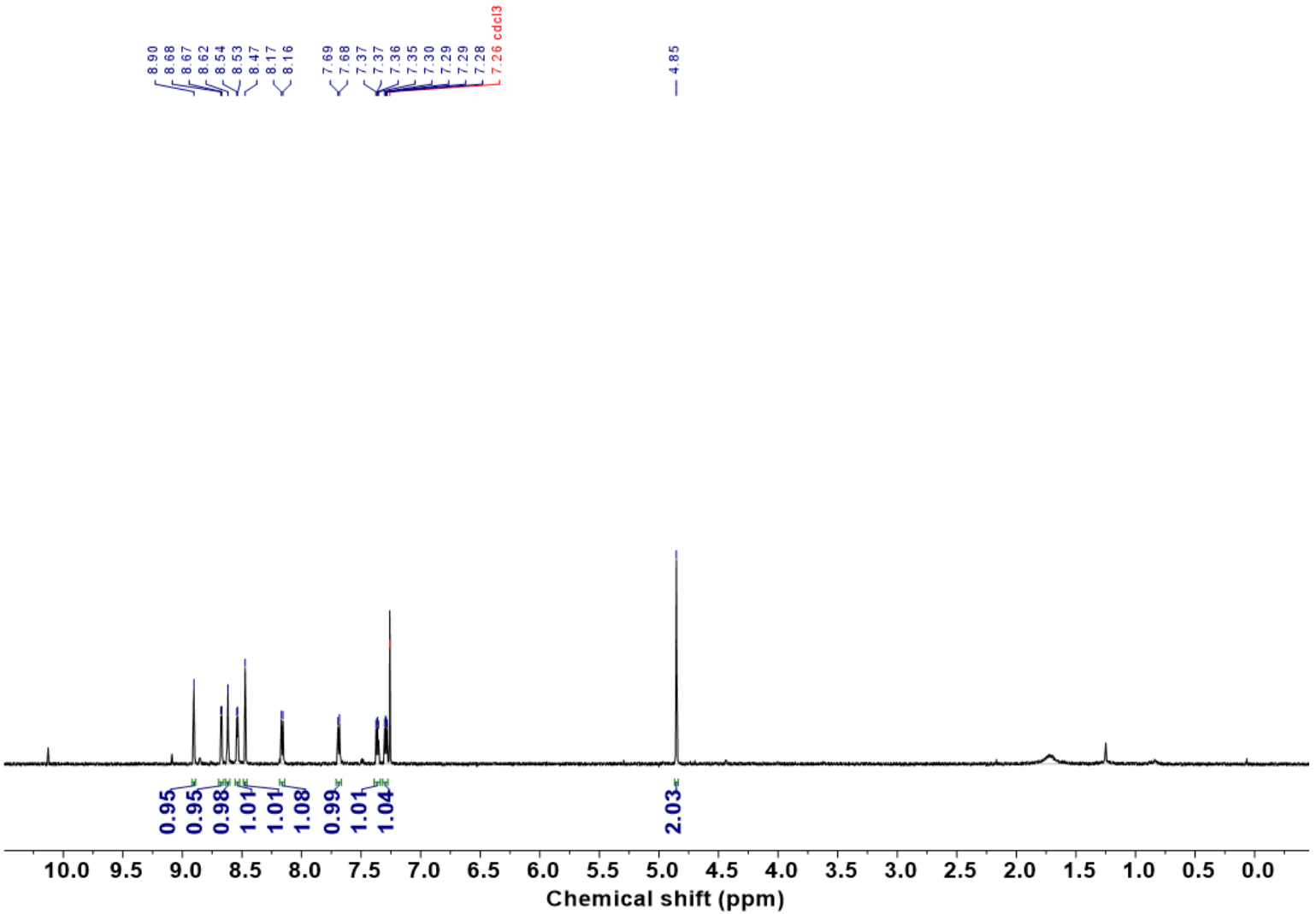

Supplementary Fig. 43 | ^{1}H NMR (600 MHz, $CDCl_3$) spectrum of 14b.

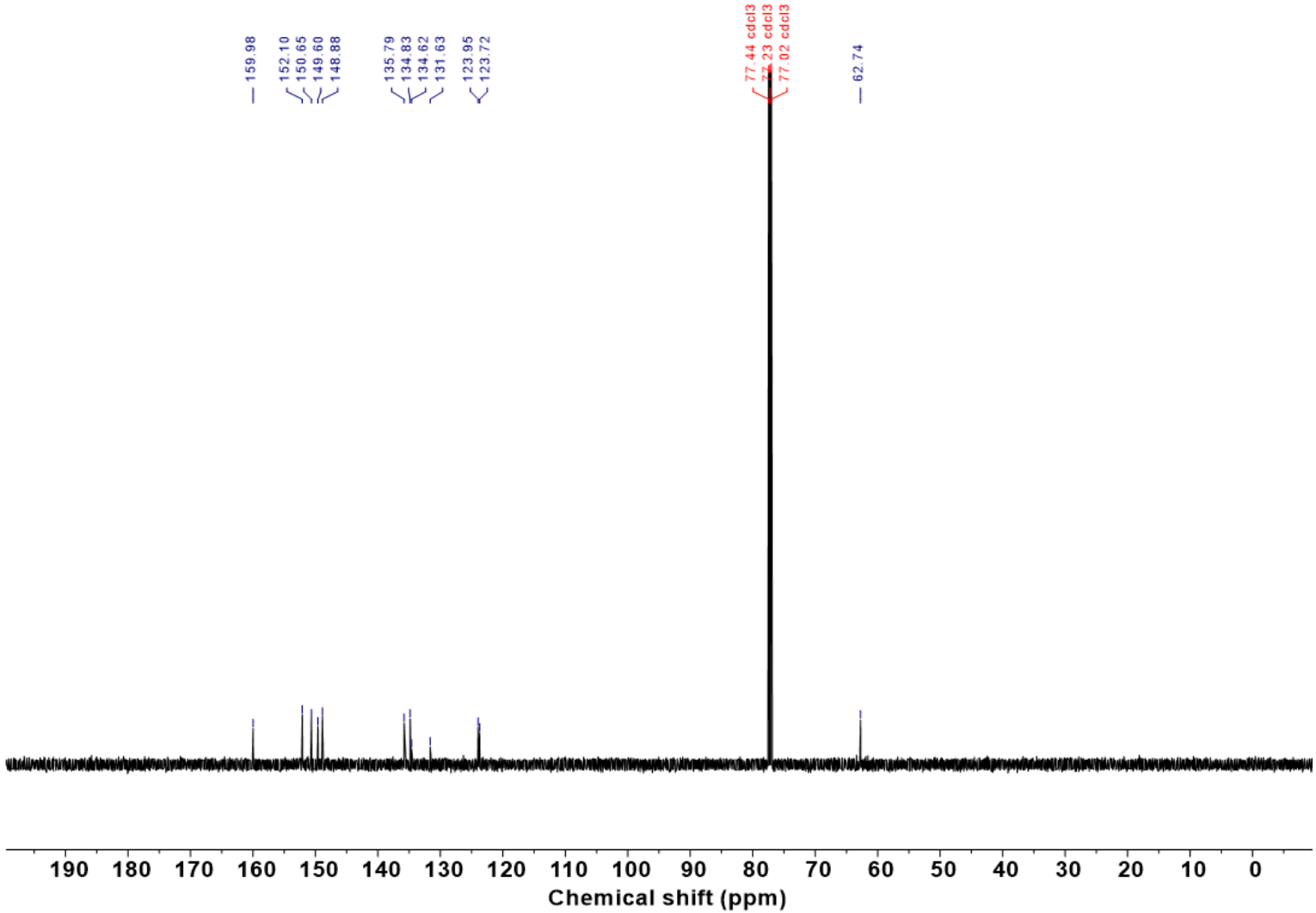

Supplementary Fig. 44 | $^{13}C\{^{1}H\}$ NMR (150 MHz, $CDCl_3$) spectrum of 14b.

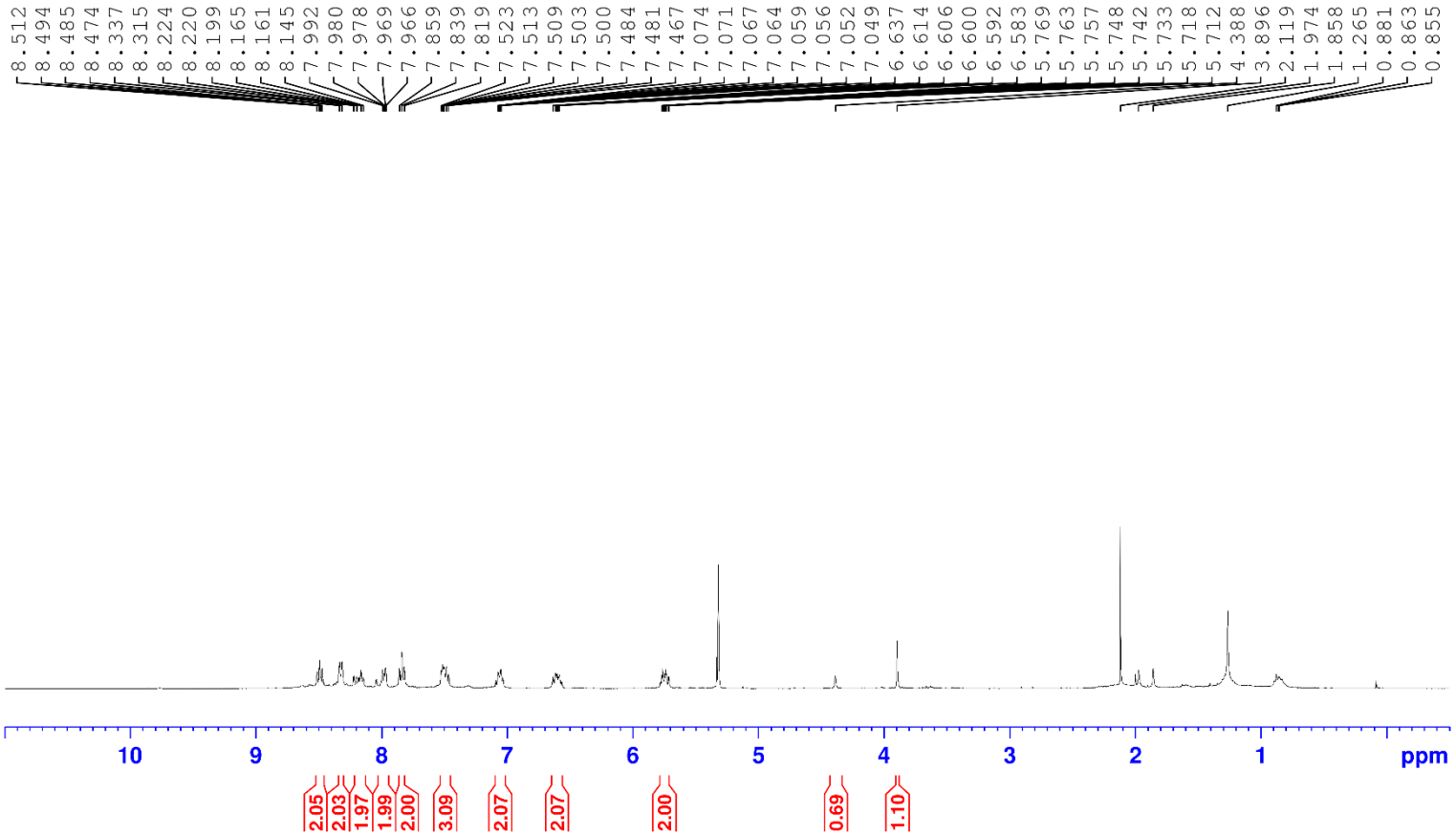

Supplementary Fig. 45 | ^{1}H NMR (400 MHz, CD_2Cl_2) spectrum of 15a.

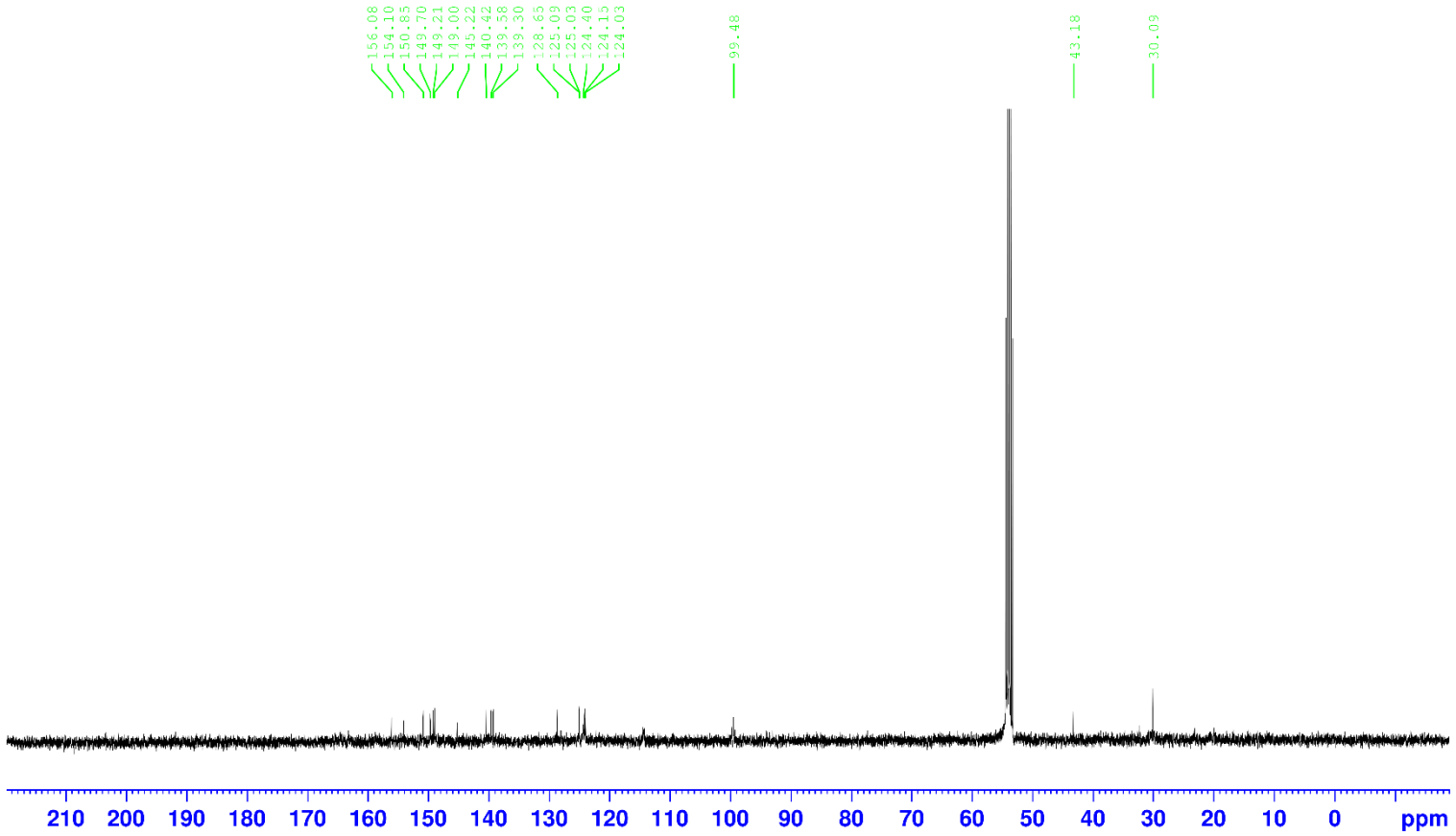

Supplementary Fig. 46 | $^{13}C\{^{1}H\}$ NMR (100 MHz, CD_2Cl_2) spectrum of 15a.

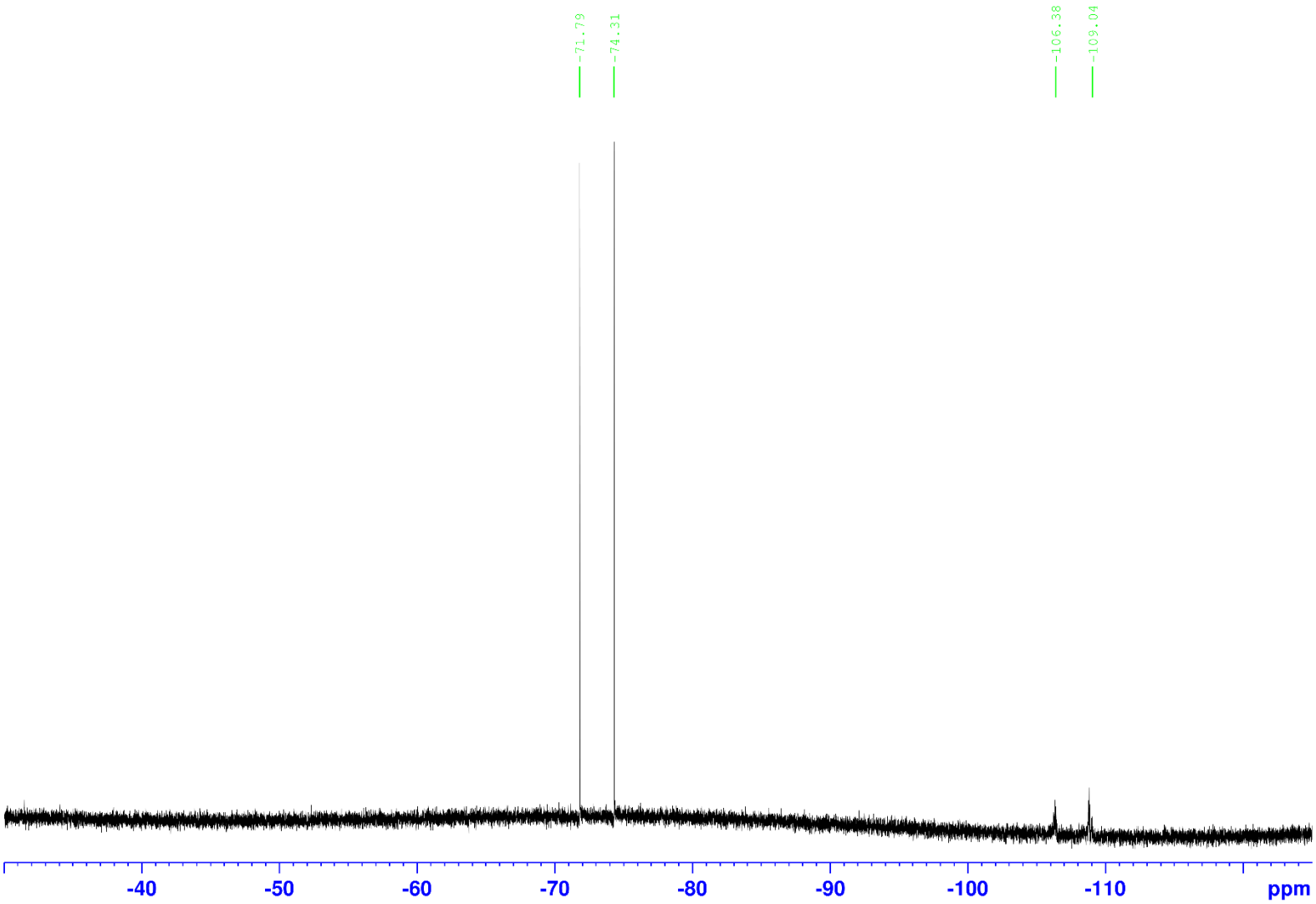

Supplementary Fig. 47 | ^{19}F NMR (376.5 MHz, CD_2Cl_2) spectrum of 15a.

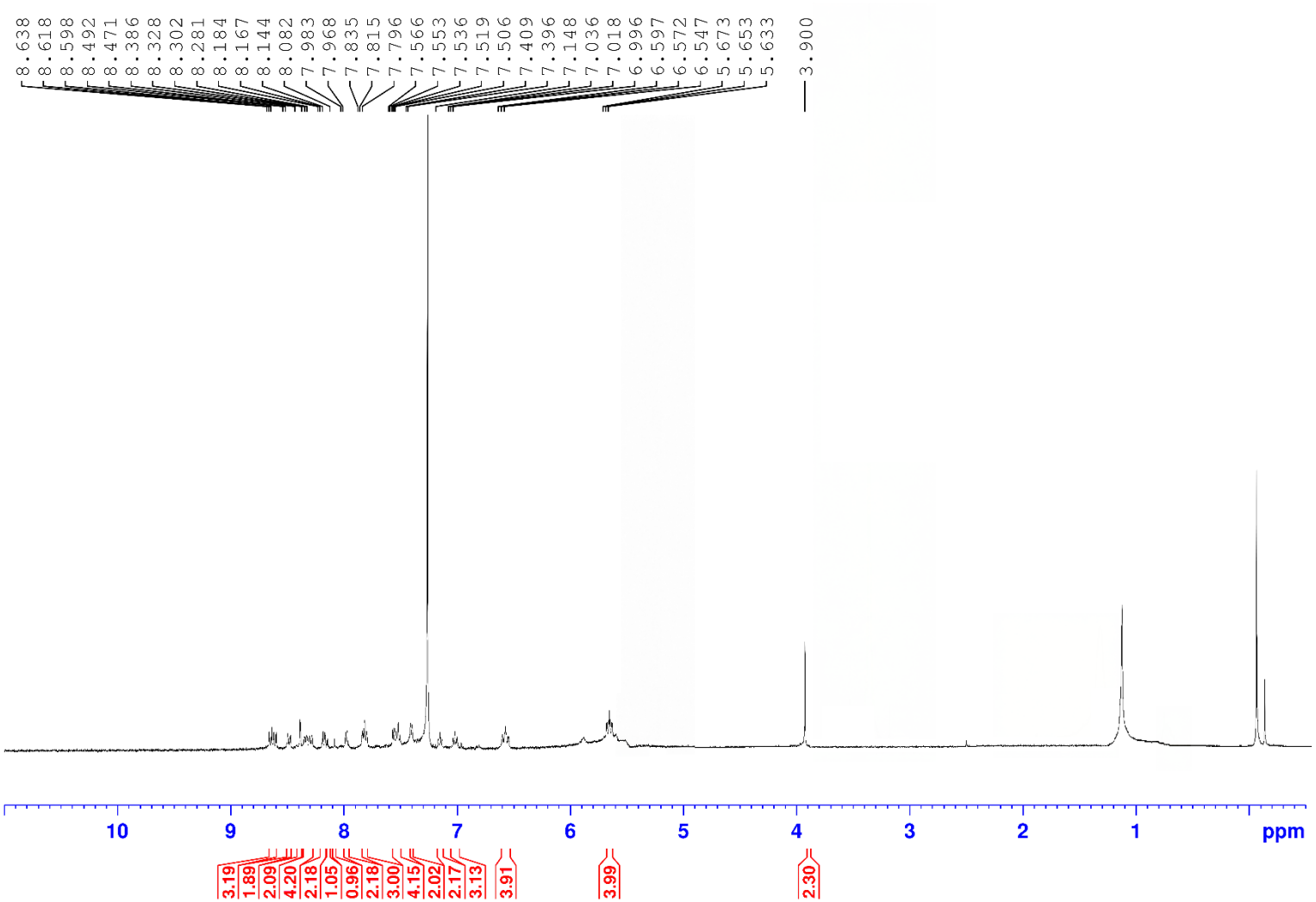

Supplementary Fig. 48 | ^{1}H NMR (400 MHz, $CDCl_3$) spectrum of 15b.

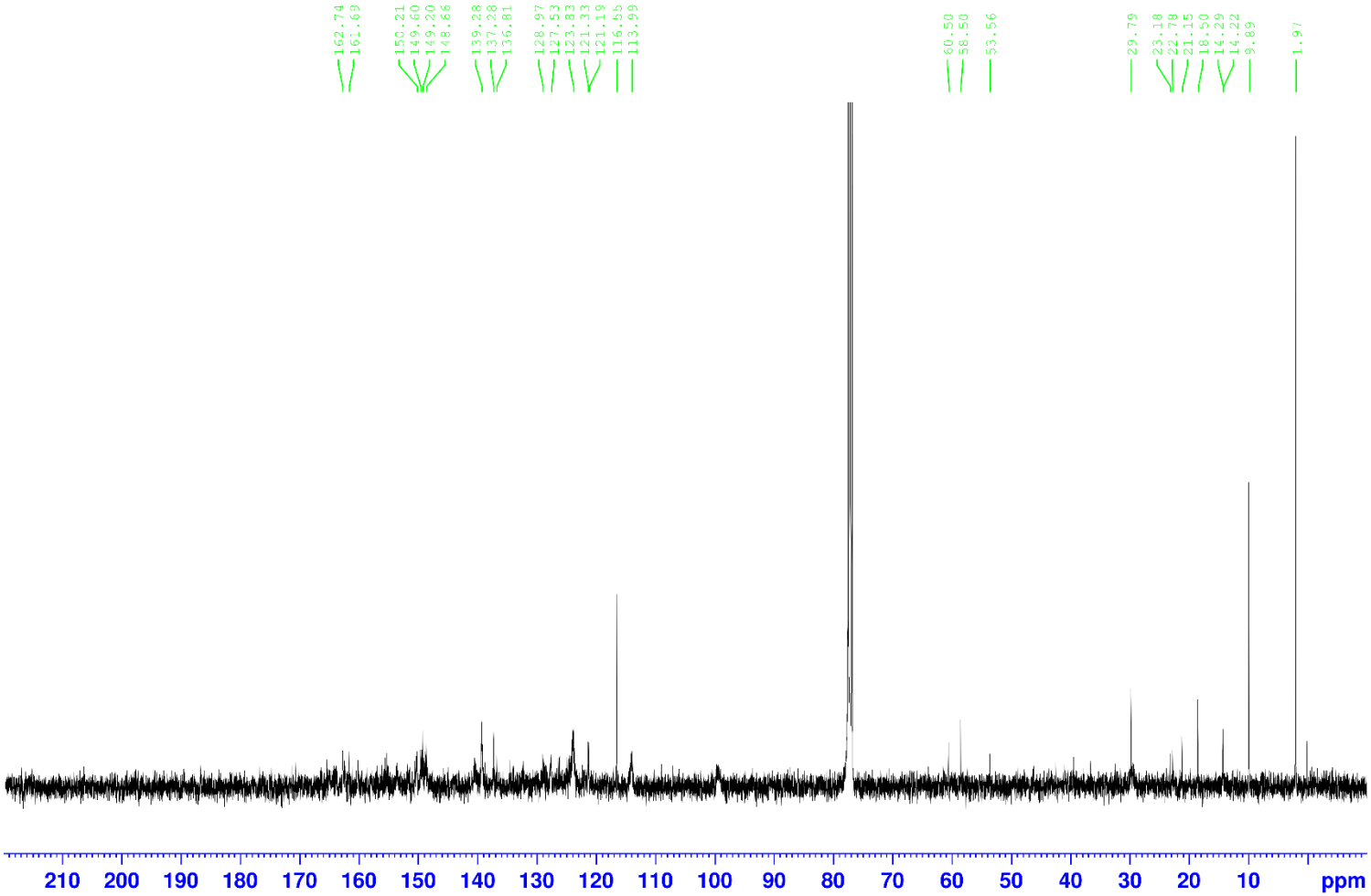

Supplementary Fig. 49 | $^{13}C\{^{1}H\}$ NMR (100 MHz, $CDCl_3$) spectrum of 15b.

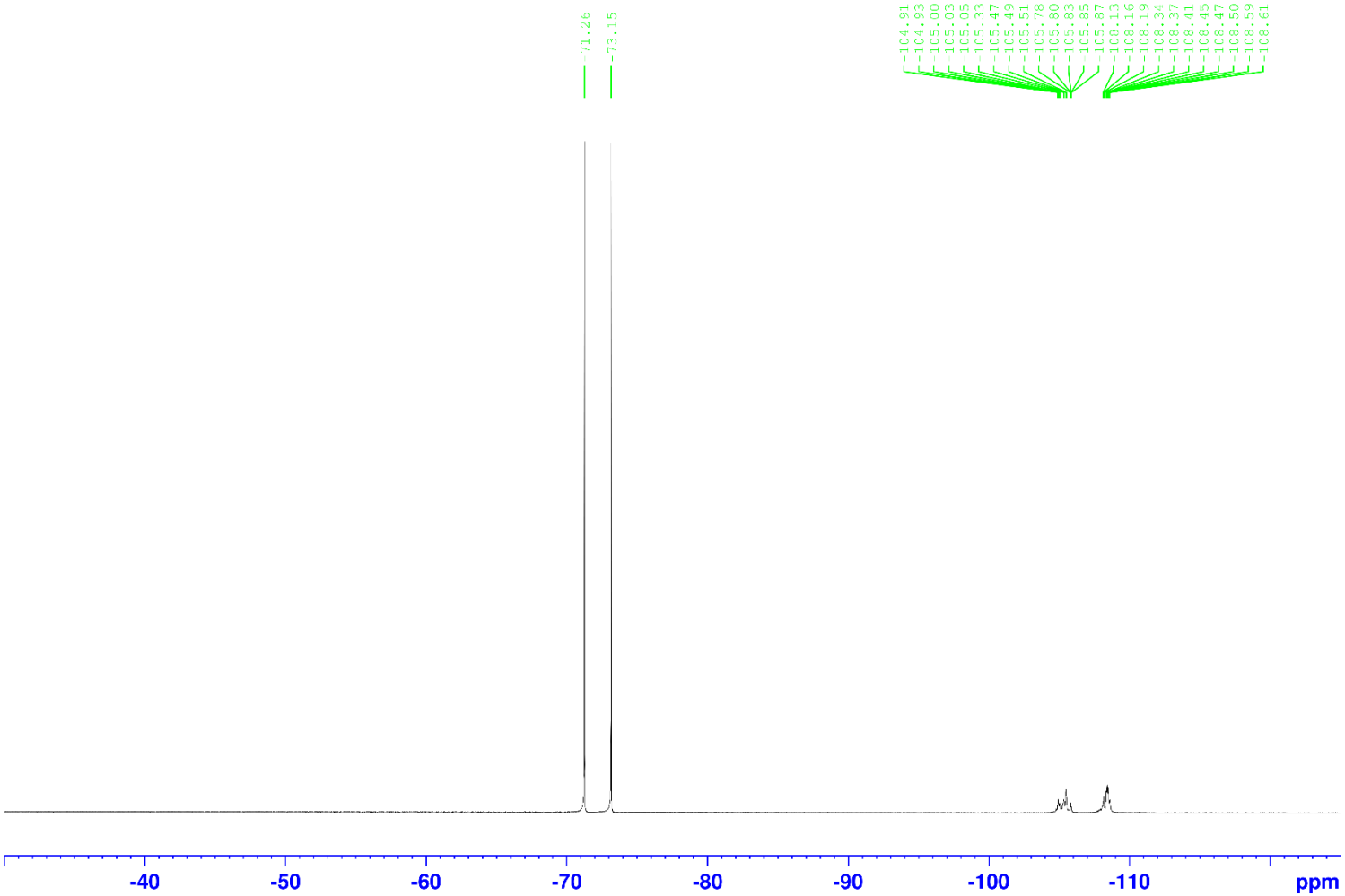

Supplementary Fig. 50 | ^{19}F NMR (376.5 MHz, CD_2Cl_2) spectrum of 15b.

Supplementary References

1. Cocquet, G., Ferroud, C. & Guy, A. A mild and efficient procedure for ring-opening reactions of piperidine and pyrrolidine derivatives by single electron transfer photooxidation. *Tetrahedron* **56**, 2975-2984 (2000).
2. Cocquet, G., Ferroud, C., Simon, P. & Taberna, P.-L. Single electron transfer photoinduced oxidation of piperidine and pyrrolidine derivatives to the corresponding lactams. *J. Chem. Soc., Perkin Trans. 2*, 1147-1153 (2000).
3. Goulet-Hanssens, A. *et al.* Hole catalysis as a general mechanism for efficient and wavelength-independent Z→ E azobenzene isomerization. *Chem* **4**, 1740-1755 (2018).
4. Watanabe, K. *et al.* Indolizines enabling rapid uncaging of alcohols and carboxylic acids by red light-induced photooxidation. *Org. Lett.* **22**, 5434-5438 (2020).
5. Lancel, M., Gomez, C., Port, M. & Amara, Z. Performances of homogeneous and heterogenized methylene blue on silica under red light in batch and continuous flow photochemical reactors. *Front. Chem. Eng.* **3**, 752364 (2021).
6. Mei, L., Veleta, J. M. & Gianetti, T. L. Helical carbenium ion: a versatile organic photoredox catalyst for red-light-mediated reactions. *J. Am. Chem. Soc.* **142**, 12056-12061 (2020).
7. Mei, L., Moutet, J., Stull, S. M. & Gianetti, T. L. Synthesis of CF3-containing spirocyclic indolines via a red-light-mediated trifluoromethylation/dearomatization cascade. *J. Org. Chem.* **86**, 10640-10653 (2021).
8. Stull, S. M., Mei, L. & Gianetti, T. L. Red-light-induced N, N′-dipropyl-1, 13-dimethoxyquinacridinium-catalyzed [3+ 2] cycloaddition of cyclopropylamines with alkenes or alkynes. *Synlett* **33**, 1194-1198 (2022).
9. Ravetz, B. D. *et al.* Development of a platform for near-infrared photoredox catalysis. *ACS Cent. Sci.* **6**, 2053-2059 (2020).
10. Ogbu, I. M., Bassani, D. M., Robert, F. & Landais, Y. Photocatalyzed decarboxylation of oxamic acids under near-infrared conditions. *Chem. Commun.* **58**, 8802-8805 (2022).
11. Tay, N. E. S. *et al.* Targeted activation in localized protein environments via deep red photoredox catalysis. *Nat. Chem.* **15**, 101-109 (2023).
12. Lee, J., Papatzimas, J. W., Bromby, A. D., Gorobets, E. & Derksen, D. J. Thiaporphyrin-mediated photocatalysis using red light. *RSC Adv.* **6**, 59269-59272 (2016).
13. Matsuzaki, K., Hiromura, T., Tokunaga, E. & Shibata, N. Trifluoroethoxy-Coated Subphthalocyanine affects Trifluoromethylation of Alkenes and Alkynes even under Low-Energy Red-Light Irradiation. *ChemistryOpen* **6**, 226-230 (2017).
14. Yerien, D. E., Cooke, M. V., Vior, M. C. G., Barata-Vallejo, S. & Postigo, A. Radical fluoroalkylation reactions of (hetero) arenes and sulfides under red light photocatalysis. *Org. Biomol. Chem.* **17**, 3741-3746 (2019).
15. Ishikawa, Y. *et al.* Red-light-activatable ruthenium phthalocyanine catalysts. *Chem. Commun.* **57**, 13594-13597 (2021).
16. Buksh, B. F. *et al.* μMap-Red: proximity labeling by red light photocatalysis. *J. Am. Chem. Soc.* **144**, 6154-6162 (2022).
17. Ogura, A., Ichii, N., Shibata, K. & Takao, K.-i. Red-light-mediated Barton–McCombie reaction. *Bull. Chem. Soc. Jpn.* **93**, 936-941 (2020).
18. Rybicka-Jasińska, K. *et al.* Porphyrins as promising photocatalysts for red-light-induced functionalizations of biomolecules. *ACS Org. Inorg. Au* **2**, 422-426 (2022).
19. Whittemore, T., Xue, C., Huang, J., Gallucci, J. & Turro, C. Single-chromophore single-molecule photocatalyst for the production of dihydrogen using low-energy light. *Nat. Chem.* **12**, 180-185 (2020).
20. Huang, J., Sun, J., Wu, Y. & Turro, C. Dirhodium (II, II)/NiO photocathode for photoelectrocatalytic hydrogen evolution with red light. *J. Am. Chem. Soc.* **143**, 1610-1617 (2021).
21. Katsurayama, Y. *et al.* Direct near infrared light–activatable phthalocyanine catalysts. *Chem. –Eur. J.* **28**, e202103223 (2022).
22. Sellet, N., Sebbat, M., Elhabiri, M., Cormier, M. & Goddard, J.-P. Squaraines as near-infrared photocatalysts for organic reactions. *Chem. Commun.* **58**, 13759-13762 (2022).
23. Tanioka, M. *et al.* Bridged eosin Y: a visible and near-infrared photoredox catalyst. *Chem. Commun.*

58, 7825-7828 (2022).
24. Su, X.-D. *et al.* Near-infrared-light-induced iron (I) dimer-enabled halogen atom transfer for rapid iodoperfluoroalkylation of alkenes. *Chem Catal.* **3**, 100710 (2023).
25. Ravetz, B. D. *et al.* Photoredox catalysis using infrared light via triplet fusion upconversion. *Nature* **565**, 343-346 (2019).
26. Kundu, B. K., Han, G. & Sun, Y. Derivatized benzothiazoles as two-photon-absorbing organic photosensitizers active under near infrared light irradiation. *J. Am. Chem. Soc.* **145**, 3535-3542 (2023).
27. Sinha, N., Wegeberg, C., Häussinger, D., Prescimone, A. & Wenger, O. S. Photoredox-active Cr (0) luminophores featuring photophysical properties competitive with Ru (II) and Os (II) complexes. *Nat. Chem.* **15**, 1730-1736 (2023).
28. Glaser, F. & Wenger, O. S. Red light-based dual photoredox strategy resembling the Z-scheme of natural photosynthesis. *JACS Au* **2**, 1488-1503 (2022).
29. Han, G. *et al.* Two-photon-absorbing ruthenium complexes enable near infrared light-driven photocatalysis. *Nat. Commun.* **13**, 2288 (2022).
30. Goldschmid, S. L. *et al.* Overcoming photochemical limitations in metallaphotoredox catalysis: red-light-driven C–N cross-coupling. *J. Am. Chem. Soc.* **144**, 22409-22415 (2022).
31. Bilger, J. B., Kerzig, C., Larsen, C. B. & Wenger, O. S. A photorobust Mo (0) complex mimicking [Os (2, 2′-bipyridine) 3] 2+ and its application in red-to-blue upconversion. *J. Am. Chem. Soc.* **143**, 1651-1663 (2021).
32. Wang, C., Wegeberg, C. & Wenger, O. S. First-Row d6 Metal Complex Enables Photon Upconversion and Initiates Blue Light-Dependent Polymerization with Red Light. *Angew. Chem.* **135**, e202311470 (2023).
33. Hu, X. *et al.* Red-light-driven atom transfer radical polymerization for high-throughput polymer synthesis in open air. *J. Am. Chem. Soc.* **145**, 24315-24327 (2023).
34. Zhou, Z., Wang, Z., Blenko, A. L., Li, J. & Lin, W. Viologen covalent organic framework mediates near-infrared light-induced electron transfer for catalytic oxidative coupling reactions. *J. Am. Chem. Soc.* **147**, 10846-10852 (2025).
35. Morselli, G., Eggenweiler, T. H., Villa, M., Prescimone, A. & Wenger, O. S. Pushing the Thermodynamic and Kinetic Limits of Near-Infrared Emissive CrIII Complexes in Photocatalysis. *J. Am. Chem. Soc.* **147**, 28226-28240 (2025).
36. Chacktas, G. *et al.* Evidence of Spin-Forbidden Excitation of [Ru (bpy) 3] 2+ and Application in Red-Light-Driven Photocatalysis. *ACS Catal.* **15**, 13938-13947 (2025).
37. Wellauer, J. *et al.* Iron (III) Complexes with Luminescence Lifetimes of up to 100 ns to Enhance Upconversion and Photocatalysis. *J. Am. Chem. Soc.* **147**, 8760-8768 (2025).
38 Zeng, L., Wang, Z., Zhang, T., Duan, C. Direct utilization of near-infrared light for photooxidation with a metal-free photocatalyst. *Molecules* **27**, 4047 (2022).
39. Sellet, N., Clement-Comoy, L., Elhabiri, M., Cormier, M., Goddard, J. -P. Second generation of near-infrared cyanine-based photocatalysts for faster organic transformation. *Chem. –Eur. J.* **29**, e202302353 (2023).